



HAL
open science

Growth and spectroscopic studies (continuous and time-resolved) of ultrathin films of topological insulators

Mateusz Weis

► **To cite this version:**

Mateusz Weis. Growth and spectroscopic studies (continuous and time-resolved) of ultrathin films of topological insulators. Materials. Le Mans Université; Uniwersytet Śląski (Katowice, Pologne), 2019. English. NNT : 2019LEMA1001 . tel-03038512

HAL Id: tel-03038512

<https://theses.hal.science/tel-03038512>

Submitted on 3 Dec 2020

HAL is a multi-disciplinary open access archive for the deposit and dissemination of scientific research documents, whether they are published or not. The documents may come from teaching and research institutions in France or abroad, or from public or private research centers.

L'archive ouverte pluridisciplinaire **HAL**, est destinée au dépôt et à la diffusion de documents scientifiques de niveau recherche, publiés ou non, émanant des établissements d'enseignement et de recherche français ou étrangers, des laboratoires publics ou privés.

THESE DE DOCTORAT DE

LE MANS UNIVERSITE
COMUE UNIVERSITE BRETAGNE LOIRE

ECOLE DOCTORALE N° 596
Matière Molécules et Matériaux
Spécialité : Physique

Par

Mateusz WEIS

« Growth and spectroscopic studies (continuous and time-resolved) of ultrathin films of topological insulators »

Thèse présentée et soutenue à Chorzow, Pologne, le 09.01.2019

Unité de recherche : SMCEBI , University of Silesia

Thèse N° : 2019LEMA1001

UNIVERSITY OF SILESIA IN KATOWICE
KATOWICE, POLOGNE

WYDZIAŁ MATEMATYKI, FIZYKI I CHEMII
Instytut Fizyki im. Augusta Chelkowskiego

Composition du Jury :

Jozef KORECKI Professor, IFIS - ZFCS, AGH
Luca PERFETTI Professor, LSI - Ecole Polytechnique

Grazyna CHELKOWSKA Professor, ZFCS, University of
Massimiliano MARANGOLO Professor, INSP - University of
Sorbonne
Artur CHROBAK Professor, ZFCS, University of
Roman WRZALIK Professor, ZBiFM, University of Silesia
Andrzej BURIAN Professor, ZBiFM, University of Silesia

Directeur de thèse

Pascal RUELLO Professor, IMMM - CNRS, Le Mans Université
Jacek SZADE Professor, WMFCh - ZFCS, University of Silesia
Co-directeur de thèse

Katarzyna BALIN Doctor, ZFCS, University of Silesia -
Gwenaëlle VAUDEL DoctorIMMM - CNRS, Le Mans Université

Titre : Croissance et études spectroscopiques (continues et résolues dans le temps) de couches ultra-minces d'isolants topologiques.

Mots clés : Isolants topologiques, Bi_2Te_3 , Spintronique, Couches ultra-minces, Spectroscopie femtoseconde

Résumé : Les isolants topologiques (TIs) sont l'un des éléments clés de la nouvelle génération de composants pour la spintronique. Ils offrent des perspectives de conversion de charge en courant de spin ou de réalisation de diodes Schottky à l'échelle nanométrique à base de fermions Dirac. Lorsque les TIs sont élaborés en couches ultra-minces (<10nm), ou soumis à un dopage approprié en éléments magnétiques, des modifications dramatiques se produisent sur la structure électronique et la dynamique des porteurs et des phonons. Pour décrire ces comportements partiellement compris, nous avons utilisé tout d'abord une chambre MBE pour faire croître des films de Bi_2Te_3 sur un substrat de mica muscovite. La structure monocristalline du film a été confirmée par des mesures LEED et RHEED, et les études complémentaires de structure électronique par XPS ont été conduites.

La spectroscopie femtoseconde pompe-sonde a ensuite été utilisée pour l'étude dynamique des porteurs chauds et des phonons optiques et acoustiques cohérents.

Dans cette thèse, nous mettons en évidence un effet de confinement quantique (<6nm) qui affecte les temps de vie des porteurs de charges mais aussi la dynamique des phonons. Des comportements similaires ont été observés quand les films (12nm) sont en interaction avec une couches magnétiques déposées en surface (dopage). La contribution respective des électrons de volume et ceux de surface (Dirac) à ces phénomènes est discutée. Ces résultats originaux apportent de nouveaux éclairages sur la physique des électrons et des phonons dans les couches minces d'isolants topologiques.

Growth and spectroscopic studies (continuous and time-resolved) of ultrathin films of topological insulators

Keywords : Topological insulators, Bi_2Te_3 , Spintronics, Ultrathin films, Femtosecond spectroscopy

Abstract : Topological insulators (TI) are one of the critical elements for the new generation of electronics and spintronics devices. Such as charge-to-spin current conversion gates or Dirac fermions based nanometer scale Schottky diodes. When reduced just too a few single layers or exposed to additional doping, TI begins to show a dramatic effect that changes the electronic structure and in consequence dynamics of carriers and phonons. In order to describe those behaviors, I used advanced high-vacuum cluster with MBE to produce ultrathin films of Bi_2Te_3 . The samples were grown on a muscovite mica substrate. The monocristalline structure of the film was confirmed with both LEED and RHEED measurements, and the complementary studies of electronic structure focused on the analysis of the valence band and core levels.

The femtosecond pump-probe spectroscopy has been used to excite the hot carriers and generate coherent optical phonons within Bi_2Te_3 nanostructures and observe it in the time domain.

In this thesis, I reveal an evident modification of the out-of-equilibrium carriers and phonons dynamics when extreme thickness or doping modify the BT layer. Performed experimental optical measurement integrate both bulk and surface electrons, but nonnegligible surface carriers contribution still gives a strong response. This continuous and time-domain investigation provides new insight into physical properties of topological insulators and shows that downscaling the topological insulators properties and their interaction with metallic interfaces have to be taken into account for potential TIs based spintronic devices.

Acknowledgements

First of all, I would like to express my gratitude to my supervisors Professor Pascal Ruello and Professor Jacek Szade, for their patience and guidance during my studies. Their inspiring scientific discussions and insight helped me in all the time of research and writing of this thesis. I could not have imagined having a better advisors and mentors for my Ph.D study. I would like to thank my Ph.D co-supervisor Katarzyna Balin and Gwenaelle Vaudel. Without their precious support it would not be possible to conduct this research. I would also like to thank Embassy of France in Poland for granting me Cotutelle scholarship, without it this research would be impossible. Last but not the least, I would like to thank my family and my Love for supporting me spiritually throughout writing this thesis and my life in general.

Contents

1	Outline	4
2	Introduction	7
2.1	Topological Insulators	8
2.1.1	Discovery of TIs	8
2.1.2	Theory of TIs	9
2.2	Applications of topological insulators and limitations of the technology . . .	15
2.3	Basic information on Bi_2Te_3	19
3	Samples preparation	23
3.1	Growth of ultra thin films	24
3.2	Molecular beam epitaxy (MBE)	29
3.3	Sample description	32
3.4	Summary	38
4	Diffraction and continuous spectroscopy techniques	40
4.1	Surface structure analysis	41
4.1.1	Reflection high-energy electron diffraction (RHEED)	42
4.1.2	Low energy electron diffraction (LEED)	45
4.2	Chemical and electron state analysis	49
4.2.1	X-ray photo-electron spectroscopy	50

<i>CONTENTS</i>	3
4.3 Summary	65
5 Time-resolved spectroscopy techniques	67
5.1 Introduction to pump-probe techniques	68
5.1.1 Experiment	68
5.1.2 Theory	70
5.2 Femtosecond laser spectroscopy - results	85
5.2.1 Role of structural order on electron and phonon dynamics	85
5.2.2 Quantum confinement effects	93
5.2.3 Influence of iron oxide capping layers	104
6 Summary	112
7 Appendix	118
7.1 Second harmonic generation	118
7.1.1 Frequency mixing and parametric generation of light	120
7.2 Optical parameters of Bi_2Te_3	123
7.3 Reflectivity change	125
7.4 Publications	126

Chapter 1

Outline

Topological insulators (TIs) represent an exciting group of materials that exhibit a quantum phenomenon even at room temperature. In 2016 Nobel Prize in physics was awarded for theoretical discoveries of topological phase transitions and topological phases of matter [1]. As stated in the press release of the Nobel Committee laureates: *"opened the door on an unknown world where matter can assume strange states. They have used advanced mathematical methods to study unusual phases, or states, of matter, such as superconductors, superfluids or thin magnetic films. Thanks to their pioneering work, the hunt is now on for new and exotic phases of matter. Many people are hopeful of future applications in both materials science and electronics"*. Over the last decade, topology research has been leading in the field of condensed matter physics - mainly due to the discovery of new topological phases matter and exotic effects not observed in classic materials, giving hope for wide use in a variety of devices. By entering into current trends, we propose an experimental approach to the subject, including the creation of TI-based structures and the study and modification of their properties. TI is poorly conducting electricity in the bulk (center) of the crystal, but the surface electrons can move around freely in a manner that is protected from defect scattering. Moreover, all electrons moving in a given direction must have their spins, pointing the same way (spin locking), or to put it another way, all electrons with the same spin component must travel in the same

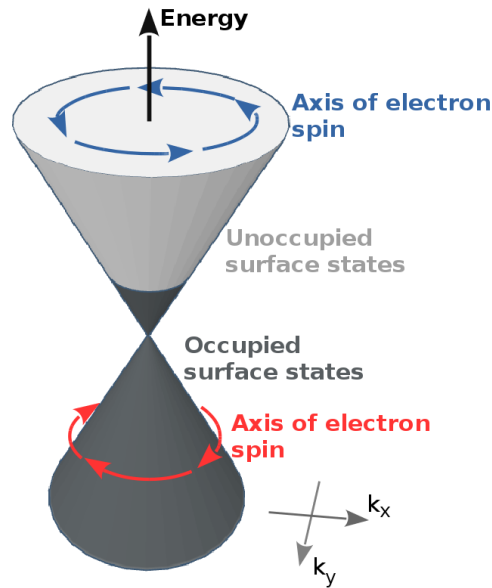


Figure 1.1: Artistic view of Dirac cone in topological insulators.

direction. This spin or internal angular momentum can be imagined as a property associated with particle motion around its axis (Fig.1.1) [2, 3].

The result possibility to control moving spin-polarized electrons around the material by passing current has generated considerable interest in potential electronic applications. Like for example spin valves or sources (injectors) of spin-polarized carriers, Schottky diodes or even spin-to-charge converters [4, 5, 6, 7]. Such phenomena as surface states and the electron spin polarization are still hard to observe without highly sophisticated equipment such as angle-resolved photoemission spectroscopy (ARPES) [8, 9, 10, 11]. Unfortunately, such measurements require extremely fresh surface layer because of low penetration depth of measurements as well as overlapping of the band structure coming from the oxidation of the layers. Because of that, it is impossible to work on a sample outside of the ultra-high vacuum, and even then it is possible to keep the complete freshness of the surface only for a couple of hours. Fortunately, it is possible to still tap into this phenomena in real working conditions. To do so, it is necessary to utilize the very short penetration depth of the visible light in materials

such as Bi_2Te_3 . Due to a thorough analysis of the existing oxidized layer, it is known that it is a mixture of tellurium and bismuth oxide, which are transparent in visible spectra, that do not disturb the measurement [12]. Because of their similar properties to the passivated layer of aluminum oxide, they create stable about 2nm thick layer that protects the material from further damage and moisture.

The technique that can utilize all those properties to its fullest potential is so-called pump-probe femtosecond laser spectroscopy. The basic concept of this method is quite simple. The femtosecond laser creates short pulses 200fs (200×10^{-15} s) that are divided into a pumping beam, that excites the electrons and vibration with the thin layer and probe which detects the change of reflection or transmission as a function of time. This experiment is very similar to the creation of stop-motion film one photo at the time, due to a moving mirror (delay line) we can "photograph" effect of the pump after a slightly different time. This technique allows subtle interaction with the matter and can detect even the slight changes within the analyzed structure without damaging it. That is why pump-probe spectroscopy is widely used in electronic devices development and control of their quality. The signal registered with this technique consists of different phenomena such as relaxation of the photo-excited carriers, phonon vibrations, and even mechanical vibration of various structures in the sample. Due to the ability of direct interaction with the electrons, it is possible to observe such subtle changes like modification of electron dynamic even after exposure to air and aging of the thin film or to directly register the crystal lattice (phonon) vibration in the time domain. In this work, we utilized advanced techniques for creation (MBE) of the samples that allow us to perform a proper investigation of the effects generated by variable nanostructures such as state of crystallization or critical thickness dependence as well as phenomena occurring at proximity to TI-metal interface. These techniques, along with careful structural (LEED/RHEED), chemical and electronic analysis (XPS), can provide a great insight into the realization of working spintronic and optospintronic systems. We hope that the data presented in this work will bring us closer to an understanding of phenomena governing this highly unusual phase of matter.

Chapter 2

Introduction

The primary focus of this work is physics surrounding the topological insulators, in particular, the Bi_2Te_3 . In this chapter, we will concentrate on bringing closer the subject of this new physical phase of matter and physical phenomena that will help to understand it better. We will also try to outline its present and future applications.

2.1 Topological Insulators

In this section, we described closer the history of topological insulators and physics standing behind them.

2.1.1 Discovery of TIs

To fully understand the concept of topological insulators, we have to mention the two most crucial discoveries to this topic. First of which is one of the greatest successes in quantum physics. That is the band theory of electric conduction made by Bloch in 1920 [13]. This theory gave us an understanding of the process governing the conduction within the crystals. In this model, electronic states of electrons are described by Bloch states. These states are plane waves with momentum wavevector \mathbf{k} modulated by the crystal lattice symmetries. This approach brought to life the idea of the continuous band structure of the solids and gave us a tool to easily distinguish materials that are conductors, semiconductors, or insulators. The reaction of a crystal to an external electric field can be purely determined by the state of electrons close to the Fermi energy. In the case of metals in which bands are only partially filled out, an external current can cause an asymmetrical redistribution of the population of electrons along with the momentum leading to the launching of the electric current. In the case of insulators and semiconductors, energy bands below the Fermi level are filled out, and the empty bands are separated from them by the so-called energy gap. This gap prevents the redistribution of the population of electrons by the external field and in result blocks the launch of the current.

The second important point on the path to the topological insulators was the discovery of the integer quantum Hall effect. The effect first predicted by Ando, Matsumoto, and Uemura in 1975 and then directly observed by Kitzling in 1980 [14, 15]. This quantum-mechanical version of Hall effects appears in two-dimensional electron systems at low temperatures and in the presence of strong magnetic fields. Under these circumstances, the Hall conductance σ

transforms into a quantum version with quantized values given by the following expression:

$$\sigma = \frac{I}{V_{Hall}} = \nu \frac{e^2}{h}$$

where σ is Hall conductance, I the channel current, V_{Hall} is the Hall voltage, ν is so-called filling factor and can take integer (1, 2, 3...) or fractional ($\frac{1}{3}, \frac{3}{7}, \dots$) values, e is elementary charge and h is a Plank's constant. We can interpret this effect as a situation where the bulk of the material can be an insulator while the edges are conducting. In the case of two dimensions materials, when electrons are in strong perpendicular to the surface magnetic field, they start to be confined into circular cyclotron orbits. In low temperatures, these orbits are quantized. The energy levels of these quantized orbitals are highly degenerate Landau levels n and take on following discrete values:

$$E_n = \hbar\omega_c \left(n + \frac{1}{2} \right)$$

where ω_c is the cyclotron frequency related to the external magnetic field $\omega_c = \frac{eB}{m}$. In the case when N energy levels are fully occupied and $(N + 1)$ is empty, we have a situation similar to the insulator with a gap equal to $\hbar\omega_c$, meanwhile on edge, the magnetic field forces the electrons into robust skipping orbits. This effect leads to the situation mentioned above where the material appears to be insulating in bulk and conducting on its edges.

Those two discovers paved the road for Moore and Balents to introduced in 2007 a new phase in condense matter physic "Topological Insulator". This new kind of electronic phase was discovered independently by three theoretical groups in the summer of 2006. Soon after that, this exotic state was observed in several real materials such as strained $HgTe$ quantum wells, $\alpha - Sn$, and $Bi_{1-x}Sb_x$ alloys. Those discoveries resulted in the rapid development of an entirely new branch of materials which have shown this new phase [2, 3, 9].

2.1.2 Theory of TIs

The origin of this unique quantum phase lies in the degeneration of the energy levels of chemical bonds, by the break in the crystal field symmetry, at the surface of the material

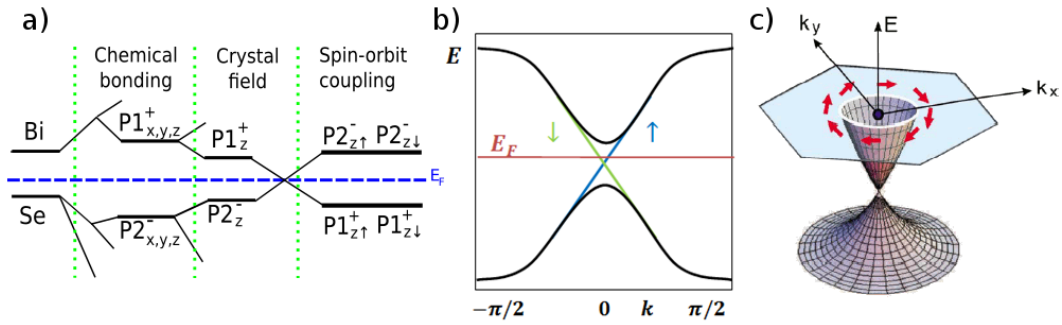


Figure 2.1: a - Evolution of the molecular band structure leading to appearance of TI state. b - Schematic of the spin-polarized surface-states dispersion in bismuth based TI. Green and blue arrow indicate the polarization of the spin. c - 3D visualization of the Dirac cone in TI. From Hasan and Kane (2010).

(Fig.2.2.a). These degenerated levels are then flipped by strong spin-orbit coupling interaction leading to the creation of the Dirac cone close to the Fermi energy (Fig.2.1.b/c). An effect like that can be observed for materials such as Bi_2Te_3 and Bi_2Se_3 [16] where the Dirac cone lies precisely at the Γ point in Brillouin zone. This materials like any other ordinary insulator or semiconductor show clear bulk energy gap separation, of the lowest unoccupied electronic band from the highest occupied band, but the difference lies in the presence of gapless edge states (2D) or surface states (3D) (Fig.2.1.b and c) which are protected by Θ time-reversal symmetry (product of spatial and spin degrees of freedom). As well as the "half-integer" quantum Hall effect (QHE), in which the skin and bottom of the thin film are contributing a half-integer unit of quantum conductance e/h . These two half-integer parts create the so-called Hall conductance plateau, which is quantized with integer units of e^2/h [3]. Half-integer QHE is another unique property of TI and is direct proof that surface-states carriers are spin-polarized massless Dirac fermions Fig.2.2. They are the same massless Dirac fermions that exist in other novel material graphene, which consist of only one atom sheet of carbon. In graphene, the charge carriers are, opposed to topological insulators, not spin-polarized and exist in four degenerate states (Dirac cones), whereas on a topological insulator surface there is only one Dirac cone, in

the center of Brillouin zone at Γ point. In order to better understand the topological insulators let us introduce the definition of the Berry phase that can be interpreted as a phase acquired by the wavefunction, when the parameters are appearing in the Hamiltonian are slowly changing in time they allow the system to adapt its configuration (adiabatic process). Let us consider the Berry phase in crystal [17]. We can approximate Hamiltonian of the independent electron as:

$$\hat{H} = \frac{\hat{P}}{2m_e} + V(r)$$

where $V(r) = V(r + R_n)$ has a period of the lattice R_n . With boundary conditions $\Psi_{mk}(r + R_n) = e^{ikR_n}\Psi_{mk}(r)$ where Ψ_{mk} is the eigenstate corresponding to the m band and k is the wave number which is defined in the Brillouin zone. We can rewrite them in following way $\Psi_{mk} = e^{ikr}u_{mk}(r)$ where $u_{mk}(r)$ has the same period as lattice. The function u_{mk} satisfies the following Schrodinger equation:

$$\hat{H}(k)|u_m(k)\rangle = E_m|u_m(k)\rangle$$

Let us consider a two-dimensional crystalline system. Then the Berry connection of the m band is equal to:

$$A^{(m)}(k) = i\langle u_m(k)|\nabla_k u_m(k)\rangle$$

and the Berry curvature $\Omega^{(m)}(k)$ can be written as:

$$\Omega^{(m)}(k) = \nabla_k \times i\langle u_m(k)|\nabla_k u_m(k)\rangle$$

This leads us to the Chern number that can be written as:

$$Q^{(m)} = -\frac{1}{2\pi} \int_{BZ} \Omega^{(m)}(k) dk$$

the above integration is taken over the Brillouin zone (BZ), the Chern number is an intrinsic property of the band structure and has various effects on the transport properties of the system. Chern number is an integral relating the curvature of topological invariant $n \in \mathbb{Z}$ (\mathbb{Z} describes the integers). A good example is a genus (Fig.2.2.a and Fig.2.2.b) the topological number,

Table 2.1: Periodic table of topological insulators and superconductors. Ten symmetry classes are labelled using Altland and Zirnbauer (1997) notation.

Symmetry				Dimension							
AZ	Θ	Ξ	Π	1	2	3	4	5	6	7	8
A	0	0	0	0	\mathbb{Z}	0	\mathbb{Z}	0	\mathbb{Z}	0	\mathbb{Z}
AIII	0	0	1	\mathbb{Z}	0	\mathbb{Z}	0	\mathbb{Z}	0	\mathbb{Z}	0
AI	1	0	0	0	0	0	\mathbb{Z}	0	\mathbb{Z}_2	\mathbb{Z}_2	\mathbb{Z}
BDI	1	1	1	\mathbb{Z}	0	0	0	\mathbb{Z}	0	\mathbb{Z}_2	\mathbb{Z}_2
D	0	1	0	\mathbb{Z}_2	\mathbb{Z}	0	0	0	\mathbb{Z}	0	\mathbb{Z}_2
DIII	-1	1	1	\mathbb{Z}_2	\mathbb{Z}_2	\mathbb{Z}	0	0	0	\mathbb{Z}	0
AII	-1	0	0	0	\mathbb{Z}_2	\mathbb{Z}_2	\mathbb{Z}	0	0	0	\mathbb{Z}
CH	-1	-1	1	\mathbb{Z}	0	\mathbb{Z}_2	\mathbb{Z}_2	\mathbb{Z}	0	7	0
C	0	-1	0	0	\mathbb{Z}	0	\mathbb{Z}_2	\mathbb{Z}_2	\mathbb{Z}	0	0
CI	1	-1	1	0	0	\mathbb{Z}	0	\mathbb{Z}_2	\mathbb{Z}_2	\mathbb{Z}	0

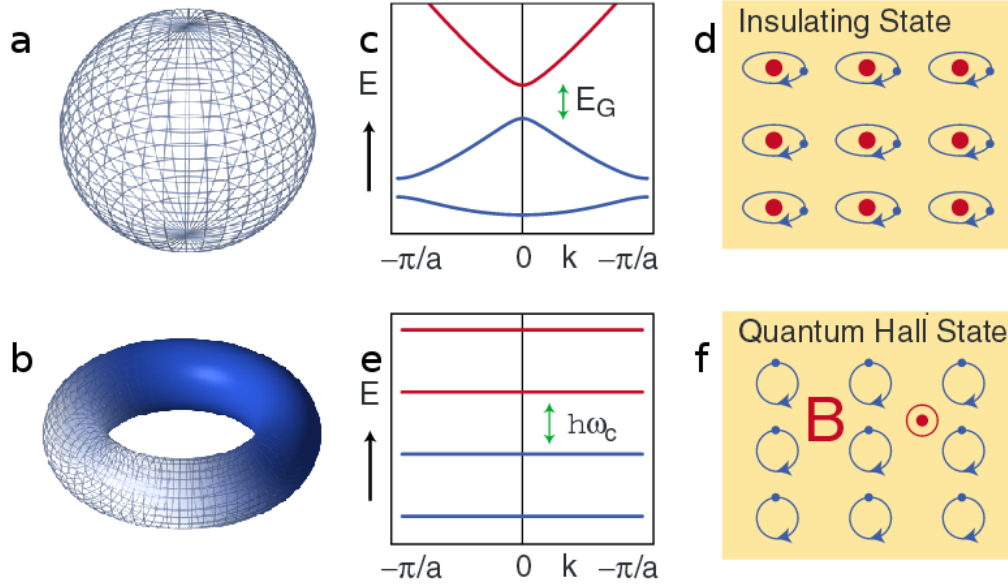


Figure 2.2: Example of object with genus $g=0$ (a) and $g=1$ (b) . c and d depict model of insulator. e and f are model of quantum Hall state. From Hasan and Kane.

which counts the number of holes, that remains constant under continuous and smooth transformations. In the presented above table we listed the topological classification of topological insulators and superconductors according to the presence or absence of time symmetry Θ , particle-hole symmetry Ξ and chiral symmetry $\Pi = \Xi\Theta$. Values in columns 2,3 are specifying the Θ^2 and Ξ^2 , and we can see that these symmetries as a function of dimensionality show a regular pattern of topological systems (\mathbb{Z}, \mathbb{Z}_2 and 0)[3]. According to M.Z. Hasan and C.L. Kane we can find that materials with quantum Hall state occupy class A with no symmetry and exist in 2D materials; TI which require \mathbb{Z}_2 can be found in class AII with $\Theta^2 = -1$ in 2D and 3D materials; superconductors (SC) which can possess either \mathbb{Z} or \mathbb{Z}_2 can be found in class D with $\Xi^2 = 1$ required for the existence of Cooper pairs, in 1D and 2D materials. The Chern number possesses physical interpretation of the Berry phase of the Bloch wave functions. For example, a standard insulator (Fig.2.2.c and Fig.2.2.d) differs from the Quantum Hall State (Fig.2.2.e and Fig.2.2.f) only by the topology of the 2D band structure [3]. In QH we can dis-

tinguish metallic edges at the boundaries of the 2D electronic system, which is very similar to the 2D TI surface states. Physics of the topological insulators involves mainly the interaction between bulk (dimension d) and the surface (dimension $d-1$). Such states can be observed at a system with $d=2$ and $d=3$. For example, direct measurements of the band gap structure with ARPES have directly shown the formation of this novel state with a strong dependence on the thickness of the material (Fig.2.4) [9, 10, 11]. The 3D topological insulator can be characterized by the \mathbb{Z}^2 topological invariant. For the material to exhibit this phase, it is necessary to meet a few conditions. First is the existence of four time-invariant points at $\Gamma_{1,2,3,4}$ in the B.Z. and Kramers degeneracy of the surface state by crystal field. The second one is the breaking of this degeneracy away from those particular points by dominant spin-orbit coupling [16]. If the conditions mentioned above are met, surface states form the Dirac cone. This, in turn, leads to the appearance of the unique 2D topological metal and massless Dirac fermions (their mass is the second derivative of the Energy in k , and for this cone is equal to 0), what is the direct cause of the ballistic conductance of those materials. Additionally, this new metallic state possesses non-degenerated spin surface states on the Fermi surface. This phenomenon is directly caused by time symmetry which requires that k and $-k$ possess opposite spin.

In this, we can observe the non-trivial Berry phase, which strongly influences the interaction with magnetic fields as well as effects of the disorder. We can say that electrons in strong topological insulators are not localized even in the presence of disorder, which is analogous to the quantum spin Hall insulators edge states.

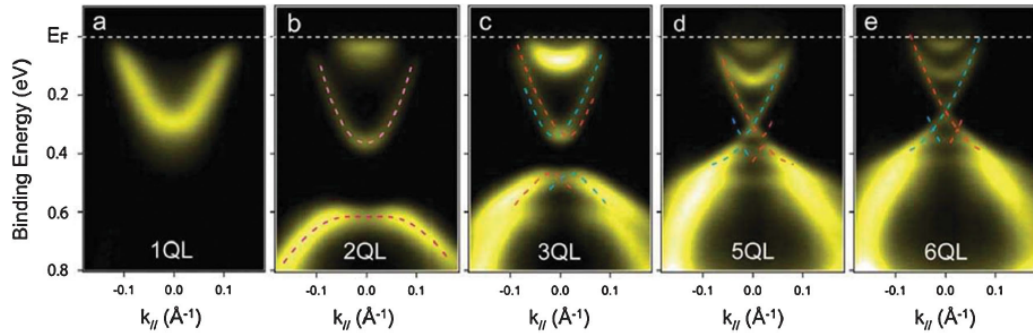


Figure 2.3: Crossover of the three-dimensional topological insulator Bi_2Se_3 to the two-dimensional limit. From Yi Zhang Nature Phys. (2010).

2.2 Applications of topological insulators and limitations of the technology

Topological insulators exhibit unique and fascinating electronic properties, such as the quantum spin Hall effect, anomalous quantum Hall effect, and topological magnetoelectric effect, as well as magnetic monopole images and Majorana fermions [2, 19, 20]. Unique properties of topological insulators have high possible applications for spintronics and quantum information processing, as well as magnetoelectric devices with higher efficiency and lower energy consumption [2, 4]. Currently, the most promising branch of spintronics, where topological insulators can find their use, is spin-charge conversion thanks to their strong spin-orbit coupling [5, 6, 7] they possess the crucial ability to connect charge with a spin degree of freedom. The ability to control the spin current by charge transport and reverse are the main goals of spintronics. Topological insulators, thanks to their strong spin-orbit coupling and possession of insulating bulk and metallic surface states with a Dirac cone dispersion, gained the reputation of the perfect candidate for the realization of spin-charge conversion devices. Thanks to unique helically locked, in Fermi contour, spin, and momentum at the surface of TI, the injection of the spin current into the surface of a TI will result in the appearance of 2D charge

current density on the surface (known as the inverse Edelstein effect, IEE) [21]. Recently, the IEE was shown experimentally by spin pumping [22, 23]. The helical surface states of topological insulator lead to a non-zero Berry's phase (π) of the electron wave function generating a broad spectrum of phenomena such as the absence of back-scattering [24, 25] and weak antilocalization [26].

The creation of new devices based on this material requires our better understanding of the phenomena surrounding these structures as well as knowing all limiting factors that will put a barrier in their development. One of the phenomena that somehow was disregarded so far in the literature is the role of electron-phonon coupling. As it is well-known spin-orbit coupling is essential in the formation of the topological state, but the electron-phonon coupling appears to set a limit on 2D surface electron transport. It was already shown that the existence of strong coupling with LO mode [27] and strong coupling of 2D surface electrons with LA mode [28] put limits on electron transport. Knowing that the electron-phonon coupling plays such an essential role in these materials, it is even more critical to know this coupling behavior well [29].

The second significant challenge ahead of us is an enhancement of the surface states contribution to the overall properties of the topological insulator material. In the case of ultra-thin films, the ratio of surface states to bulk states starts to be not negligible and grants us the ability to design working components based on those materials, and through the use of advanced techniques of deposition, it is possible to achieve high-quality crystals [30]. In the case of thin films, at a critical thickness, the surface states from opposite surfaces of the films can couple together and open thickness-dependent gap (Fig.2.4) [9, 31, 32], which is non-trivial and may give rise to quantum spin Hall state similarly to HgTe quantum wells [33]. The bandgap opening, in compounds like Bi_2Se_3 and Bi_2Te_3 , has been reproduced theoretically and it has been reported that additional quantum size effects should appear leading to topological quantum phase transitions that depend on the film thickness. So far this phenomenon was observed only by angle-resolved photoemission spectroscopy that has to be made under perfect high vacuum

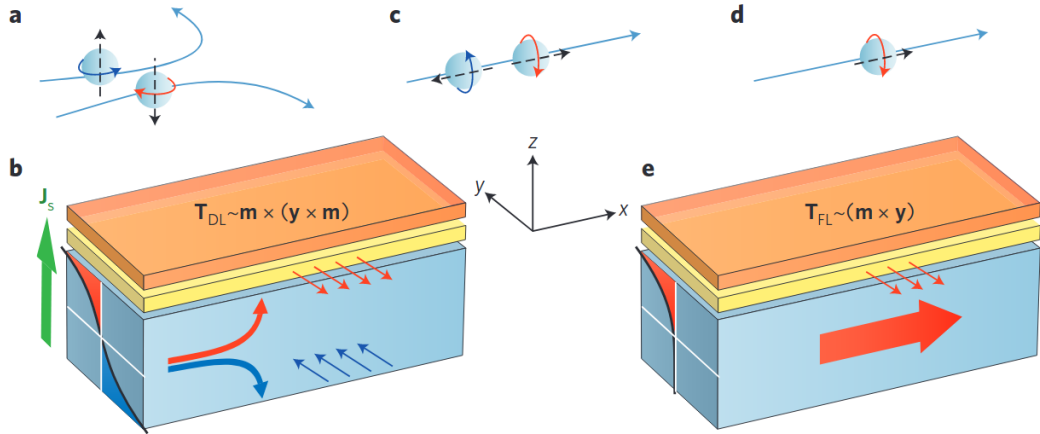


Figure 2.4: Presentation of effects generated by spin-orbit coupling for working spin-current conversion: a Thanks to the Magnus effect spin Hall effect creates a force that acts on spinning particles. b, On schematic heavy metal with strong spin-orbit coupling, is marked with blue, with yellow ferromagnetic layer and on top (orange) protective capping layer. The torque created by the spin Hall effect in a magnetic bilayer separates moving spins into aligned parallel (blue arrows) and anti-parallel (red arrows) to the direction of flow; this produces polarized spin current J_S (green arrow). This effect generates anti-damping torque T_{DL} that depends on the magnetization m and the direction of the spin accumulation y . c To nullify the effect of the Magnus force spin angular momenta (dashed arrows) must be frozen along the current direction. d In the case of a system without inversion symmetry like in topological insulators, this effect creates a spin-polarized current. In the case of breaking the inversion symmetry directly at the interface between the material with strong spin-orbit coupling (blue) and ferromagnetic layer (yellow) spin accumulates along the transverse direction leading to the appearance of non-equilibrium spin-orbit torque T_{FL} . From A. Manchon Nat.Phys.(2014).

and with the samples which surface is fresh, usually few minutes after deposition or cleaving of the crystal. Even then, the measurements prove to be difficult because of the rapid evolution of the states in the presence of a small number of adsorbents. In order to gain a better understanding of the processes of electron and phonon dynamics, under working conditions or exposure to air, a new approach to sample geometry and experimental methods like femtosecond laser spectroscopy have to be employed [12].

The third important part necessary to understand, in order to create working devices, the reaction both chemical as well as physical of topological insulators with additional materials deposited on it [34]. Currently carried experiment of spin-current conversion requires proximity to ferromagnetic (Fig.2.5) or metallic layer with strong spin-orbit coupling like platinum or cobalt [5, 6, 7]. The greatest challenge, to efficiently harness the potential of a topological insulator, is to create a stable chemical system that conserves the topological insulator surface states and still allow the transfer of generated polarized spin current into other layers. This motivates us to thoroughly investigate the chemical states and potential chemical reactions and evolutions of such interfaces. Knowledge gained through that would be crucial in finding proper configurations, that retain the proper evolution of the band system of topological insulators (like in a case of trivial interfaces [2, 3]), for the realization of a new generation of spintronic devices.

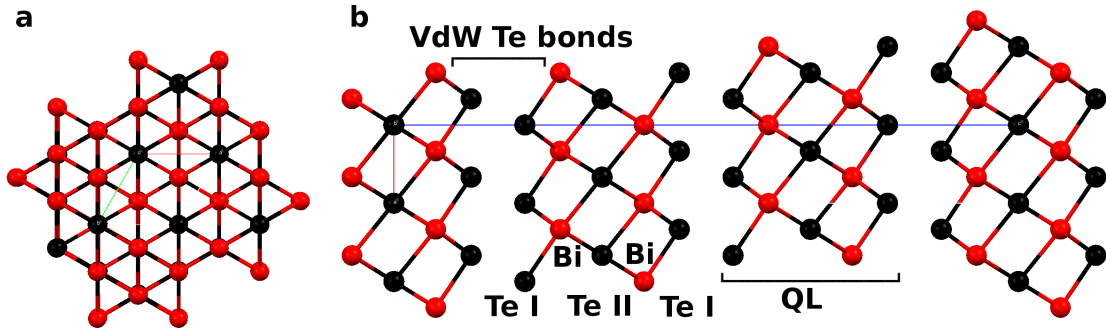


Figure 2.5: Crystallographic structure of Bi_2Te_3 with the quintuple layers (QL,s) connected through Van der Waals Te bonds. a Depicts view from c plane and b from the b plane.

2.3 Basic information on Bi_2Te_3

Bi_2Te_3 is a promising material that exhibits topological insulating properties [16]. Similarly to the Bi_2Se_3 and Sb_2Te_3 it belongs to the 3D topological insulator family which is more closely described in the previous subsection. Bismuth telluride in its bulk form is a narrow bandgap semiconductor that, aside from its TI behavior, possesses powerful thermoelectric properties that play an essential role in thermoelectric devices. This semiconductor has one of the highest figures of merit at room temperature. It is an auspicious material for application in electronics and especially in quantum computing due to excellent parameters and high ballistic conductivity.

Bi_2Te_3 is a trigonal rhombohedral crystal with 15 atoms in a unit cell, with Hermann - Mauguin index $R\bar{3}m:H$ and space group number 166. The single unit cell possesses one bismuth atom in coordinate [35] at:

$$Bi(x,y,z) = (0.00000; 0.00000; 0.40046)$$

two not equivalent positions of tellurium atoms at

$$Te_1(x,y,z) = (0.00000; 0.00000; 0.00000)$$

$$Te_2(x,y,z) = (0.00000; 0.00000; 0.79030)$$

and unit cell parameters

$$a = b = 4.395 \text{ \AA} \quad c = 30.440 \text{ \AA}$$

$$\alpha = \beta = 90^\circ \quad \gamma = 120^\circ$$

Bi_2Te_3 can be effortlessly cleaved along the trigonal axis due to Van der Waals bonding between neighboring tellurium atoms Fig.2.6. This figure presents cell generated with crystal visualization program, Mercury, using shown parameters.

In recent years, electronic properties of Bi_2Te_3 compound have been experimentally and theoretically studied by various ab-initio methods ([36, 37]). Theoretical calculations have shown that Bi_2Te_3 is a narrow-gap semiconductor, and its gap structure strongly depends on the spin-orbit coupling. Calculations shown in this work were completed in case of non-spin-orbit simulations on $20 \times 20 \times 4$ k-point mesh, and full spin-orbit calculations on $30 \times 30 \times 6$ k-point mesh. Calculations of the band structure were conducted with and without taking into account the spin-orbit coupling. Such calculations were performed with spin-polarized Hamiltonian and an additional $\sigma \cdot L$ term responsible for this coupling. Feeble external field of $0,017T$ was added in the direction of the z-axis in order to break spin symmetry. Calculated band structures without and with spin-orbit coupling are shown in Fig 2.6. It can be seen that Bi_2Te_3 is a semiconductor with a narrow energy gap. The character of the gap strongly depends on the spin-orbit interaction. This coupling changes the shape of the bands and the character of the gap from a direct to the indirect one. Such a result was already reported in this material [36]. From the calculations of the total density of states, the value of the energy gap changed in the case of calculations without spin-orbit coupling from $0.36eV$ down to $0.08eV$ in the case of spin-orbit calculations. This value is very close to experimental one of $0.145eV$ [38].

Besides the significant spin-orbit coupling effect on the features of surface and bulk electrons dynamics, the large electron-phonon coupling mechanisms is the object of active discussion and appear to play a peculiar role in the transport properties of the TIs. Bismuth telluride possesses both optical and acoustic phonon modes, which are depicted in Fig.2.8 and

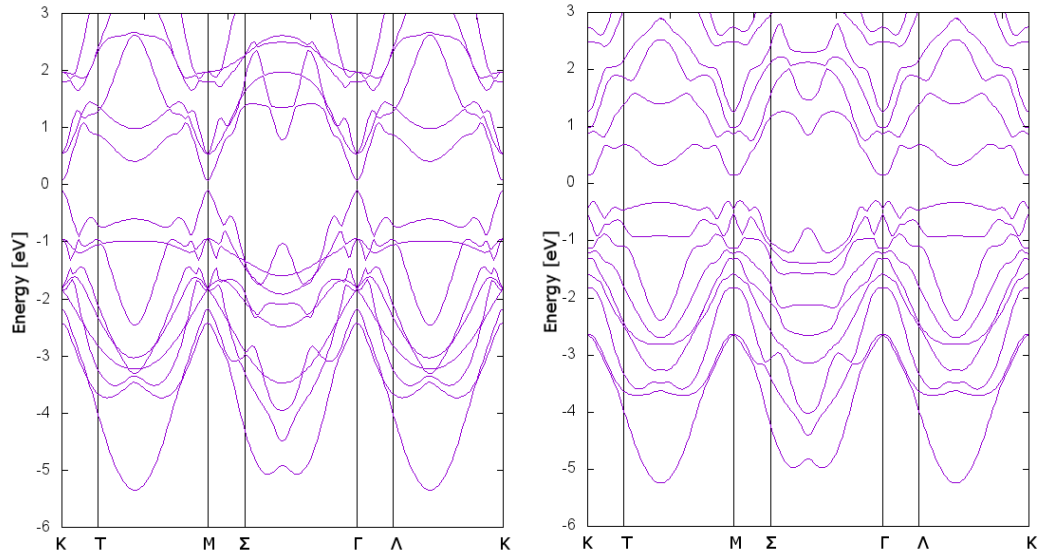


Figure 2.6: Band structure a) without and b) with spin orbit interactions.

Table 2.2: Phonon modes frequencies (in THz) of Bi_2Te_3 . Letters “E” in-plane and “A” out-of-plane lattice vibrations, letter g denotes Raman active and u IR active modes.

Name	Raman[39]	IR[39, 40]	Simulation [41]
A_{1g}^1	1,88		1,84
A_{1g}^2	4,02		3,74
A_{1u}^1		2,82	2,88
A_{1u}^2		3,60	3,58
E_g^1	1,10		1,47
E_g^2	3,09		3,42
E_u^1		1,50	1,43
E_u^2		2,85	2,90

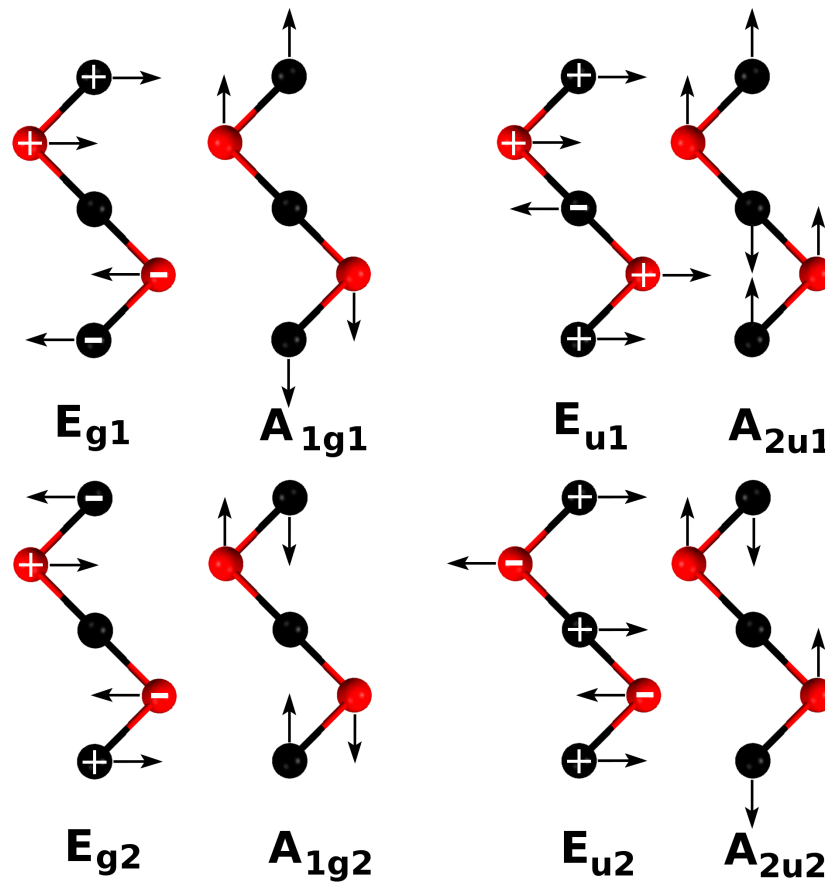


Figure 2.7: Optical phonon modes in Bi_2Te_3 . The “+” and “-” signs in presented figure describe motions toward and from the observer.

table.2.2. The structure of this compound with three inequivalent positions give rise to three acoustic phonon modes and twelve optical phonon modes. With two distinguish subgroups Raman active A_{1g} and E_g and two Infra-red active A_{1u} and E_u [41].

Chapter 3

Samples preparation

In this chapter, we will describe the process of crystal growth with a prime focus on the molecular beam epitaxy technique. In the central section, we will present the developed techniques of deposition Bi_2Te_3 ultra-thin films as well as we will go into detail regarding the preparation of samples used in this work.

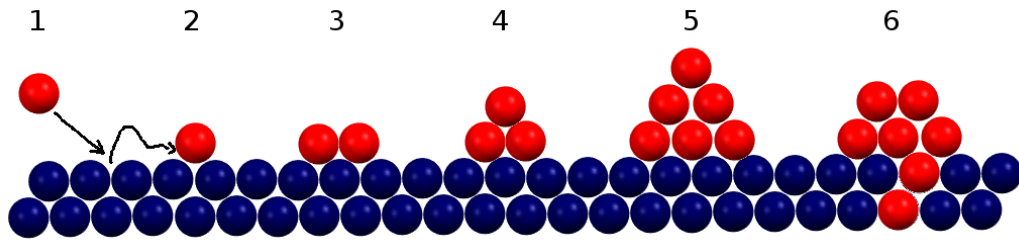


Figure 3.1: Steps of thin film growth: 1 - absorption, 2 - surface diffusion, 3 - chemical bond formation, 4 - nucleation, 5 - microstructure formation, 6 - bulk changes.

3.1 Growth of ultra thin films

We can differentiate 6 different steps in crystal growth Fig.3.1[42]. The first one the absorption or physisorption when approaching atom can be either reflected or absorbed on the top of the substrate surface. This step strongly depends on the rate of the flux of incoming atoms, the trapping probability, and the sticking coefficient.

In the second step of the crystal growth, overall surface energy is being minimized by atoms which have enough energy to diffuse to low energy site. This step is strongly governed by the temperature of the surface, through a diffusion rate k_s that increases with the temperature [42]. The diffusion length of relaxing atoms has the following form:

$$\Lambda = a\sqrt{k_s t}$$

where t is the diffusion time, and a is the hop distance. Λ at low temperatures increase with temperatures, while at higher temperatures desorption from the substrate overtakes the absorption causing the Λ to shorten. Typical diffusion lengths for physisorption is $300\mu m$ while for chemisorption this distance is much shorter $5nm$ [42].

In the third step after being physisorbed, the atom can start to chemically bond (chemisorption) to molecule-molecule or substrate-molecule or desorbed from the surface. In order for the atom to be either physisorbed or chemisorbed, it has to overcome local energy barriers (Fig.3.2). Arriving atoms that manage to attach to the surface create tension (energy) in the

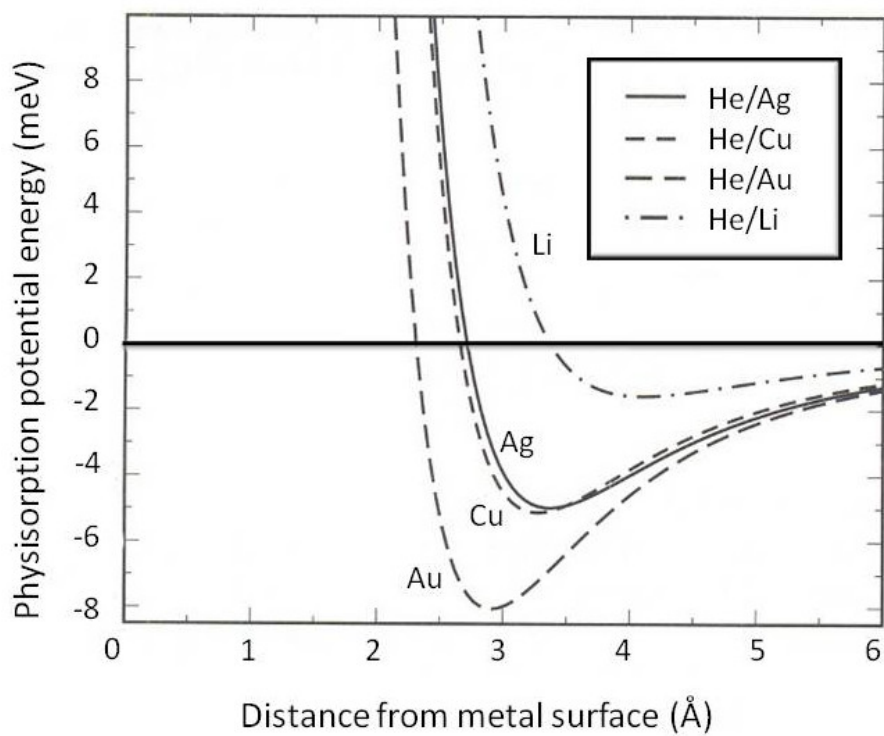


Figure 3.2: Physisorption potential energy for Helium calculated for various metal substrates (from E. Zaremba et.al [43]).

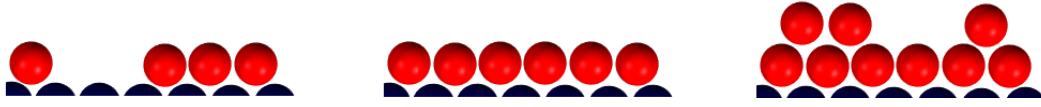


Figure 3.3: Frank van der Merwe crystal growth - Layers.

surface by stretching the bonds of substrate atoms. Such energy is a function, of broken bond energy of the top layer atoms, which depends on the crystal structure of the used substrate. We can distinguish two main types of substrate structures used for the growth process. That is a heteroepitaxial structure where there is a strong mismatch between the crystal structure and homoepitaxial where the crystal structure of both substrate and grown material is very close or identical.

In the fourth step deposited material starts to create nuclei of the crystal. This step is extremely critical to create a stable film. In the case of too small nuclei, the total surface energy is overpowering the process of proper crystallization. We can say that the nuclei have optimal size when by adding additional molecules, we can decrease Gibb's free energy. We can distinguish two types of nucleation undesirable one Homogeneous, which is a rare occurrence [42]. Where the free energy of the atoms in a gas form is smaller than when they are nucleated. The second one desirable so-called Heterogeneous, where the nucleation on the substrate surface reduces Gibb's energy by reducing the surface area. Nucleation processes are strongly dependent on the substrate temperature, which determines the size of the crystal embryos but increases the barrier for nucleation. As well as depend on the deposition rate. With a higher deposition rate, the critical size of the nuclei decreases but the energy barrier for nucleation diminish. Rate of the process of nucleation N depends on three parameters:

$$N = N^* A^* \omega$$

N^* the equilibrium concentration of stable nuclei, A^* critical area of embryos and ω the rate in which the incoming atoms cover said area.

In the fifth step, when the nuclei are big enough, they start to merge in one of the following ways. Large particles are taking the material from small ones (Ostwald Ripening). Two nuclei are forming a neck between each other. The shape of the neck allows for faster growth and merging of both nuclei (Sintering). Nuclei can as well undergo surface diffusion; when both nuclei are in local energy minimum, they will align and merge (Cluster Coalescence). The merging nuclei start to form the microstructures. We can distinguish three different kinds of film-forming. First one the Frank van der Merwe growth (Fig.3.3) where the layers tend to form uniform layers one by one. This growth happens when the substrate-vapor surface energy is larger than the total surface energy of the film. This results in a smooth film that wets the surface, decreasing the energy of surface tension. The second form of growth is Volmer Weber's growth (Fig.3.4.a), where the film starts to grow in island-like structures. This occurs when the entire surface energy of the interface is more significant than substrate-vapor energy. This situation leads to the conglomerating of film into islands. This condensation minimizes the surface area touching the substrate, and leads to uneven growth and very slow internal diffusion due to the accumulation of structural defects. Third type the Stranski-Krastanov growth is a mixture of the two (Fig.3.4.b). During this growth in the initial phase, the film is growing in a uniform layer, and after a few monolayers, it starts to grow island-like structures. This is the result of the straining of the initial layer near the interface with the substrate, where the grown layer starts to match the structure of the underlying substrate. This stress after a few layers start to relax changing in result the overall surface energy of deposited film [42].

In the last and final step, the deposited layer starts to relax. The structure of the film goes into a local minimum of the energy by diffusion of atoms. This relaxation process leads to the formation of defects within the layer and grain formation. Defects in crystals that are breaking the periodicity, by a shift of position, of single atoms or whole molecules or even entire grains can be divided into four separate categories. Point defects that occur within a single cell and do not expand in any direction; there are few defects in this category. Vacancy defect - where one of the positions in the unit cell is vacant. Surrounding crystal structure prevents the structure

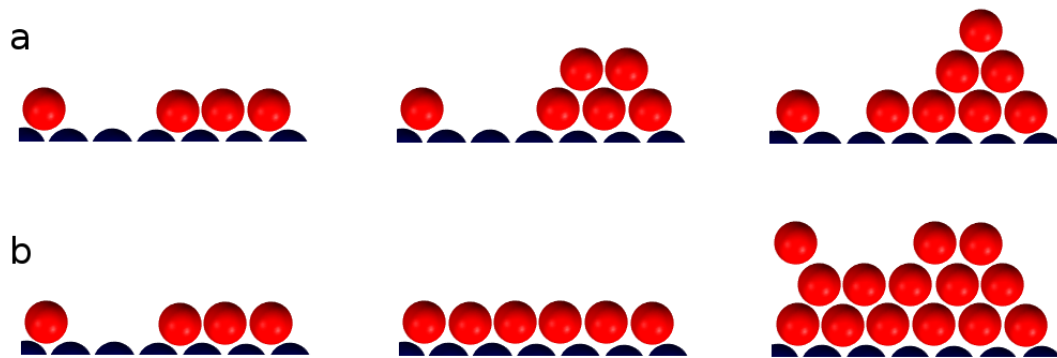


Figure 3.4: a - Volmer Weber crystal growth - Islands. b - Stranski-Krastanov crystal growth - Mixed

from collapsing. This type of defect is called as well Schottky defect. Antisite defect - where atoms of different type change places. Interstitial defect - which is caused by atom occupying a site that usually does not exist. Frenkel defect - when the interstitial and vacancy defect occurs at the same place. Line defects that are dislocations of entire planes of the crystal. We can distinguish two main types of this defect. Edge dislocation that is a termination of QL within the crystal, causing the adjacent planes to bend around it. Screw dislocation is a spiral-like growth of the planes of the crystal where each layer has a slightly different angle of growth. Planar defects include all grain formations such as boundary defects between grains where the direction of lattice abruptly changes. Stacking faults occur when a local change of the stacking sequence in the complex crystal is changed. Twin boundaries happen where neighboring grains possess mirror symmetries to each other. To this category, we can also include step formation between atomically flat terraces. The last group of the defect is a bulk defect that includes formations of pores, cracks, and inclusions. This group includes as well voids in the crystal structure and clusters of impurities so-called precipitates.

3.2 Molecular beam epitaxy (MBE)

All samples described in this work are thin films prepared by thermal evaporation in the Molecular Beam Epitaxy chamber (Fig.3.5 for an overview of the samples see table 3.1.). In MBE, the material is evaporated under high vacuum ($10^{-9} - 10^{-12}$ mbar) from effusion cells, forming molecular beams that are incident upon a heated sample. Lack of carrier gases and ultra-high vacuum environment makes the MBE the best method for creating the highest purity grown films. A typical MBE vacuum chamber effusion cells are situated directly underneath the substrate. Cells are equipped with shutters covering them to enable control over which material is being deposited. Typical effusion cells consist of a crucible for the source material and a heating source. There are two types of heating used in such effusion cells that is ohmic heating from a filament wound around the crucible or by electron beam heating. In the case of an electron beam, heating electrons from the cathode are accelerated through a potential of a few kV toward the material usually in the shape of a thin cylinder. Such a technique allows depositing large amounts of power, generating heating in the source material up to 2400°C . The evaporated material is then directed on to the sample manipulator on which samples are mounted. Such a manipulator allows rotation of the sample, which is necessary to create uniform coverage of the produced layer. Typical sample holder consists of the substrate, onto which the material is deposited, and includes heating system. Holder typically has one of two forms of heating: resistive up to 1000°C or by the electron beam.

Presented above chamber (Fig.3.5) was used in our experiments and is equipped with RHEED (reflected high energy electron diffraction, described in 4th chapter), quartz microbalance and mechanical shutter. The quartz crystal microbalance (QMB) measures the change of mass of deposited material per unit area by detecting the variations in the frequency of a quartz crystal resonator. Thanks to the high precision of this device, it is possible to achieve stable rates with extremely low flux with a precision of 10^{-5} Å/s. The mechanical shutter allows us to cover parts of the substrate during the deposition. This gives us the ability to create steps on the sample, regions with different thickness or partially cover the sample with different material.

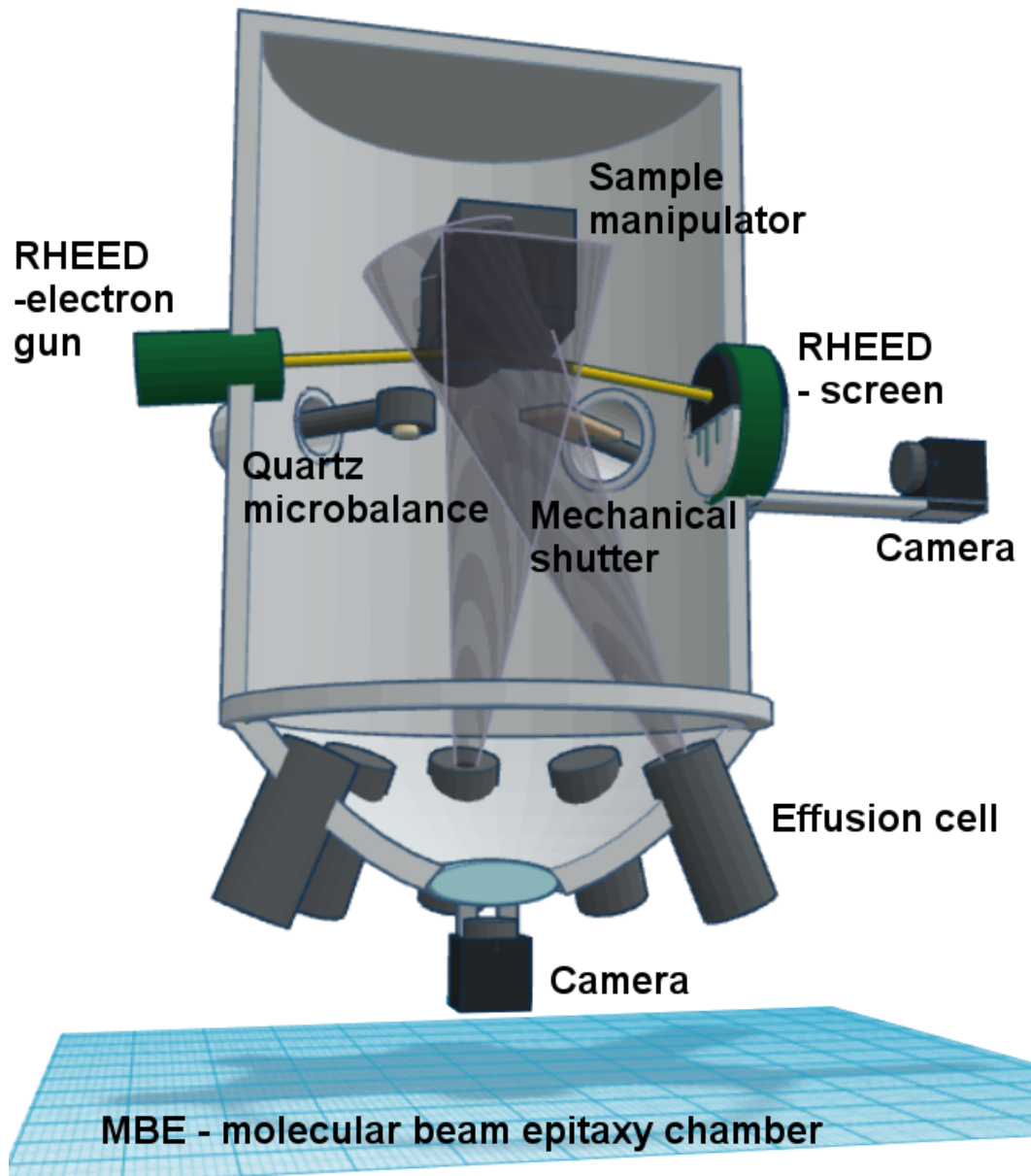


Figure 3.5: Model of MBE chamber used in our experiments.

MBE deposition rate (typically less than 30 000 Å/h) allows the films to grow epitaxially, which is layer by layer. With a growth strictly imposed by the substrate. In industrial applications, it is required that the deposited material will create a crystalline overlayer with a well-defined orientation to the substrate crystal structure. We can distinguish two main types of epitaxy. First, one the Homoepitaxy where the substrate has the same crystallographic structure as the deposited material or the structure is very close to it; this type includes deposition of the same material as a substrate to achieve for example a different kind of doping. Heteroepitaxy is an epitaxy where the substrate crystallographic structure differs from the deposited material; this sometimes allows the to make the grown layer take a different not achievable by other means of crystallographic orientations.



Figure 3.6: High vacuum cluster in laboratory of Surface Physics in Institute of Physics, University of Silesia.

3.3 Sample description

As previously mentioned all samples described in this work are thin films prepared by thermal evaporation in the Molecular Beam Epitaxy chamber from PREVAC company, which is part of a high vacuum cluster in the laboratory of Surface Physics in ŚMCEBI in Chorzów. Samples were made using two different substrates, Muscovite mica (110) (Ted Pella. Inc.) and silicon (001), and two different growth methods [30] [44]. The core objective of our project was an investigation of electric carriers dynamics of TI in extremely thin layers and near the metallic interface, in case of our project with the Fe layer. Finding the correlation between structure and physical functionality of such junctions is crucial for the fundamental understanding of the physical processes behind the spin transport as well as application in new technology. Most of our samples were grown on Muscovite mica, which allowed us to grow monocrystalline layers of topological insulator Bi_2Te_3 efficiently. This substrate, aside from providing optimal conditions for the growth of the films, also provides excellent thermal and electric insulation of grown layer, with excellent optical properties which are crucial for time-resolved femtosecond laser spectroscopy. For the processes of growth Bi pieces of purity, 99.999% (Aldrich Chem. Co.) and spectrographically standardized Te ingots (Johnson Matthey Chemicals) were used as a deposition source in standard effusion cells in all discussed processes of growth. The Fe wire of purity 99.999% (Aldrich Chem. Co.), was evaporated

Table 3.1: Characteristics of growth of the samples.

Name	Substrate	Plane	Substrate temp. [$^{\circ}C$]	<i>Bi</i> dep. rate	<i>Te</i> dep. rate	Thickness
A_1	Mica	(110)	$120^{\circ}C$	0.0145 Å/s	0.0210 Å/s	15 nm
A_2	Silicon	(001)	$130^{\circ}C$	0.0090 Å/s	0.0380 Å/s	10 nm
A_3	Silicon	(001)	$130^{\circ}C$	0.0140 Å/s	0.0200 Å/s	10 nm
B_1	Mica	(110)	$120^{\circ}C$	0.0145 Å/s	0.0210 Å/s	15 nm
B_2	Mica	(110)	$120^{\circ}C$	0.0145 Å/s	0.0210 Å/s	15 nm
C_1	Mica	(110)	$120^{\circ}C$	0.0145 Å/s	0.0210 Å/s	15 nm
C_2	Mica	(110)	$120^{\circ}C$	0.0145 Å/s	0.0210 Å/s	15 nm

with an electron cell. The deposition process was held under ultra-high vacuum conditions; the pressure during the growth did not exceed the level of $5 \cdot 10^{-9}$ mbar.

Sample A1 - reference sample - was made with a standard technique described in our previous works. That is the Muscovite mica with (110) plane which was cleaved and mounted on a standardized sample holder for resistive heating from PREVAC company and inserted into the system. After an introduction into the vacuum environment, the holder was slowly reheated to $120^{\circ}C$ in order to degas it and remove the impurities that might be stuck on the surface. After the primal cleaning, the temperature of the substrate was risen to $250^{\circ}C$ for at least 1h to remove any remaining residue and reorganized the surface thoroughly. The substrate was then left at $120^{\circ}C$ for at least 12h. The temperature during the deposition process was kept at $120^{\circ}C$. The rates of the Bi and Te vapor flux were controlled with quartz crystal microbalance and were kept at 0.0145Å/s for bismuth and 0.0210Å/s for tellurium, which gives a correct ratio of 2:3 structure of Bi_2Te_3 . The total flux of the molecular beam was 0.0355Å/s; such flux was maintained for the duration of 1h 15min to achieve a 15nm layer of the Bi_2Te_3 . Layer after the deposition was left at $120^{\circ}C$ overnight to reorganize its crystal structure.

Sample A2 - polycrystalline sample on silicon - sample was prepared according to the tech-

nique described by Rapacz et.al. The silicon wafer was cut with a diamond pen and cleaned in a solution of isopropanol in an ultrasound bath. After that, it was reheated on the hotplate up to 200°C for an hour; then the substrate was mounted on a standardized sample holder for resistive heating from PREVAC company and inserted into the system. After an introduction into the vacuum environment, the holder was slowly reheated to 130°C in order to degas it and remove the impurities that might be stuck on the surface. The substrate was then left at 130°C for at least 12h. The temperature during the deposition process was kept at 130°C . The rates of the Bi and Te vapor flux were kept with quartz crystal microbalance and were maintained at $0.0090\text{\AA}/\text{s}$ for bismuth and $0.0380\text{\AA}/\text{s}$ for tellurium. The total flux of the molecular beam was $0.0370\text{\AA}/\text{s}$; such flux was maintained for the duration of 35min to achieve a 10nm layer of Bi_2Te_3 . Layer, after the deposition, was left at 100°C overnight to reorganize its crystal structure.

Sample A3 - polycrystalline sample on silicon - sample was prepared according to the technique described by Rapacz et.al. The silicon wafer was cut with a diamond pen and cleaned in a solution of isopropanol in an ultrasound bath. After that, it was reheated on the hotplate up to 200°C for an hour, then substrate mounted on a standardized sample holder for resistive heating from PREVAC company and inserted into the system. After the introduction into the vacuum environment, the holder was slowly reheated to 130°C in order to degas it and remove the impurities that might be stuck on the surface. The substrate was then left at 130°C for at least 12h. The temperature during the deposition process was kept at 130°C . The rates of the Bi and Te vapor flux were maintained with quartz crystal microbalance and were kept at $0.0140\text{\AA}/\text{s}$ for bismuth and $0.0200\text{\AA}/\text{s}$ for tellurium. The total flux of the molecular beam was $0.0340\text{\AA}/\text{s}$; such flux was maintained for the duration of 50min to achieve a 10nm layer of Bi_2Te_3 . Layer, after the deposition, was left at 100°C overnight to reorganize its crystal structure.

Sample B1 - step sample Fig.3.7. - was made with a standard technique with slight modification. Mica substrate, in order to achieve better quality of the surface, was separated with

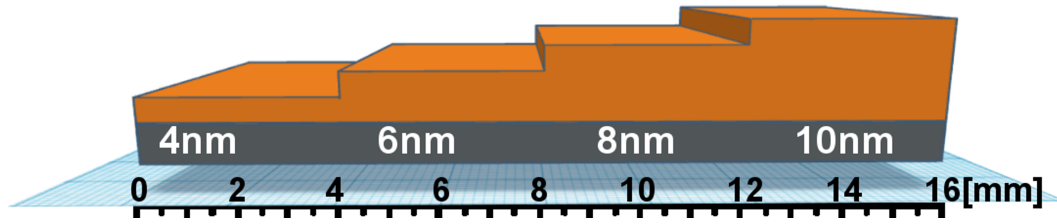


Figure 3.7: Sample B1 - art view of monocrystalline sample of Bi_2Te_3 with terraces' thickness of 4, 6, 8 and 10nm .

scotch tape to ensure a lack of additional terraces and perfectly smooth substrate with orientation (110). After this substrate was mounted on a standardized sample holder for resistive heating from PREVAC company and inserted into the system, after the introduction into a vacuum environment, the holder was slowly reheated to $120^\circ C$ in order to degas it and remove the impurities that might be stuck on the surface. After the primal cleaning, the temperature of the substrate was risen to $250^\circ C$ for at least 1h to remove any remaining residue and reorganized the surface completely. The substrate was then left at $120^\circ C$ for at least 12h. The temperature during the deposition process was kept at $120^\circ C$. The rates of the Bi and Te vapor flux were controlled with quartz crystal microbalance and were kept at 0.0145 \AA/s for bismuth and 0.0210 \AA/s for tellurium, which gives a correct ratio of 2:3 structure of Bi_2Te_3 . The steps on the sample were achieved by creating the shadow over the substrate with an integrated manipulator within the MBE chamber. The procedure to achieve the step structure was as follows: after the stabilization of the effusion cells. The total flux was kept at 0.0355 \AA/s , at which point both shutters were opened to substrate plate; after 19min, the mechanical shutter was shifted by 4mm, in order to stop the growth over the region with 4nm step; after each 19min, the mechanical shutter was shifted by another 4mm up to the layer with 10nm of thickness at which point after the elapsing of 19 minute mark, the effusion cells where covered. The layer after the deposition was left at $120^\circ C$ overnight to reorganize its crystal structure.

Sample B2 - wedge sample Fig.3.8 - was made with a standard technique with a slight

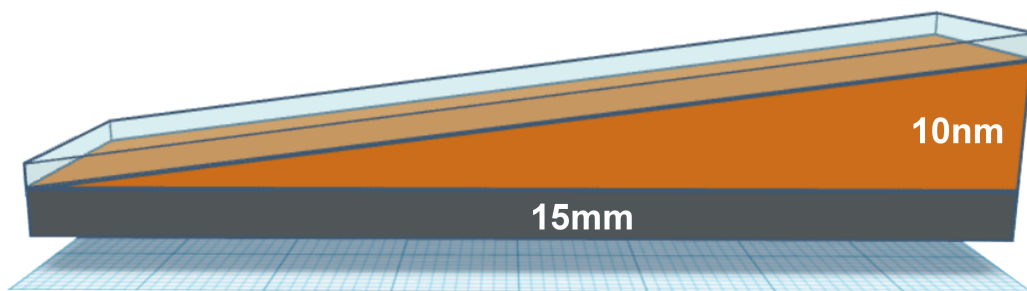


Figure 3.8: Sample B2 - art view of monocrystalline wedge of Bi_2Te_3 with slope of 0.66nm/mm.

modification. Mica substrate, in order to achieve better quality of surface, was separated with scotch tape to ensure a lack of additional terraces and perfectly smooth substrate with orientation (110). After this, the substrate was mounted on a standardized sample holder for resistive heating from the PREVAC company and inserted into the system. After an introduction into the vacuum environment, the holder was slowly reheated to $120^{\circ}C$ in order to degas it and remove the impurities that might be stuck on the surface. After the primal cleaning, the temperature of the substrate was risen up to $250^{\circ}C$ for at least 1h to remove any remaining residue and reorganized the surface effectively. The substrate was then left at $120^{\circ}C$ for at least 12h. The temperature during the deposition process was kept at $120^{\circ}C$. The rates of the Bi and Te vapor flux were maintained with quartz crystal microbalance and were kept at $0.0145\text{\AA}/s$ for bismuth and $0.0210\text{\AA}/s$ for tellurium, which gives a correct ratio of 2:3 structure of Bi_2Te_3 . The procedure to achieve the wedge sample was as follows: after the stabilization of the vapor flux at $0.0355\text{\AA}/s$, the mechanical shutter was moved with the motor with speed of $0,005\text{mm}/s$ during the time of 47min until the shutter completely covered the sample and we achieved the maximal thickness of 10nm; due to this procedure it was possible to get a sample with gradient of thickness 0,66 nm/mm; layer, after the deposition, was left at $120^{\circ}C$ overnight to reorganize its crystal structure.

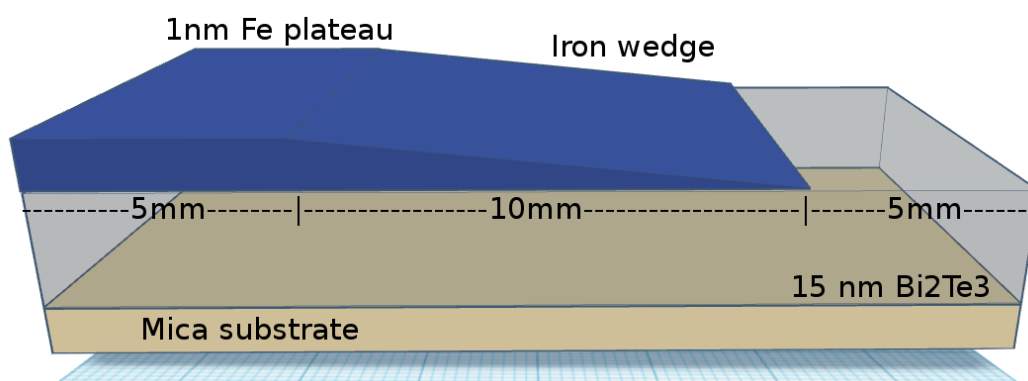


Figure 3.9: Sample C2 - art view of monocrystalline sample of Bi_2Te_3 with 3 sections: 1st - plateau of iron with a thickness 1nm and length 5mm; 2nd - wedge of iron with gradient $1\text{\AA}/\text{mm}$; 3rd - free surface sample of BT.

Sample C1 - iron oxide cover - sample was made with the standard technique the same way as described for sample A1. The temperature during the deposition process was kept at 120°C . The rates of the Bi and Te vapor flux were maintained with quartz crystal microbalance and were kept at $0.0110\text{\AA}/\text{s}$ for bismuth and $0.0160\text{\AA}/\text{s}$ for tellurium, which gives a correct ratio of 2:3 structure of Bi_2Te_3 . The total flux of the molecular beam was $0.0270\text{\AA}/\text{s}$; such flux was maintained for the duration of 1h 30min to achieve a 15nm layer of the Bi_2Te_3 . The layer after the deposition was left at 120°C overnight to reorganize its crystal structure. After one day, a layer of iron was deposited on half of the clean Bi_2Te_3 surface. Iron was deposited at the rate of $0.063\text{\AA}/\text{s}$ during the time of 160s, which resulted with capping layer of iron with thickness 1nm.

Sample C2 - iron oxide wedge Fig.3.9 - sample was made with the standard technique the same way as described for sample A1. The temperature during the deposition process was kept at 120°C . The rates of the Bi and Te vapor flux were controlled with quartz crystal microbalance and were kept at $0.0137\text{\AA}/\text{s}$ for bismuth and $0.0201\text{\AA}/\text{s}$ for tellurium, which gives a correct ratio of 2:3 structure of Bi_2Te_3 . The total flux of the molecular beam was $0.0338\text{\AA}/\text{s}$;

such flux was maintained for the duration of 1h 15min to achieve a 15nm layer of the Bi_2Te_3 . The layer after the deposition was left at $120^\circ C$ overnight to reorganize its crystal structure. After one day, iron plateau and wedge were deposited on top of the Bi_2Te_3 leaving a 5mm wide region without iron for comparison. The rate of iron was kept at $0.00872\text{\AA}/s$ during 19min; during this time, the automated manipulator was exposing the layer to create the wedge sample with a speed $0,0087\text{mm}/s$.

3.4 Summary

By employing molecular beam epitaxy, we successfully created high-quality ultra-thin films of Bi_2Te_3 that allowed us to tackle different questions concerning the properties of this material. Samples from group A consist of three samples, one deposited on Muscovite Mica, and two deposited on Silicon (001). During their growth, we used different rates of the molecular beam flux, as well as different temperatures of growth. That allowed us to see how the change of this parameters influences the quality of grown material as well as probe the electron-phonon coupling and phonon dynamics that may play a crucial role in the development of future devices [27, 28].

The second group B of the thin film was created for a better understanding of the critical thickness of the Bi_2Te_3 [9, 31, 32, 33]. In order to answer this question, we prepared two samples deposited on Muscovite Mica with different geometry: one with large steps (that grants us access to the large surface area with uniform thickness) and the second one with continuous slope (that allows us to conduct experiments with a higher number of investigated spots). We believe that such geometries are optimal for investigation of the critical thickness influence on the behavior of photoexcited hot carriers as well as allow us to understand the growth process of the material better.

The last group C of the synthesized films was made in order to understand the chemical

reactions and physical phenomena induced by the proximity to the oxidized iron layer [34]. Due to the considerable interest of the community in the creation of devices based on the topological insulator phenomena [5, 6, 7], it is crucial to understand the fundamental interactions (both chemical and physical) of materials showing these effects near other non-trivial, in a topological sense, interfaces. In our study we have chosen the iron oxide as the covering layer, and we have created two samples: one with a uniform thin cap of iron ($\sim 1\text{nm}$) covering half of the sample and second, similar to sample B2, with a uniform continuous wedge of iron ($1\text{nm} \rightarrow 0\text{nm}$) deposited on a 15nm layer of Bi_2Te_3 . Such configuration gives us means to directly compare the effects induced by the presence of other material on both crystal structure as well as phonon and hot carrier dynamics. Using half of the sample as the reference, we can eliminate effects that could be induced by different growth conditions and give us a chance to compare the measured signals directly.

Chapter 4

Diffraction and continuous spectroscopy techniques

In this chapter, we will focus on continuous spectroscopy techniques used to characterize the samples of Bi_2Te_3 . We will describe as well the techniques that were used for the characterization of our samples, and we will discuss the most exciting results.

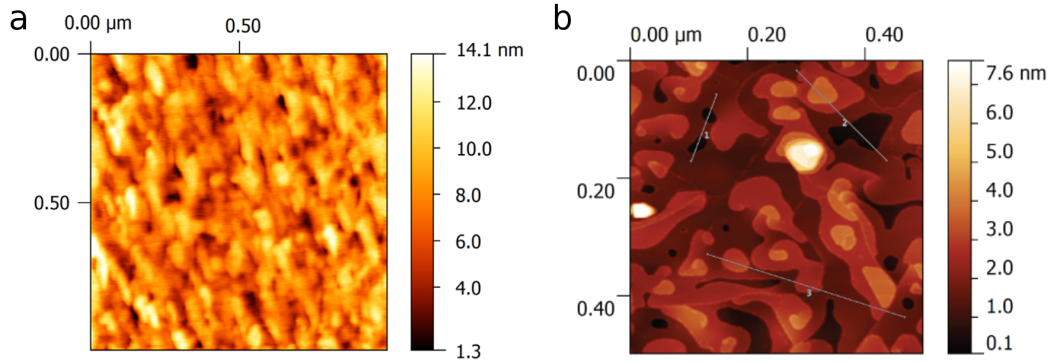


Figure 4.1: a - $1 \times 1 \mu\text{m}$ AFM image of sample A2, Bi_2Te_3 grown on Si(001). b - $0.45 \times 0.45 \mu\text{m}$ AFM image of sample A1 grown on Muscovite mica (110). From R.Rapacz [30]

4.1 Surface structure analysis

One of the leading fields in modern physics is surface structure analysis, especially at the nanoscale. In our arsenal, we now possess a broad spectrum of different ways to characterize the physical aspects of this region. One of the most prominent group is the scanning probe microscopy (SPM) with atomic force microscopy (AFM) technique and scanning tunneling microscopy (STM). The resolution of those microscopes is not limited by diffraction, but mostly by the size of the probe-sample interaction volume. Hence the ability to measure small local differences in object height like 1nm steps on Bi_2Te_3 (Fig.4.1.b). Unlike electron microscopy methods, some modes in this group do not require a partial vacuum but can be efficiently be used in air. However, the most prominent advantage of this type of measurement is a wide diversity of techniques, which allow additional characterizations of measured samples. For example, we can measure local conductivity or magnetic and ferroelectric domain structure.

Second group of methods, widely used for surface characterization, are different kinds of electron diffraction methods, which provide us with information about crystal order in measured samples. To this group belong LEED and RHEED techniques, that were used in our

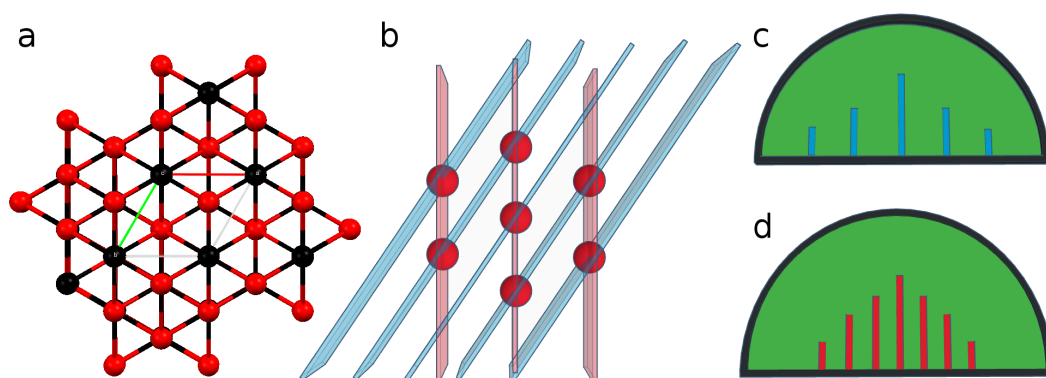


Figure 4.2: a - View on the c plane (001) of Bi_2Te_3 cell. b - Two main symmetry planes in the hexagonal cell, the difference between them is precisely 30° . c and d - Artistic representation of diffraction pattern made with RHEED along with two main symmetries, colors are corresponding to the planes marked in picture b; the received pattern is in reciprocal lattice.

experiments. Low energy electron diffraction is based on the detection of diffracted electrons from the collimated monoenergetic beam. The image is created by electrons elastically scattered back towards the electron source. The spatial distribution of the intensity maxima is determined strictly by the surface structure. Positions of the intensity maxima correspond to the lattice structure of the surface represented in reciprocal space.

4.1.1 Reflection high-energy electron diffraction (RHEED)

Reflective high energy electron diffraction method gives us information about the long-range order of the sample surface in the plane perpendicular to the beam incidence plane. Namely, if the sample is monocrystalline or polycrystalline or possesses some texture, additionally RHEED can be employed in the measurement of the thickness of samples grown in the MBE chamber. RHEED because of its small penetration depth, caused by the interaction between incident electrons and atoms, is mainly sensitive to the atomic structure of the first few planes of a crystal lattice. This feature is especially useful for quick identification of grown

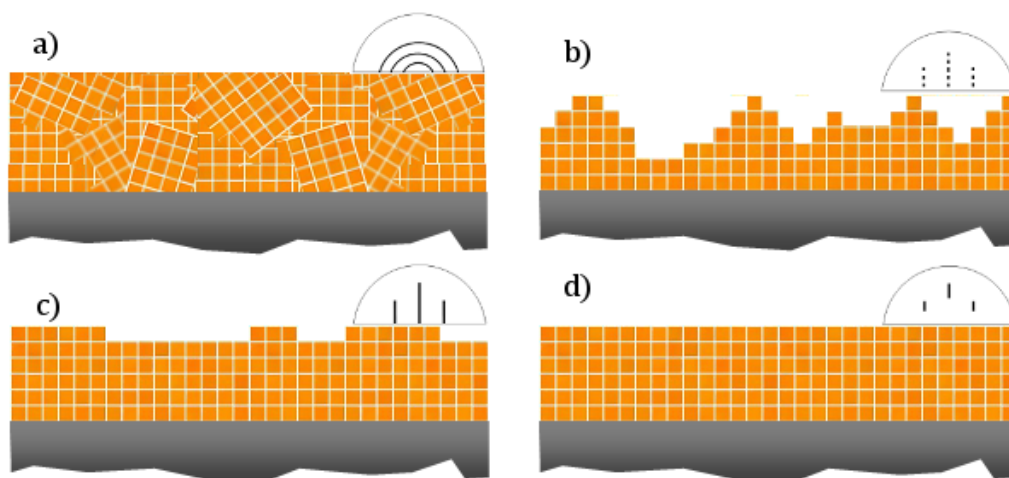


Figure 4.3: RHEED diffraction image from: a) Polycrystalline sample; b) Monocrystalline sample with additional 3D structures (for example islands or quantum dots); c) Monocrystalline structure with small terraces; d) Monocrystalline and perfectly flat structure .

film, for example (Fig.4.2) hexagonal structure of Bi_2Te_3 possess two characteristic RHEED patterns, which differ from each other by 30° rotation, what in result creates 60° repetition of each pattern.

Because of RHEED geometry incident beam is directed at a low angle to the surface and has a powerful effect on both the diffraction and its interpretation. When the atomic defects are parallel to the incident beam direction, they can produce significant changes in both the measured intensity and the shape of the diffracted beams, for example, atomic steps (Fig.4.3.c). In contrast, the atomic structure in the diffracted intensity is mainly determined by the atomic structures perpendicular to the incident beam. Both of those phenomena are originating from the shallow glancing angle of the incidence beam.

Additionally, RHEED diffractometer can detect intensity changes of a diffracted electron during the growth of the layer in the MBE chamber, that can be used to follow in time the thickness of deposited layers. Our experiments, using this technique, have shown linear changes

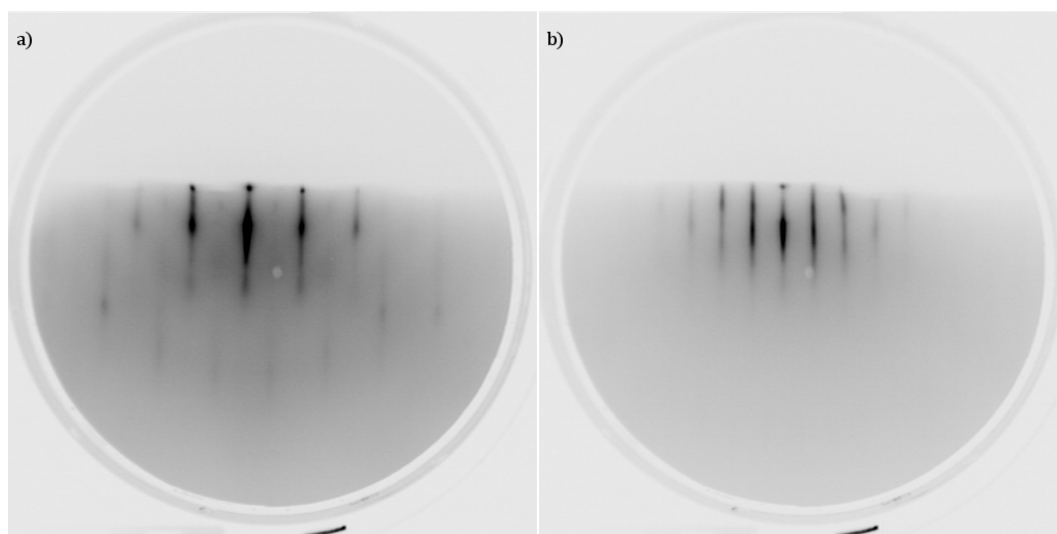


Figure 4.4: RHEED diffraction image of sample A1 along two main planes of symmetry characteristic to Bi_2Te_3 hexagonal crystal structure. Detected streaks are proof of monocrystalline terrace growth of the sample.

with a lack of any periodicity accustomed to Frank van der Merwe crystal growth (the growth layer by layer). This result pointed to us in two possible mechanisms of growth of our samples that are either Volmer Weber (growth in island formations) or Stranski-Krastanov (mixed) crystal growth dynamic [42].

All samples were measured on RHEED from STEIB Instruments in situ environment, just after the growth of the samples. The analysis was performed with RHEED Vision v5.6.6 software. Sample, A₁ diffraction image Fig.4.4, shows characteristic symmetries of hexagonal structure (difference of 30°), and appearance of streaks suggests high-quality surface, similar to all samples from group B and C. Received results are a direct proof that technique, employed during the growth, is optimal for creation of very smooth and monocrystalline thin films of Bi_2Te_3 . Samples, grown on silicon substrate A₂ Fig.4.5.a and A₃ Fig.4.5.b, exhibit formation of polycrystalline structure, which is mainly caused by a mismatch between Bi_2Te_3 and silicon (001). Film A₃ possesses additional streaks, which suggest the creation of some

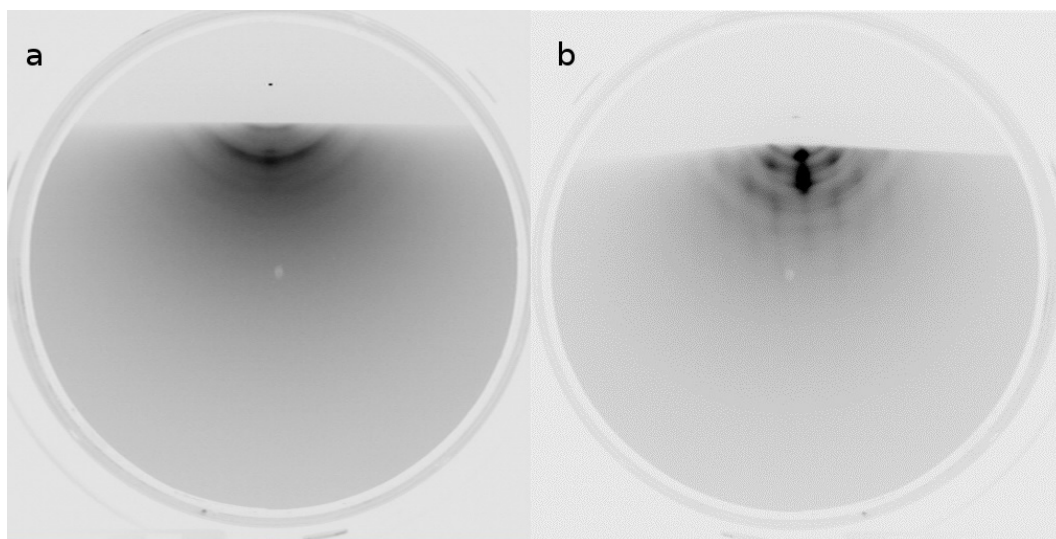


Figure 4.5: RHEED diffraction image of sample a - A2 and b - A3. Observed half circles are proof polycrystalline growth of the sample.

long-range ordering on the film. Both groups of samples B and C were grown with the same parameters of growth as the sample A1. In the case of sample B2 Fig.4.6.a, we can observe similar streaks corresponding to one of the characteristic diffraction patterns of the hexagonal crystal. The broadening is caused by the presence of planned steps in the structure. For both samples B1 and B2, due to their unique configuration with changing thickness and placement on the sample holder, it was impossible to get an image from all the angles. In the case of samples from batch C, they all showed a uniform single crystalline structure of Bi_2Te_3 with smooth terraces of nm height Fig.4.6.b This is a proof of deposition quality repeatability using the method developed by our group.

4.1.2 Low energy electron diffraction (LEED)

LEED (low energy electron diffraction) is a technique in which a beam of electrons, ejected from an electron gun, probes a measured sample. The main components of the LEED are elec-

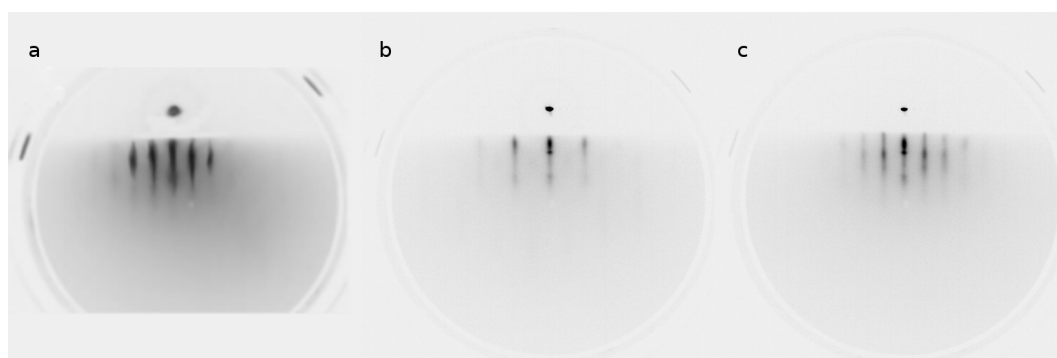


Figure 4.6: a - RHEED diffraction image of sample B2 along principal planes of symmetry characteristic to Bi_2Te_3 hexagonal crystal structure. Observed streaks are proof of monocrystalline terrace growth of the sample. b and c - RHEED diffraction image of sample C2 along two principal planes of symmetry characteristic to Bi_2Te_3 hexagonal crystal structure. Observed streaks are proof of monocrystalline terrace growth of the sample.

tron gun and fluorescent screen on which we observe registered diffraction patterns. Electron gun consists of two main parts, first is the heated cathode, which is an emitter of electrons and second, the array of focusing lenses. Such configuration allows generating a collimated beam of electrons with finely defined energy in the range $20 - 300eV$, which are then scattered in numerous different directions strictly dependant on the surface crystallography. After the diffraction, electrons go through 3 different grids before arriving at the phosphor covered screen. The first grid is grounded and acts as shielding for the second one. Second is a filter that passes only electrons with enough energy. Thanks to that electrons with lower energy, the image does not cloud or distort. The final grid acts as a barrier between the negatively charged second grid and positively charged screen. After that, electrons land on the screen, creating a glow in which intensity is strictly dependant on the intensity of the arriving electrons. Pattern, created by those electrons, is an image in reciprocal space of the measured structure.

LEED is one of the primary techniques in surface physics for the determination of grown structures. We can distinguish two ways in which we can analyze acquired data. The first

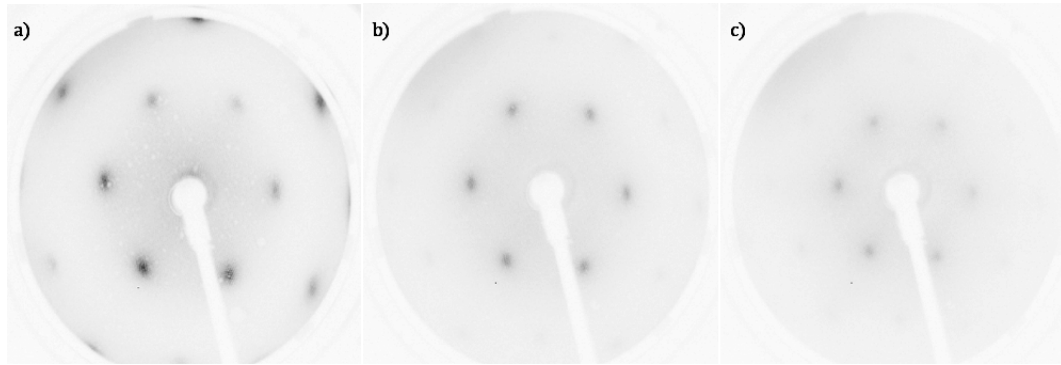


Figure 4.7: LEED diffraction image of sample A1 at different electron incident energies a) 56eV; b) 75eV; c) 98eV.

one used in this work is an analysis of the position of spots on the diffraction pattern. This method gives us information about symmetries, size, and rotational alignment of unit cells of our samples. The second one is the analysis of acquired spots intensities recorded as a function of incident electron beam energy. This allows generating so-called I-V curves which can be directly compared with theoretical models giving in result accurate information about atomic positions in the unit cell of the measured sample.

All described LEED measurements were performed in situ environment, in a short period after the thin film deposition, on INTEGRALEED model BDL800IR-LMX-ISH. Samples A2 and A3, because of their polycrystalline structures, did not give any diffraction images. Fig.4.7. shows diffraction pattern of sample A₁. The conducted experiment has proven that grown structure posses correct Bi_2Te_3 hexagonal structure. Slight diffusion of diffraction points might be caused by a slight mismatch between quintuple layers. Sample C₂ (Fig.4.8.) made with the same technique as sample A1 shows similar diffusion of diffraction points which might be characteristic for this method of growth. During this experiment, it was possible to observe ordered structure at low and high energy (up to 200eV). Above this high energy region diffraction spots were vanishing. The ability to observe diffraction spots to such energies proves the correct and monocrystalline structure of grown thin film underneath the topmost atomic layers.

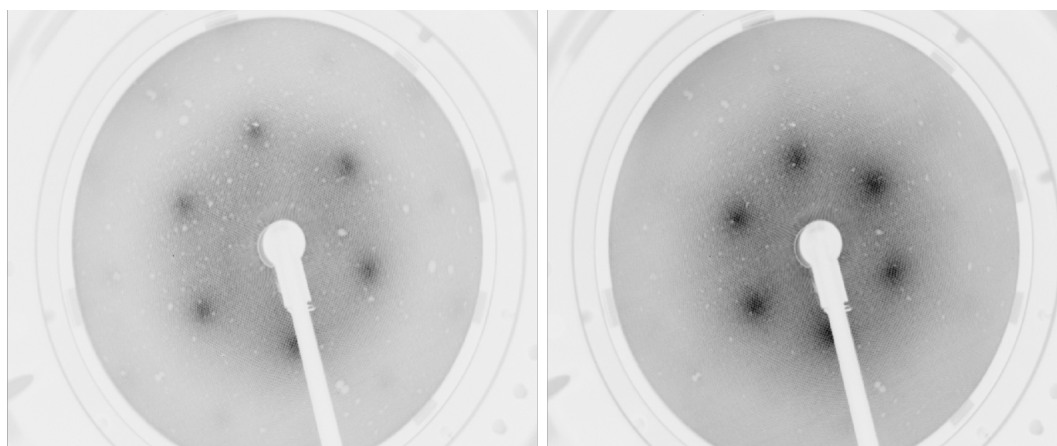


Figure 4.8: LEED diffraction image of sample C3 revealing characteristic Bi_2Te_3 hexagonal crystal structure. Broadening of the diffraction spots is a result of slight mismatch between nearest QL's.

LEED images have provided us with apparent information about the formation of crystal structure in the case of our growth method. Deposition of the sample with evaporation rates, similar to desired composition stoichiometry but with a lower temperature of the substrate, causes a slight mismatch between nearest QL's but on the other hand, gives us the excellent formation of Bi_2Te_3 structure.

To further analyze the nature of the crystal formation, we performed the low energy electron diffraction experiments on the step layer sample B2 in order to confirm the proper growth of the crystalline layer. A detailed LEED image on a 5 nm thick film is shown in Fig.4.9.a. Measurement confirmed the proper symmetry structure of the thin layer. In the region of 4nm thickness, the image started to become distorted because of the bending of the mica substrate.

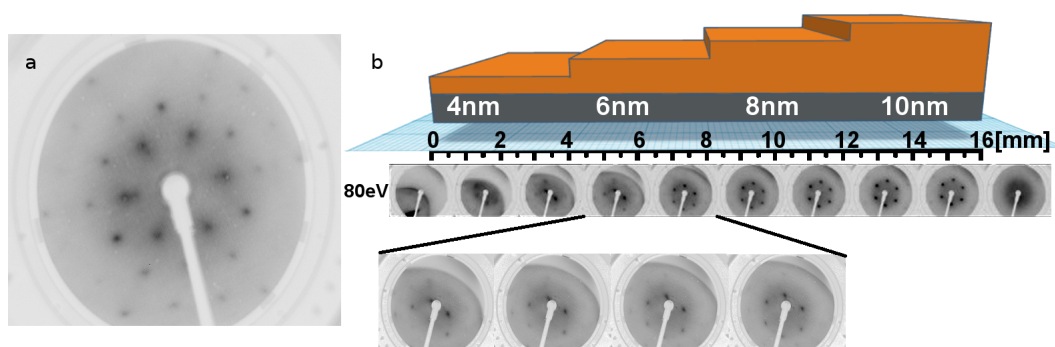


Figure 4.9: a - LEED of 5nm thickness sample at energy 115eV. b - Art view of the cross section of the step sample B2 with an inset in the bottom of the figure showing thickness dependence of LEED image obtained at energy 80eV.

4.2 Chemical and electron state analysis

In order to fully understand the physics hiding behind material like Bi_2Te_3 , we need to have well-defined samples. During the process of growth, the control over the rates of deposition is not always the same, and the stoichiometry of deposited film can vary even when using identical parameters. Even slight variations in the ratio of bismuth to tellurium can cause self doping of the material, and their polarity can be changed from p-type to n-type by increasing bismuth concentration in the film [45]. The ability of self doping of Bi_2Te_3 is used in industry to better harness its thermoelectric properties [46, 47, 48, 49].

Because of this property and direct modification of electron levels due to it, it is crucial to characterize chemical state of each sample well. In our case, each sample was thoroughly measured with X-ray photoemission spectroscopy. We put a particular focus on investigating the changes in the valence band and $Bi4f$ and $Te3d$ core level energy shift.

4.2.1 X-ray photo-electron spectroscopy

The photo-electron spectroscopy is one of the few methods which allows direct characterization of electronic and chemical states of the elements that exist inside the measured material. Emitted electron possesses very shallow penetration of measured sample, usually in the range of $0.5nm$ up to $2nm$. We can distinguish two separate methods by the energy of excited photons. Ultra-Violet Photo-electron Spectroscopy ($h\nu = 10 - 150eV$) and X-ray Photo-electron Spectroscopy ($h\nu = 150 - 3000eV$). Because binding energy decreases with the distance from the nucleus, UPS method is only used for characterization of valence band electrons, while XPS method can be employed for characterization of both core level electrons and valence band electrons.

In principle, the PES method works by excitation of sample with radiation with specific energy $h\nu$, and absorption of a photon by the material, followed by the transfer of its total energy to an electron. Changing the state of the electron from $|i\rangle$ to the state $|j\rangle$:

$$h\nu = E_j - E_i$$

Then, if the emitted electrons energy E_j is larger than the work function barrier ϕ excited electron can be emitted into the vacuum. Kinetic energy E_k of this particle is then measured with energy analyzer and is given by the Einstein equation:

$$E_k = h\nu - \phi - E_B$$

Work function ϕ is characteristic for each spectrometer and can be considered as constant, but the binding energy E_B of electrons depends on the type of atom from which electron was irradiated as well as the local chemical environment. Because each element possesses a characteristic structure of the atom, measurement of E_B can be used for the identification of elements and their chemical states in samples. The quantum mechanics gives the approximation of this energy (for multielectron atoms).

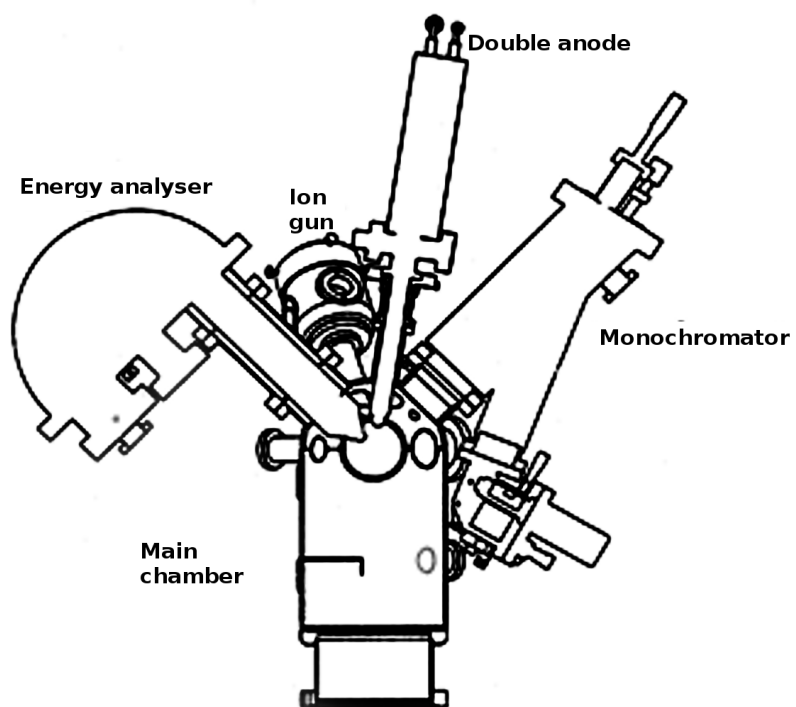


Figure 4.10: Schematic of *Physical Electronics PHI5700* spectrometer.

Samples group A

Conducted photo-electron spectroscopy studies were performed with the use of the monochromatized $AlK\alpha$ radiation using the PHI 5700 spectrometer from Physical Electronics Fig.10. All film after growth has been transferred in UHV from the MBE to the analysis chamber within minutes after deposition. The films studied in-situ showed no oxidation nor carbon contamination. The analysis spot had a diameter of 0.8 mm. The analysis of the spectra was done with the use of MULTIPAK program from Physical Electronics. The lines were fitted by Gaussian-Lorentz or asymmetrical lines. The same program was used to calculate the atomic concentration. During the measurements, we obtain the photoelectron spectra of $Bi4f_{7/2}$ and $Te3d_{5/2}$ core levels, as well as broad spectra in order to check the purity of grown films.

Analysis of the XPS spectra allowed us to determine the atomic composition and chemical state of the components (Table 4.1). All samples appear to be free of any contamination and the atomic composition characterized by the Bi/Te ratio spans from 33/67 (B_2) to 46/54 (A_1). The Bi_xTe_y system is known to form many-layered nanostructures especially for the compositions $y/x < 3/2$, in which stacking sequence of the quintuple layers, has additional interlayers of Bi and Te located in-between the BT QL's [50].

The calculations, together with the analysis of core levels, indicate that at the used growth conditions main phase of Bi_2Te_3 is formed with some addition of Te. In samples A_2, A_3 we observed the existence of two chemical states of Te, which can be associated with pure Te and the second one to the chemical state of Bi-Te compound. The observed chemical shifts (Table 4.1) exhibit similar trends for all examined films. The maximum of the $Bi4f_{7/2}$ peak is shifted, relatively to pure bismuth layer, towards higher binding energies while the $Te3d_{5/2}$ line is moved towards lower binding energies compared to pure Te film. The high-binding-energy $Bi4f_{7/2}$ states observed for the film A_1 at 157.31 eV, up to 157.56 eV for the film A_3 and are in close agreement with those reported by R. Rapacz [30]. Good agreement with those

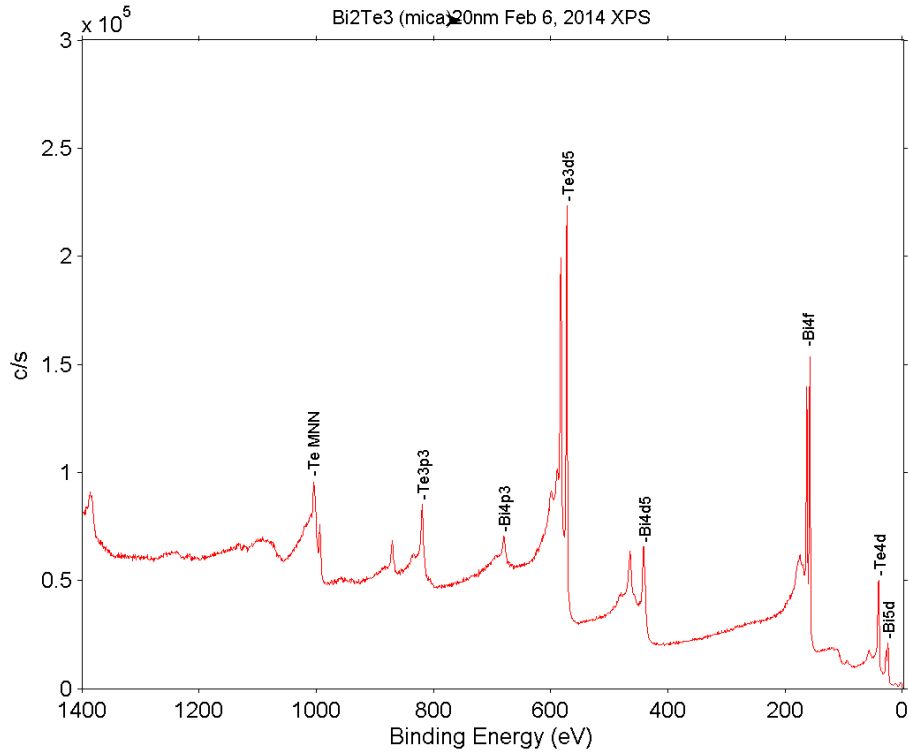

 Figure 4.11: Typical XPS spectra of pure Bi_2Te_3 sample.

Table 4.1: Summary of the atomic concentration calculations derived from the XPS data.

Sample	$Bi4f_{7/2}$			$Te3d_{5/2}$		
	Low_{Be} state	$High_{Be}$ state	At [%]	Low_{Be} state	$High_{Be}$ state	At [%]
E_B [eV]	E_B [eV]	E_B [eV]		E_B [eV]		
Tellurium	-	-	-	-	572.80	100
A_1	-	157.31	46	571.93	-	54
A_2	-	157.52	35	572.10	572.80	65
A_3	-	157.56	33	572.11	572.88	67
Bismuth	156.85	-	100	-	-	-

energies can also be observed for the $Te3d_{5/2}$ band. The low-binding-energy state spans from 571.93 eV for film A_1 up to 572.11 for film A_3 . Observed states of the main peaks of Te and Bi indicate the formation of Bi_2Te_3 .

Samples group B

As previously for group A the $Te3d_{5/2}$ and Bi 4f doublets and valence band were used for the analysis of the proper formation of the Bi_2Te_3 structure. In Fig.4.12 we presented the valence band where it is clear that thickness of the film does not influence this part of the electronic structure considerably but leads to shifting of the energy ($\sim 0.2eV$). Obtained spectra for core levels of $Te3d_{5/2}$ doublet (Fig.4.13.a) shows lack of distortion induced by the thickness, while for the $Bi4f_{7/2}$ level a small contribution from metallic Bi could be detected after fitting of the spectra for the films with thickness up to 8 nm. Fig.4.14 shows an example of the results of fitting for the 6 nm film. This fact correlates with the obtained atomic concentration which is rich in Bi, especially for the thickness of 4 and 6 nm:

Atomic concentration of grown films

Thickness	Tellurium	Bismuth
4 nm	49,5	50,5
6 nm	52,4	47,6
8 nm	52,1	47,9
10 nm	53,2	46,8

One of the possible reasons for the Te deficiency changing with the thickness of the films could be related to the desorption of Te at the initial stage of growth. According to the literature, the formation of additional Bi layers between QLs is a consequence of that process. The superstructure Bi-BT conserves the stable structure within the QLs [51]. The Te desorption may be

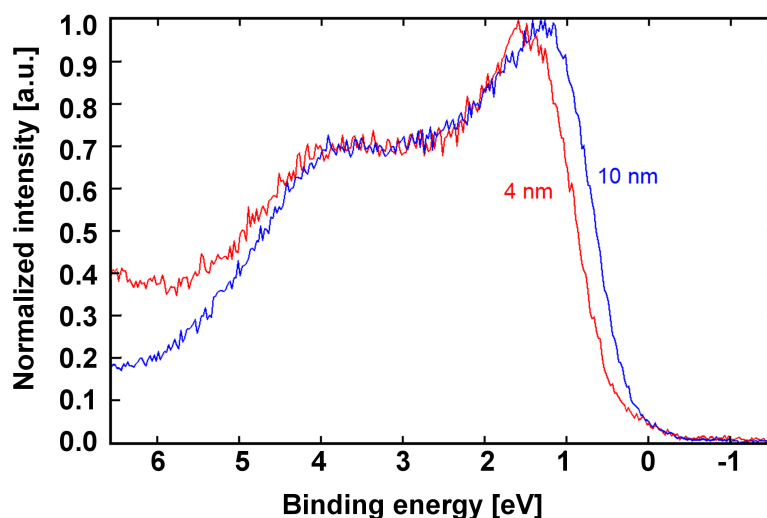


Figure 4.12: Valence band spectra for the as grown film with various thickness.

related to the latent heat of the compound formation which causes overheating of the deposited film. The effect will be most pronounced at the thinnest films because the heat transfer to the substrate is limited, and the mass of the deposited BT is minuscule. The interface BT-mica has the van der Waals character limiting the heat transfer to the substrate.

Another important issue is related to the fact that the optical measurements were performed ex-situ, for the samples oxidized at the surface. In order to estimate the effect of surface oxidation, we performed the XPS analysis a few months after the growth. The analysis has shown that even for the thinnest part of the sample we could observe in the photoemission core-level spectra the contribution from the unaffected BT compound with the characteristic position of the Te and Bi lines (Fig.4.15). The remains of the Bi interlayers could also be detected for the films 4 and 6 nm thick. The oxides formed on the surface are mostly Bi_2O_3 and TeO_2 . For the thinnest films, a small contribution with higher binding energy than for TeO_2 was observed indicating to TeO_3 .

To estimate the thickness of the oxide layer, we used the formula that takes into account photoemission intensity damping [51]:

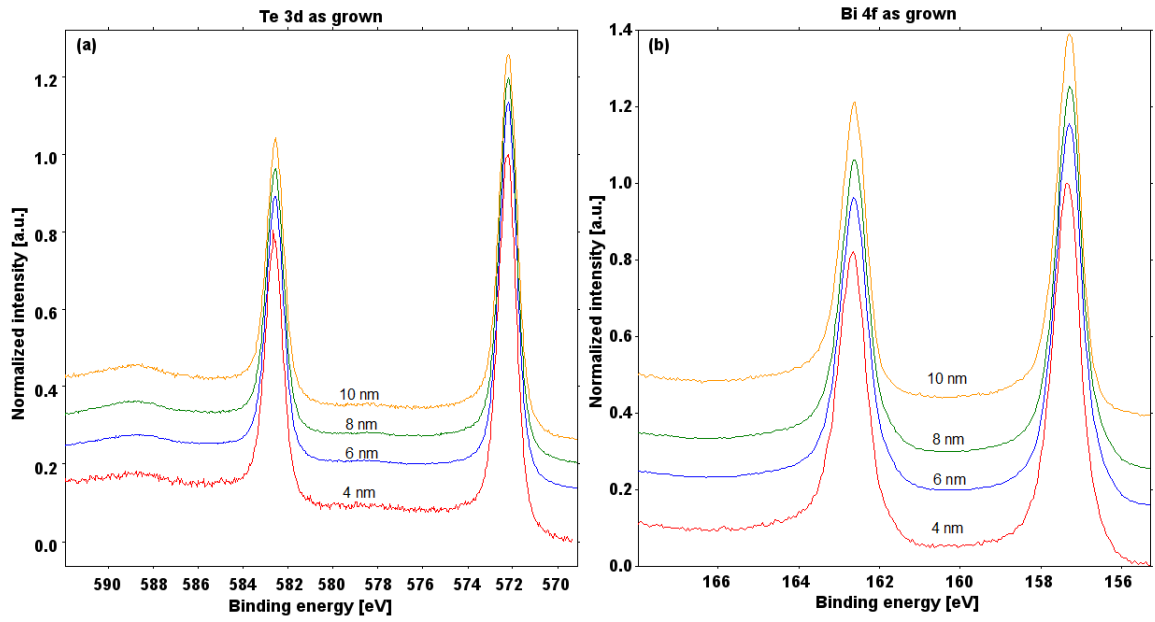


Figure 4.13: XPS $Te3d_{5/2}$ a and $Bi4f_{7/2}$ b doublets for the as-grown films.

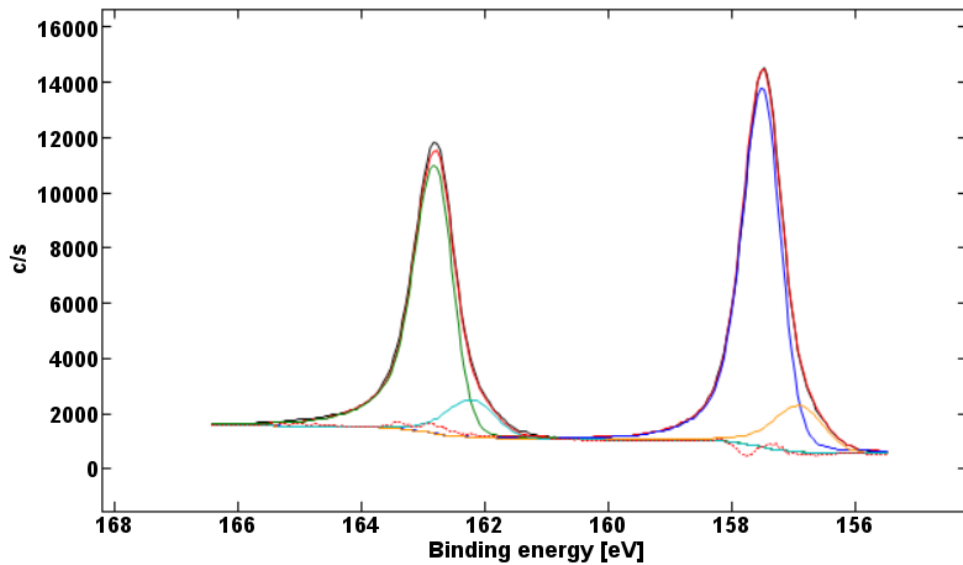


Figure 4.14: Fit of the $Bi4f_{7/2}$ doublet for the 6 nm thick film showing the contributions from the Bi_2Te_3 (high intensity doublet) and Bi (low intensity doublet).

$$\frac{I_C}{I_F} = \frac{I_{C_0} \left[1 - \exp\left(\frac{-d}{\lambda_C \cos\Theta}\right) \right]}{I_{F_0} \exp\left(\frac{-d}{\lambda_F \cos\Theta}\right)}$$

The intensity ratio from the oxide cap layer I_C and the main film I_F can be expressed with the use of the thickness of the cap layer d and inelastic mean free path within the basic film and the cap layer. The analysis angle was 45° .

The photoelectron mean free path λ can be estimated using the TPPM2M formula in the Quases program of S. Tougaard [52, 53, 54]. Performed calculations showed formation of about 1.75 nm of TeO_2 and 2.25 nm for Bi_2O_3 . We calculated the relative intensity of the photoemission components coming from oxides and BT. Size of the oxidized layer changes with the thickness, while for thin films of 4 and 6 nm the intensity ratio of oxide to BT is between 3 and 6, for the thicker films it is around 1.8.

When assuming a uniform cap layer of mixed Bi and Te oxides, one can calculate the thickness of the oxide film. Mean free path of about 2 nm was taken to the formula:

$$d = \lambda \cos\Theta \ln\left(\frac{I_C}{I_F} + 1\right)$$

where we applied assumption $I_{C_0}/I_{F_0} = 1$. The calculated thickness of the oxide layer varies from about 2.2 nm for thin films to about 1.4 nm for the films with thickness 8 and 10 nm.

Atomic concentration for the oxidized films				
Thickness	Tellurium	Bismuth	C	O
2 nm	8.3	9.3	45.0	37.4
4 nm	10.5	11.0	41.1	37.4
6 nm	12.2	13.0	40.9	33.9
8 nm	9.5	10.2	47.7	32.8

Surprisingly the AFM studies of the oxidized sample showed higher roughness for the thicker films. It may be related to the Stransky-Krastanov way of BT growth leading to the increased

differences between the height of the column. The quality of the surface seems to be better for those films, which leads to a lower thickness of the cap layer formed by oxides. The thickness of the oxides is between 1.4 and 2.5 nm, which protects the film from further oxidation. It does not influence or hardly influences the optical response of the main film composed of Bi_2Te_3 with a possible interlayer of Bi.

Table 3. AFM roughness measurements on step sample after oxidation

Thickness	Roughness
8 nm	2.25 nm
6 nm	0.57 nm
4 nm	0.31 nm
2 nm	0.68 nm

The obtained thickness of the oxides' film on the BT films means that the effective thickness of the compound may be lower than that from the as-grown films by about 2 nm, which was taken into account in all presented figures.

Samples group C

In order to better understand the chemical and physical processes near the interface between the iron and Bi_2Te_3 layer, we made precise measurements of the state of the sample after the exposure to the air. This process, just like in the case of samples from group B, played an especially important role in the proper interpretation of the results received from femtosecond laser spectroscopy.

During the measurements, we obtained the photoelectron spectra of $Te3d_{5/2}$ and $Bi4f_{7/2}$ core levels that were fitted by Gaussian-Lorentz or asymmetrical lines Fig.4.16. From the fitting of $Te3d_{5/2}$ core level line we can distinguish, aside of ordinary for this type of material oxidation states, of tellurium TeO_2 at 576.0eV and corresponding to the Bi_2Te_3 572.2eV line, additional state at 572.6eV that suggests the presence of FeTe in the form of the thin film. In

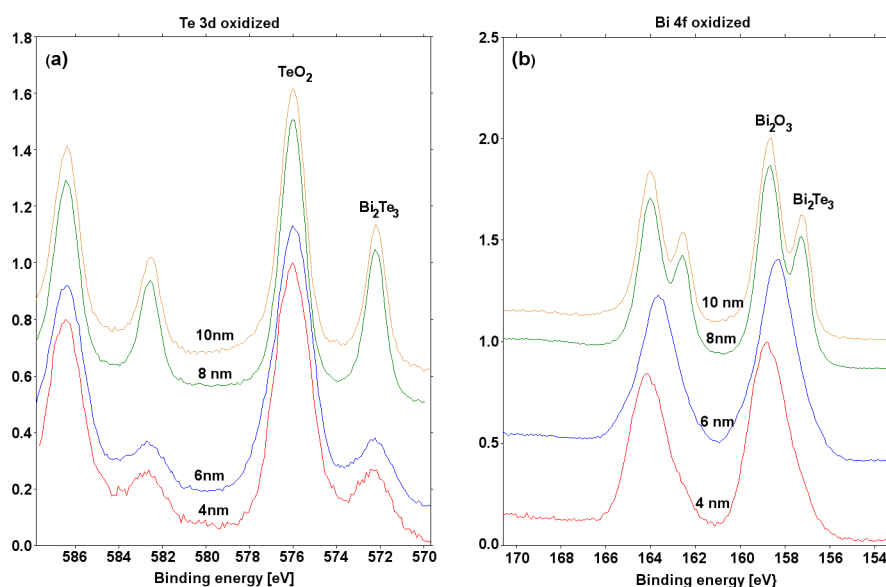


Figure 4.15: XPS doublets of $Te3d_{5/2}$ (a) and $Bi4f_{7/2}$ (b) after oxidation of the film.

the case of bismuth, we can observe the presence of only two main peaks coming from the formation of Bi_2O_3 at 158.9eV and line coming from Bi_2Te_3 at 157.45eV.

Additionally, we performed a thorough investigation of the state of $Fe2p_3$ core level line Fig.4.17; it was possible to fit the multiplet of iron 2p3 successfully. In the presented figure, we can see the central peak (709eV) and three others coming from the splitting. The additional peak at 713.5eV comes from the surface. Since the 1st and second peak is of the same height and, on the picture beneath, we can see the mainline at 710eV and a satellite with a shift of about 9eV. The iron is in a state of Fe^{3+} , and because of the shape of the multiplet, we can say that the formed oxide with a significant probability is $\gamma-Fe_2O_3$ (Maghemite) form of iron oxide or the hydrogenated form of the compound [55]. Further analysis of the spectra also revealed as well the existence of additional states in the valence band Fig.4.18 between the 2-8eV originating from the formation of the oxide layer, and additional states visible close to 1eV that corresponds to Bi_2Te_3 compound.

After the initial test of the states of the compounds directly on the surface of the sample,

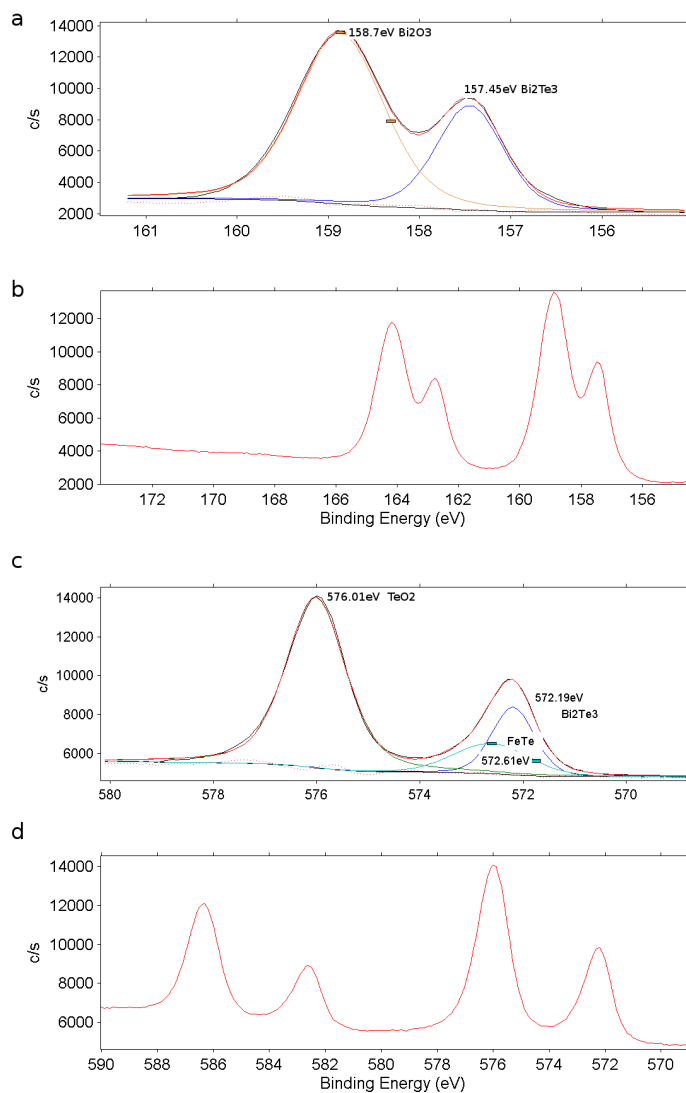


Figure 4.16: a - XPS spectra are fitting of $Bi4f_{7/2}$ core level and b - view over $Bi4f_{7/2}$ doublet lines. We can see two chemical states of Bi, one belonging to the oxide and second one to Bi_2Te_3 compound. c - XPS spectra fitting of $Te3d_{5/2}$ core level and d - view over $Te3d_{5/2}$ doublet lines. We can see that the tellurium has three chemical states: two main ones belong to oxide and Bi_2Te_3 , the third one probably belongs to pure Te in metallic state or FeTe compound.

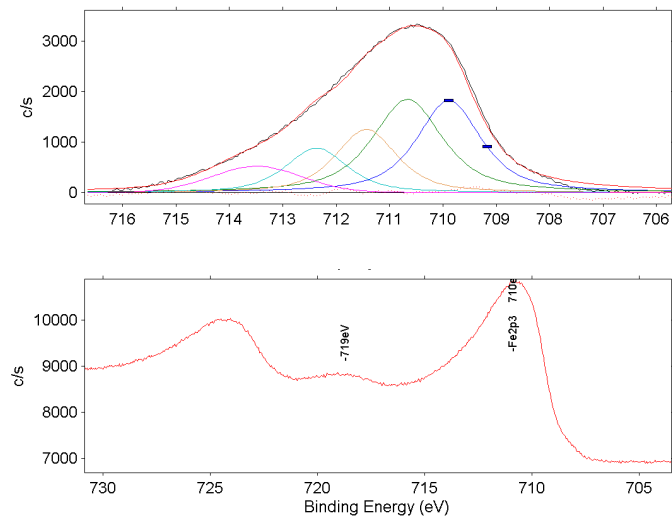


Figure 4.17: XPS spectra of $Fe2p_{3/2}$ core level.

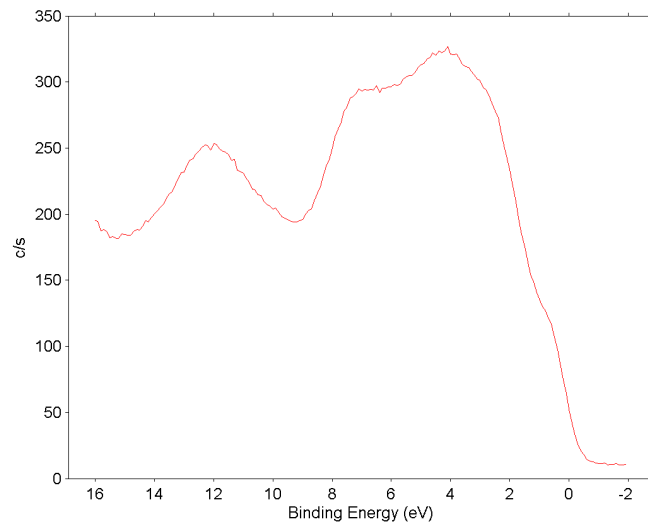


Figure 4.18: XPS spectra of valence band after the oxidation.

the measured film was slowly removed with a collimated beam of argon (Ar^+) ions to perform depth profiling of the sample. The x-rays beam was arriving at the sample at 45° (Fig.4.19). The rate of the incoming ion beam was set to remove the layer with a speed of about 1nm per 30min with the energy of 0.7keV , allowing us to receive a profile of the sample with a spectrum around every 2nm. It corresponds to $\sim 2QL$ change of thickness per spectrum. On presented in Fig.4.19.b depth profile, we can observe the change of chemical state of Tellurium. We can see that, after the removal of the first 4-6nm, Te is only in a compound of Bi_2Te_3 (Fig.4.19.b yellow line). Data presented in Fig.4.20. shows an evolution of the valence band structure shows that we are detecting the states coming from the Bi_2Te_3 already from the surface and starting from 2 lines, they are dominating contribution. Analysis of the iron line Fig.4.20.b revealed traces of iron in deep parts of the sample, up to the last 2-4nm of the layer. Presence of iron at such depth can be explained by taking into account a few factors:

- the layer growth has the dynamics of Stranski-Krastanov, where we have a formation of uniform plains upon which there is a growth of islands, such geometry allows diffusion of iron in between the islands and differences in the thickness of capping layer;
- local defects in a layer of Bi_2Te_3 and mica can act like channels through which iron can diffuse into the bottom layers;
- sputtering ions of argon can cause pushing in the iron more in-depth into the structure causing the observed effect.

We can observe as well slight shift in the energy of the iron into the region of lower energy; this effect might be explained both by the destruction of bonds in oxide, as well by the different structure of iron deeper inside the layer. Based on previous observations [34] it is possible that iron forms the FeTe structure within the sample. Unfortunately, because of the similar binding energy of Te in FeTe and Bi_2Te_3 , it is impossible to use it for confirmation.

Performed depth profile on the valence band revealed that the electron structure typical for the Bi_2Te_3 is visible even through the oxide layer Fig.4.20.a. The oxidized states are a source of large contribution to the density of states between 2-8eV and vanish rapidly after removal

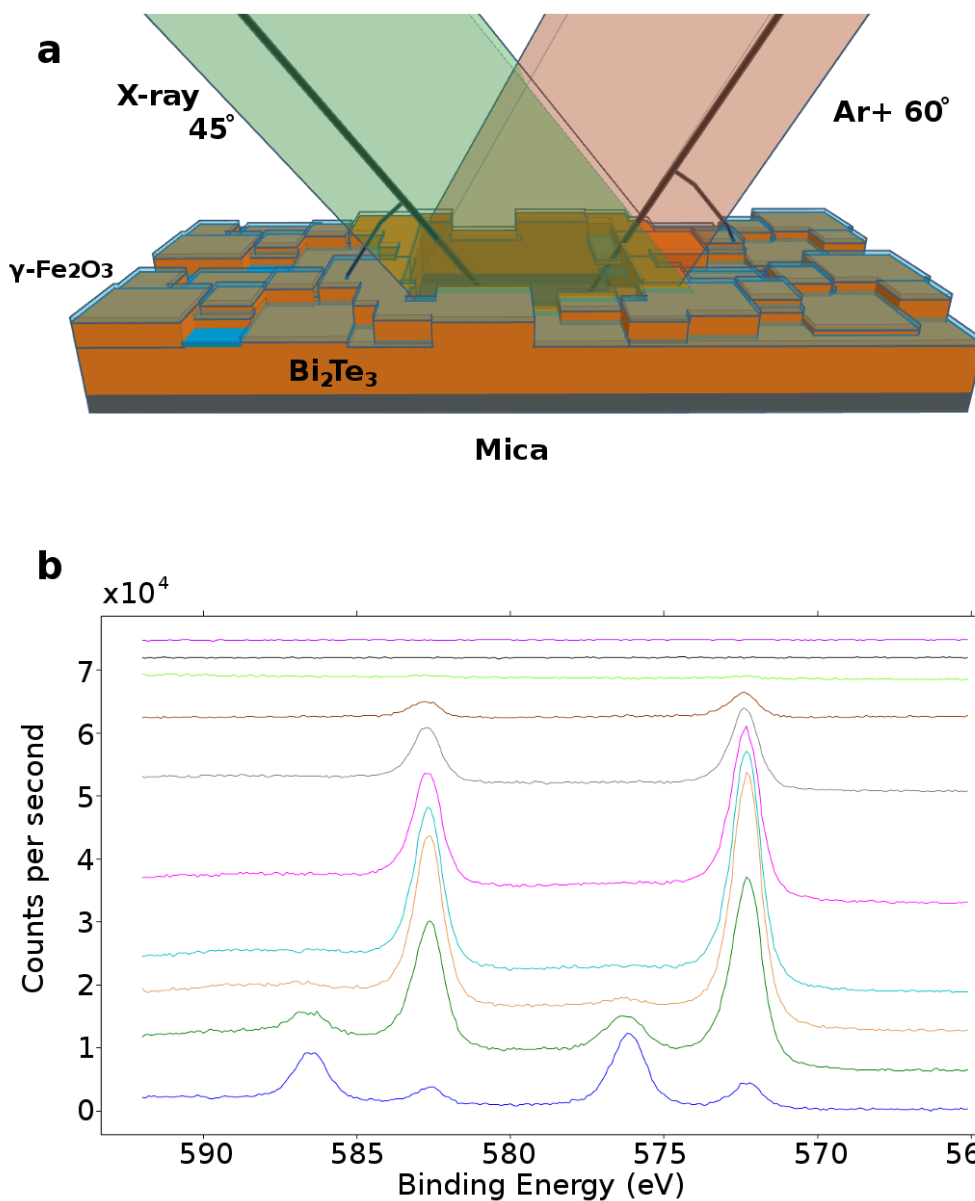


Figure 4.19: a - Artistic visualization of the surface of sample C2. Due to Stranski-Krastanov's type of growth, the sample at the start of deposition develops well-formed layers up to 10-12nm; after that, the material started to form an island-like structure that retained proper order and symmetry to the layers underneath. Highlighted with a green plane indicates the direction of the X-ray analysis beam, where the beam of ions used to remove layers was marked with red. b - Profile of sample C2 on line $Te3d_{5/2}$, the blue bottom line corresponds to the surface of the sample; the following lines were made during the removal of the next 2nm (2 QL) from the sample.

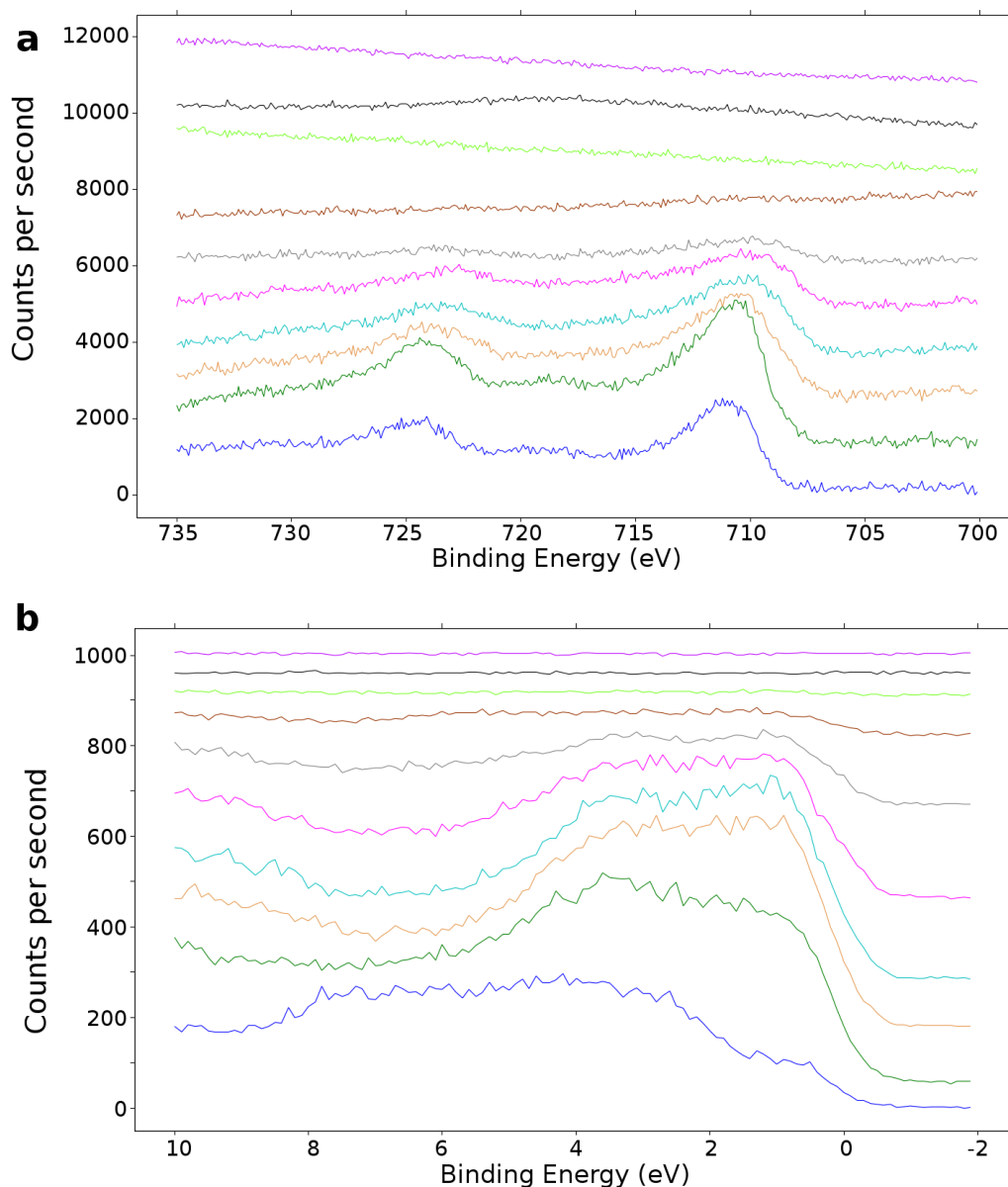


Figure 4.20: a - Profile of sample C2 of line Fe2p, the red bottom line corresponds to the surface of the sample following lines which were made during the removal of the next 2nm (2 QL) from the sample. b - profile of valance band, the red bottom line corresponds to the surface of the sample following lines which were made during the removal of the next 2nm (2 QL) from the sample.

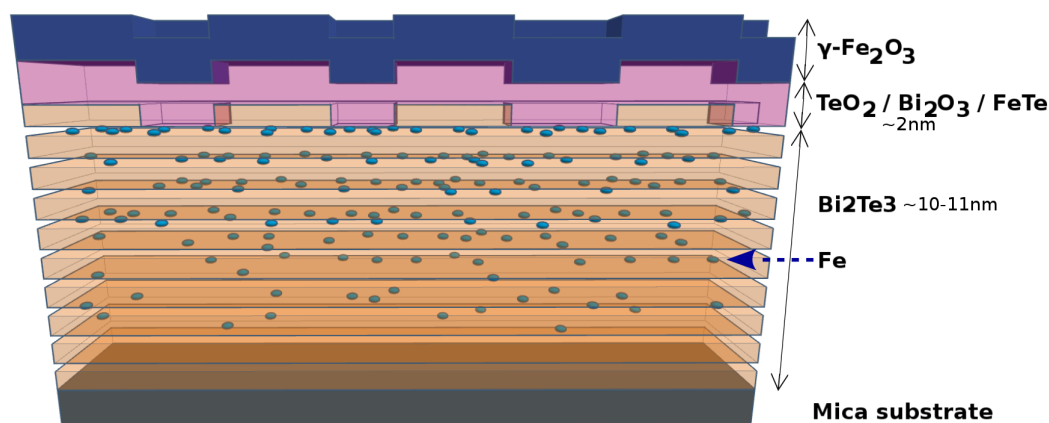


Figure 4.21: Artistic sketch of sample C2 cross-section based on data received from the depth profile.

of the first 4nm. Starting from line (13-12nm) the valence bands are exactly the same as in pristine freshly deposited Bi_2Te_3 [29, 30, 12, 34]. Taking into account the data from the depth profile, we managed to create a model of the layer with deposited iron, presented in Fig.4.21. On the presented figure we marked with blue spot the detected states of iron, which should not disturb the structure of Bi_2Te_3 and tend to accumulate in the Van der Waals layers between the QL's. Because of the uncertainty of the state of the iron (oxide or FeTe), it was marked as Fe.

4.3 Summary

Conducted experiments on samples from the group A revealed differences in crystal structure between sample grown on Muscovite Mica A1 and Silicon (001) A2 and A3. The diffraction image of sample A1 has shown a distinct presence of tiny terraces that possess two characteristics to the hexagonal cell patterns. The correct structure and stoichiometry of this film were confirmed as well by the LEED image and XPS spectra (Bi/Te - 46/54). In the case of samples A2 and A3, the RHEED image revealed the formation of a polycrystalline structure that might be caused by a mismatch between Bi_2Te_3 and silicon (001). Performed XPS also

revealed as well that both A2 sample and A3 are rich in Te (A2: 35/65; A3: 33/67) such composition is known to cause the formation of the interlayers of Te in between the Van der Waals layers of Bi_2Te_3 [50].

Investigation of the samples from group B revealed that the deposition technique, similar to the one used in the creation of the sample A1 gives stable and repeatable high-quality films of Bi_2Te_3 . Due to the unique opportunity given by planned variation in thickness, we were able to reveal that layers of Bi_2Te_3 tend to grow with Stransky-Krastanov dynamics. Likewise, to sample A1, films from group B shown the stoichiometry rich in bismuth, which should, as a result, give a stable superstructure Bi-BT within the QL's. Performed after the oxidation XPS measurements revealed the existence of passivated layer ($\sim 2nm$) of Te and Bi oxides, that is stable in time and acts as a protective layer from further degradation of deposited layers.

Experiments performed on the last set of samples with deposited iron oxide allowed us to identify the state of iron (Fe^{3+}) and type of the formed oxide ($\gamma-Fe_2O_3$). Additionally, depth profiling of the layer C2 has shown the presence of iron within the structure of Bi_2Te_3 . The lack of change in energy of core levels both of Bi and Te, characteristic to formation of Bi_2Te_3 , lead us to conclude that the additional iron within the layer might be in oxidized form or compound with Te, but at the same time, it does not destroy properly formed QL's of Bi_2Te_3 . This data allowed us to create a possible model of the formed structure that we presented in Fig.4.21.

Chapter 5

Time-resolved spectroscopy techniques

In this chapter, we will focus on ultrafast time-resolved spectroscopy. We will show the current description of the mechanisms of the signal generation and the setup used to perform our experiments. We will also present the results obtained on thin films of Bi_2Te_3 that were described in previous chapters.

5.1 Introduction to pump-probe techniques

5.1.1 Experiment

All performed measurements were made on femtosecond laser setup at Le Mans University presented in Fig.5.1. Used geometry allowed us to perform standard pump-probe spectroscopy both in reflection as well as in transmission. As the laser source for the experiment, we used Ti:sapphire Chameleon laser operated with (f_L) 80 MHz repetition rate and (P_L) maximal power of 3,2 W with pulse duration τ_{pulse} below 200fs. That translate to the energy of a single pulse at:

$$E_{pulse} = \frac{P_L}{f_L} = \frac{3,2W}{80MHz} = 40nJ$$

Produced by the laser beam 830nm (1.495eV) is then split with a polarizing beam splitter into a pump and a probe beams. The probe beam is introduced in a synchronously pumped Chameleon OPO (principles of second harmonic generation and frequency mixing in Appendix), from Coherent company, that allows us to tune the wavelength in range of 600-550nm and finally permit to do two-color pump-probe experiments (pump and probe linearly and circularly polarized respectively) that allowed us to filter out the pump contribution on the photo-detector. During our experiments, we kept the probing line in the range of 590-570 nm (2.13 eV). For the chosen energies of pump and probe, it corresponded to absorption lengths of 8 nm and 10 nm (for optical constants see Appendix) [38]. The pump line was modulated with wave function by EOM device, which was adjusted in real-time by lock-in amplifier using a reference signal from photo-diode. Pump signal was also delayed in time to the probe signal by changing its path using a computer-controlled delay line (Fig.5.1.b). This part of the system is crucial for femtosecond spectroscopy. The delay line causes delay of the pump arrival in accordance to probe in order to detect the evolution of the system as a function of time. Delay line usually consists of a mechanized moving mirror; in our experiment, it is placed on the pump optical path. This element requires a high precision of movement in order to achieve a good resolution of acquired data. To put it in perspective, a movement of the mirror

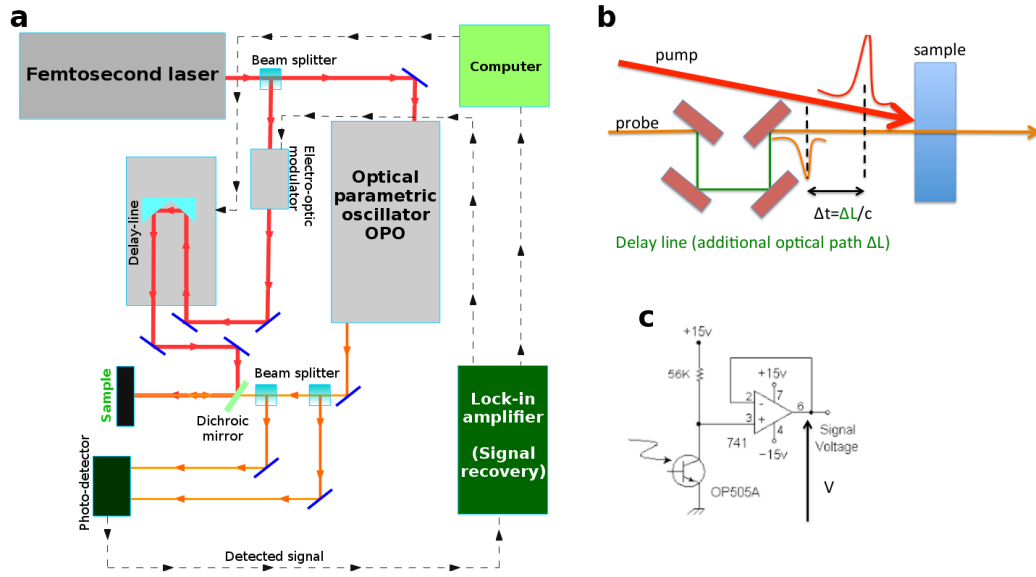


Figure 5.1: a - Schematic of two-color pump-probe experiment. b - Schematic of delay line. c - Schematic of photo detector.

by $\Delta L = 0.1\text{mm}$ results in the time delay between pump and probe at the scale of:

$$\Delta t = \frac{2\Delta L}{c} = \frac{10^{-4}\text{s}}{3 \cdot 10^8\text{m/s}} \approx 300\text{fs}$$

The pump and probe meet each other at the dichroic mirror, which reflects the pump and transmits the probe. This allows us to superimpose the pump and probe on the surface of the sample. In our experiment, we use pump power of around 10mW ($E_{pulse} = 0.125\text{nJ}$), that gives the rate of energy that the pump deposits on the surface of the sample at:

$$P_p = \frac{E_{pulse}}{\tau_{pulse}} = \frac{0.125\text{nJ}}{200\text{fs}} = 625\text{W}$$

The energy of the probe was kept at around 1mW that is ten times lower than the pump. Both beams were then focused with a microscope objective down to a spot of A area around $80\mu\text{m}^2$. That gives the total intensity of the pump equal to:

$$I_p = \frac{P_p}{A} \sim 8 \times 10^{12} \frac{\text{W}}{\text{m}^2}$$

and the fluence of the pump (that gives us information of how much energy single pulse has deposited over the area):

$$F_{pulse} = \frac{E_{pulse}}{A} = 1,6 \frac{J}{m^2} = 0,16 \frac{mJ}{cm^2}$$

The reflected (or transmitted) probe is then directed to photo detector (Fig.5.1.c), that transforms the intensity of the arriving pump to voltage, that can be then introduced into lock-in amplifier.

5.1.2 Theory

Methods of registration of fast processes have gone through an unusually rapid process of development, throughout the last 100 years. At the end of the 19th century, the shortest possible time resolution was around few ms (10^{-3}), and at the end of 20th century, it was pushed by a tremendous factor of 10^{14} , which opened a new doorway for the understanding of fundamental processes in physics and chemistry. Nowadays technology allows direct observation of quantum effects with time resolution as short down attoseconds (10^{-16} s), which is one of the most spectacular achievements in terms of technology and it was awarded in 2018 a Nobel Prize in Physics. This time resolution was achieved in 2006 as the shortest time-scale ever was observed (direct measurement of light waves - Fig.5.2). Unfortunately, systems that can achieve such time resolution are still presenting a challenge. On the other hand, the femtosecond (10^{-15} s) time resolution is relatively easy to achieve with commercially available sources.

Different rules than conventional macroscopic physics governs ultrafast processes. For example, during the first few femtoseconds after the excitation electrons move while cations may still be frozen. In such time scales, the classical statistical temperature cannot be defined, and such systems are deterministic mainly because the observation time is too short for the system to explore the entire phase space. New concepts have to be thought up in order to understand and interpret the femtosecond time scale. Ultrafast laser excitation may lead to non-trivial ef-

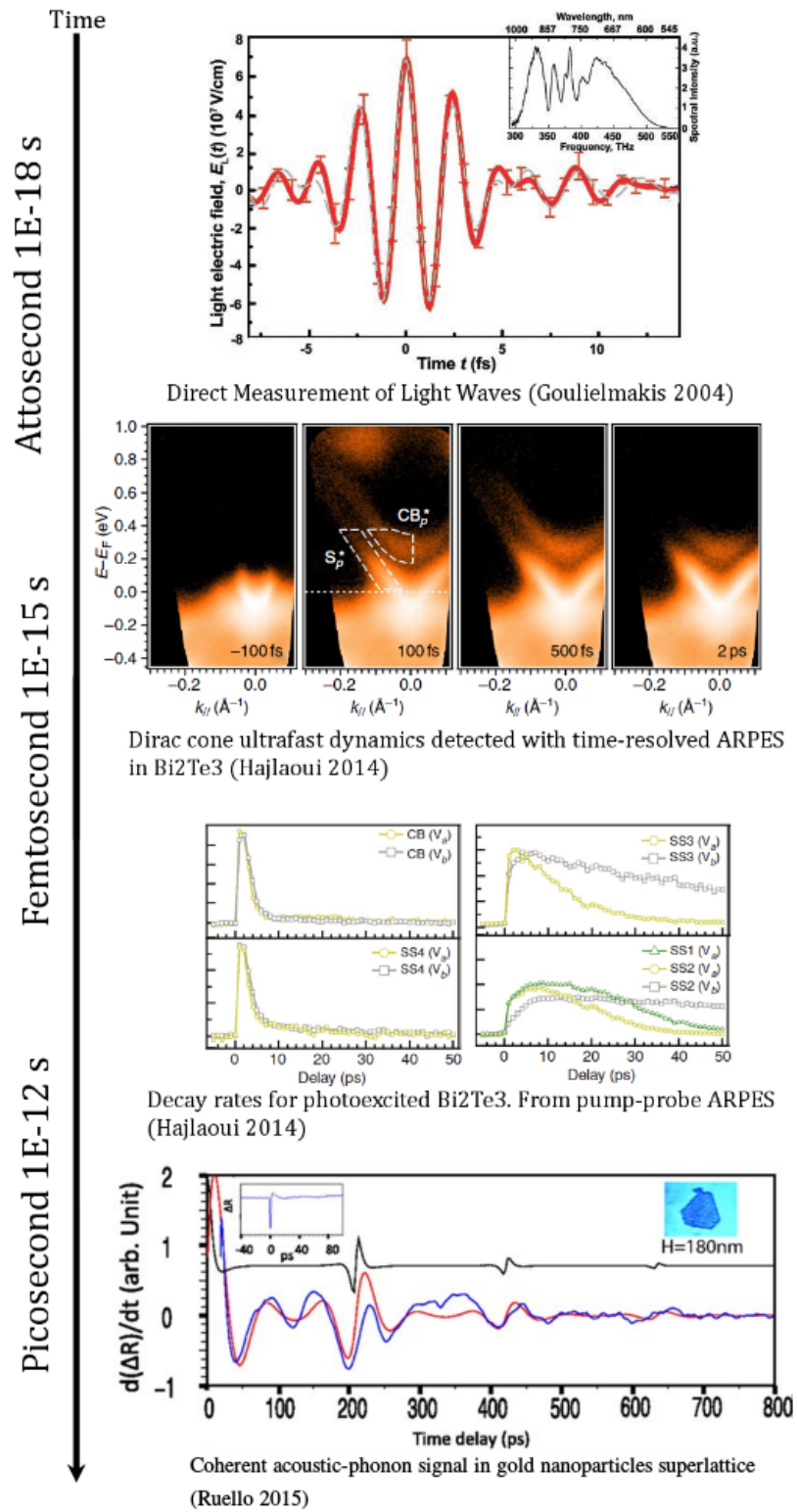


Figure 5.2: Time scale of our ability to register physical processes.

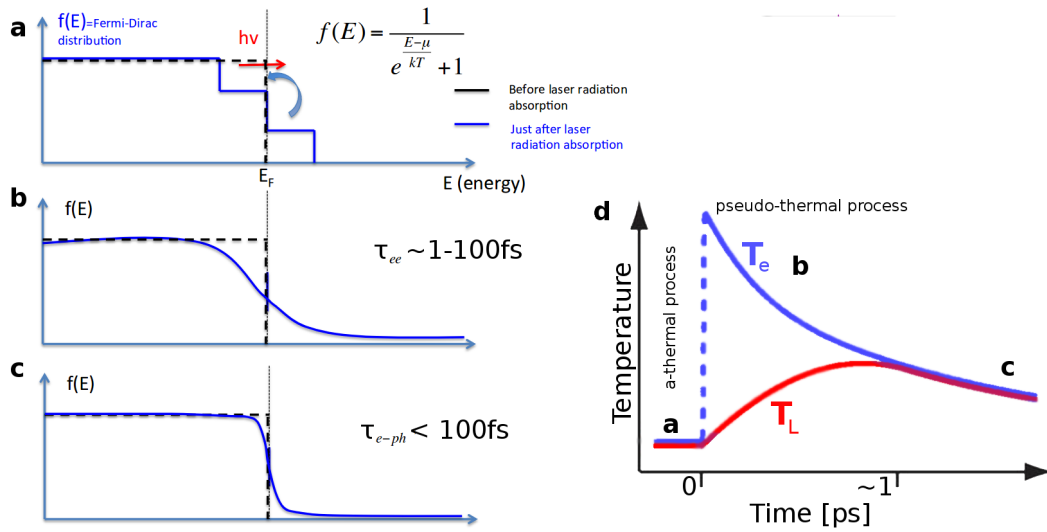


Figure 5.3: Time dependence of the Fermi distribution after an ultrafast laser excitation: a - photon energy is first absorbed by the electrons, b - thermalization of the electronic subsystem, c - thermalization of the electronic subsystem with the phonon (cations) subsystem. d - TTM two temperature model shows the time scale of the processes mentioned earlier.

fects, such as the relaxation channels used by the system to dissipate energy being dependent on the duration of the external trigger. The Time-resolved pump-probe experiment is based on the simple idea of time-lapse motion detection like in regular cameras.

Carrier dynamics:

When the photon packet arrives at the sample, it interacts with part of its volume, leading to a modification of internal energy. The electrons first absorb the photon energy, in the case of interaction with light in visible spectrum range (Fig.5.3), in general after which electrons start to thermalize rapidly τ_{ee} by electron-electron collisions (Fig.5.3.b) [56]:

$$\tau_{ee} = \tau_0 \left(\frac{E_F}{kT} \right)^2 = \tau_0 \left(\frac{E_F}{\Delta E} \right) \quad (5.1)$$

usually within $1 - 100fs$, after which the system start to dissipate energy through electron-phonon interaction (Fig.5.3.c) [57]:

$$\tau_{e-ph}(E) = \frac{C_e}{2g} \left(1 + \sqrt{1 + \frac{E}{E_0}} \right) \quad (5.2)$$

As a first approximation those times can be derived by taking into account the specific heat of electron C_e and lattice C_L in the two-temperature model (TTM) initially proposed by Kaganov, Tanatarov and Lifshitz [58] (Fig.5.3.d). After excitation with an ultrashort optical pulse the electrons and after the electron-electron thermalization, the electrons are described by a Fermi-Dirac distribution at temperature T_e (see Fig.5.3.b) and the lattice by a Bose-Einstein distribution at temperature T_L , the general equations for this model are as follow [59]:

$$\begin{cases} C_e(T_e) \frac{\partial T_e}{\partial t} = \kappa \Delta^2 T_e - g(T_e - T_L) + P_0(r, t) \\ C_L \frac{\partial T_L}{\partial t} = g(T_e - T_L) \end{cases} \quad (5.3)$$

where g is the coupling constant between electronic and phononic subsystem (deformation potential, Fröhlich, etc...), κ is the electron thermal conductivity, and $P_0(r, t)$ is optical source term that provides the energy to the electronic subsystem (Gaussian function). The energy transfer from the electrons towards the phonon subsystem is proportional to the difference of their corresponding effective temperatures. This model works quite well with metals where the relaxation of electrons occurs through the intraband relaxation mechanism [59], but in the case of semiconductors, we have to take into account not only the intraband process but also interband process, due to existence of bandgap Fig.5.4.b. The two-temperature model can be separately applied to be defined for electrons and holes in the intraband relaxation process, that takes place in the conduction (CB) and valence (VB) bands, respectively. This allows the determination of the energy exchange between electrons and holes with lattice during that intraband process. This works as far as the interband relation ($CB \rightarrow VB$) does not take place and usually, the intraband process is much faster than the interband relaxation which allows separating in time the description of each of these processes. For this purpose, we need to define in the TTM a corresponding heat capacity for both electron and holes. After the intraband

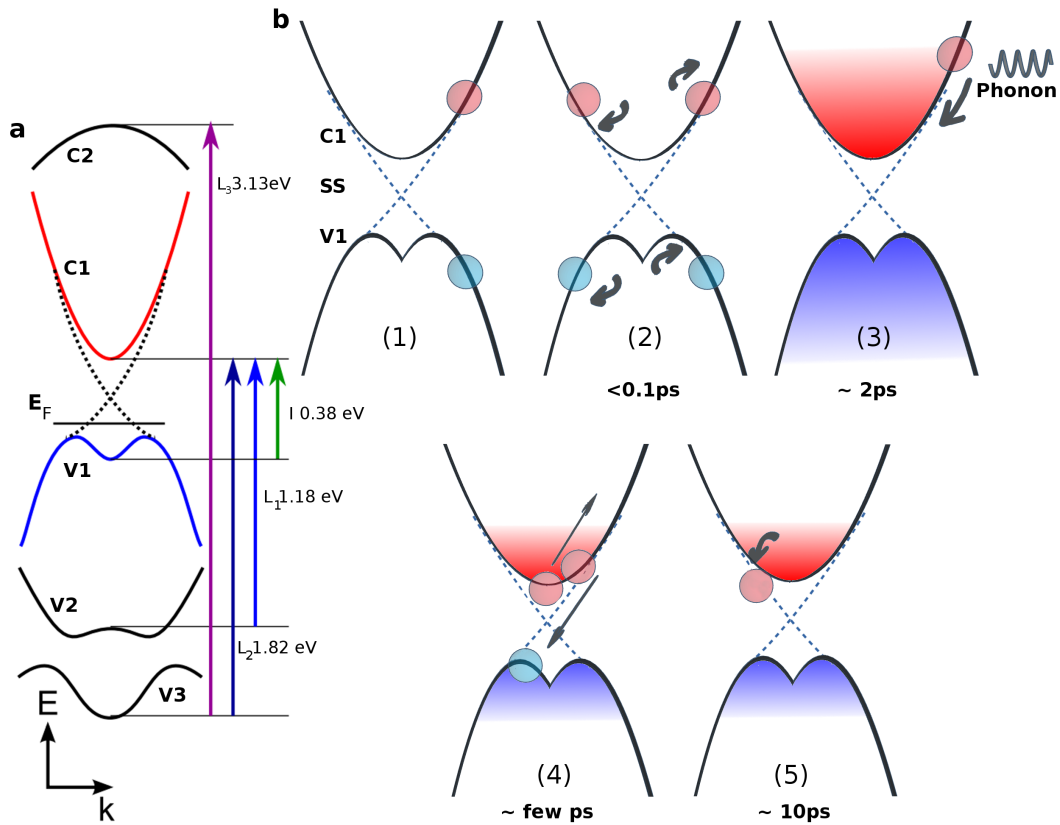


Figure 5.4: Schematic diagrams of electronic dispersions in $Bi_{1.5}Sb_{0.5}Te_{1.7}Se_{1.3}$. b - diagrams of relaxation processes of photo-excited carriers in the lowest conduction band (C1), the highest valence band (V1), and the surface states (SS) existing in 3D topological insulators: (1) photo-excitation of electron-hole pairs, (2) carrier thermalization, (3) carrier cooling due to phonon emission, (4) Auger recombination, and (5) intraband scattering from C1 and V1 to SS. From Y. Onishi et. al. Phys Rev B (2015).

process is achieved, we can say that carriers and phonon are thermalized ($T_e = T_L = T$)[59, 60]. At this stage, we can consider the electrons and holes are pretty well localized in energy at the bottom and top of the CB and VB (Fig.5.4.b). We describe then the dynamics of electrons (holes) with their volumic concentration. The electrons (holes) can then relax (interband process) either by non-radiative or radiative recombination process. For the first case, the energy that has been released to the lattice increases its temperature. For the second one, the energy is converted into radiation. The carrier dynamic can then be described according to the Boltzman equation[59]. The carrier dynamics equation will take the following form:

$$\frac{\partial N(t,x)}{\partial t} = D_{eh} \frac{\partial^2 N(t,x)}{\partial x^2} - \frac{N(t,x)}{\tau_R} + \frac{1-R}{h\nu_L} I_L f(t) e^{-\alpha x} \quad (5.4)$$

where D_{eh} is the carrier diffusion coefficient, R is the optical reflectivity of the material, τ_R is the rate of carriers recombination, $h\nu_L$ is the laser quantum energy, I_L is the laser intensity, $f(t)$ is the temporal envelope of the laser pulse (Gaussian) and α is the optical absorption. This out-of-equilibrium electron-hole distribution will immediately affect the optical properties of the material. The dielectric function will be perturbed, which leads to the following variation of the optical reflectivity coefficient with:

$$\frac{\Delta R}{R} = f(\epsilon_1, \epsilon_2) = \frac{\partial \ln R}{\partial \epsilon_1} \Delta \epsilon_1 + \frac{\partial \ln R}{\partial \epsilon_2} \Delta \epsilon_2 \quad (5.5)$$

where the ϵ_1 and ϵ_2 are the real and imaginary part of the dielectric constant, which are dependant on a number of photo-excited carriers. During the excitation with the pump light pulse, we transfer an electron from the VB into the CB (Fig.5.4.a); as a result, we change the electron density function leading to the modification of light absorption and transmission through the change of $\Delta \epsilon_1$ and $\Delta \epsilon_2$. This effect is then used in the pump-probe experiment in the following way: after the pump excitation, the irradiated region is probed with a second laser pulse (so-called probe) which fluence is smaller than the pump. Because the fluence of the probe is much lower than the pump, the induced change in dielectric function by the probe is small enough to be in the linear regime of the detection process. The probe that is being transmitted or reflected from the sample carriers now information about the change generated in dielectric

function ($\Delta\epsilon_1$ and $\Delta\epsilon_2$) initiated by the pump pulse

During the first femtoseconds we can typically observe (Fig.5.5) a sharp change in optical properties, which is typically referred to as an electronic peak. In the case of absorbing solid, as it is in case of Bi_2Te_3 , this phenomenon is attributed directly to the excitation of hot carriers, which relaxation process plays an important role in launching the coherent vibrations, that will be discussed later on. As earlier proposed in the literature [61], the transient electronic contribution to the change in signal $\Delta R/R_{elec.}$ of the optical reflectivity can be numerically adjusted with a function that takes into account the integrated response of the solid during the pump-probe cross-correlation as well as the decaying signal. For the latter one, we need to use two specific times, τ_1 for the fast dynamic (ps) and τ_2 for the slower one (thermal effect or slow electronic relaxation).

$$\frac{\Delta R(t)}{R_{elec.}} = \left[1 + erf \left(\frac{t}{\sigma} - \frac{\sigma[\tau_1 + \tau_2]}{\tau_1 \tau_2} \right) \right] \left[A_1 exp \left(-\frac{t}{\tau_1} \right) + A_2 exp \left(-\frac{t}{\tau_2} \right) \right] \quad (5.6)$$

with σ the resolution of measurement that is dependant on the optical path and the laser pulse duration, τ_1 the hot carrier relaxation, τ_2 the thermal relaxation, A_1 the hot carriers contribution and A_2 the thermal contribution. Once the electronic contribution is adjusted, it is possible to extract the phonon contribution $\Delta R/R)_{phonon}$ arising from the optical and acoustic phonons (green curve in Fig.5.5).

Phonon generation and detection:

The relaxation of hot carriers leads to the generation of stress at the unit cell level (generation of optical phonon) or macroscopic scale (acoustic phonon) within the structure. This photo-induced stress is the driving mechanism of coherent vibrations. For the case of coherent acoustic phonons, the lattice motion can usually be described with the general equation of motion in accordance to classical Newton law [59, 60]:

$$\frac{\partial^2 u(x,t)}{\partial t^2} - v^2 \frac{\partial^2 u(x,t)}{\partial x^2} = \frac{1}{\rho} \frac{\partial \sigma(x,t)}{\partial x} \quad (5.7)$$

where $u(x,t)$ is a function describing the atom motion, v is a speed of propagation of the acoustic pulse, ρ is the density of the medium and $\sigma(x,t)$ is time and space function of photo-induced

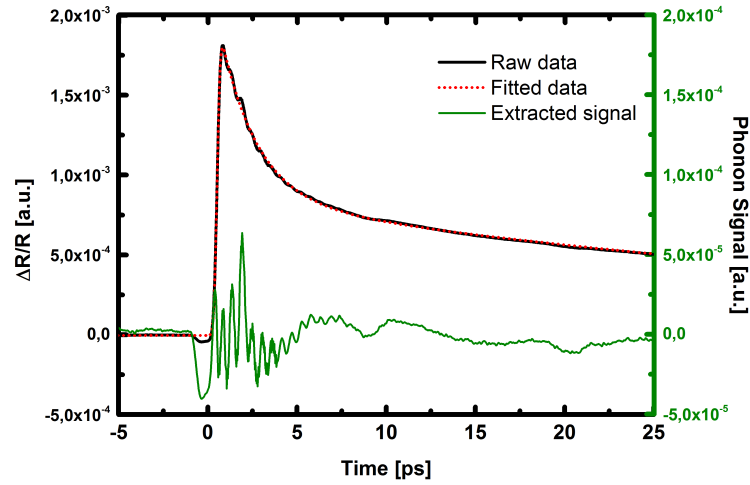


Figure 5.5: The measured signal was fitted with function 5.6 and remaining after subtraction residua are consisting mainly of the phonon signal from the investigated region.

stress. This photo-induced stress spatial distribution is governed by the optical skin depth at the pump light wavelength, but can also be affected by hot carriers diffusion, for example, [59, 60, 63]. In this approximation, we are only discussing one-dimensional geometry. It is possible to take such an assumption when the irradiated area is much larger than the distance of propagation of the coherent acoustic pulse. The photo-induced stress has few dominating processes at its origin, that is deformation potential and thermoelasticity [59, 60, 63].

Deformation potential mechanism generates the stress within the material by modification of the electron energy distribution. This change in electronic distribution, in this case, due to optical excitation, leads to the change in interactions between electrons-cations, cations-cations, and electrons-electrons. As a result, it generates the evolution of the interatomic forces, since they are dependent on this distribution (Fig.5.6). A change in the interatomic forces leads to the change of position of cations from their equilibrium in the lattice and hence to the crystal deformation [59, 60, 63]. We can say that the out-of-equilibrium carriers induce the deformation of the crystal lattice, and consequently, coherent vibrations are emitted. The

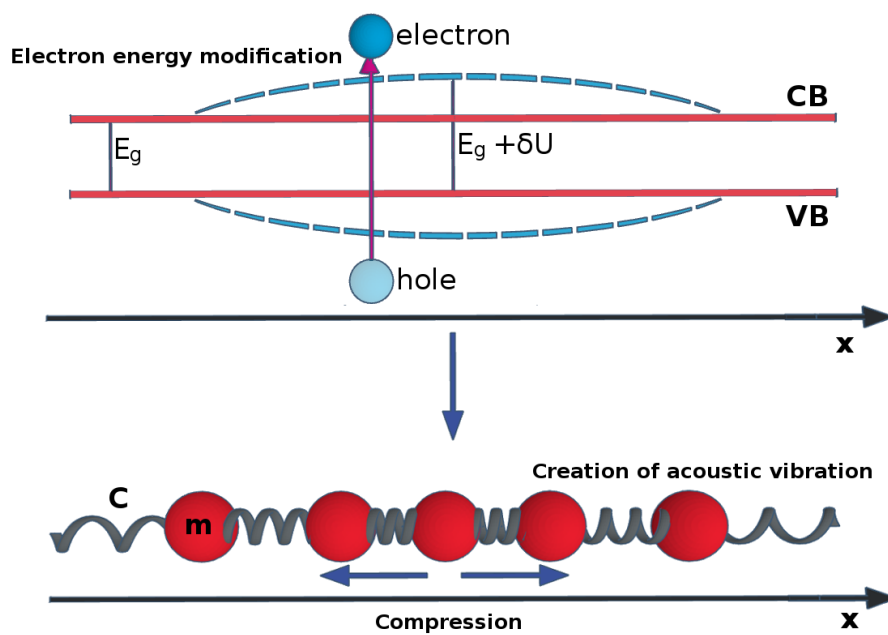


Figure 5.6: Deformation potential in band structure picture: excitation of an electron-hole pair disturbs the electronic distribution and modifies the interatomic interaction leading to a change of atomic positions and consequently to the generation of a strain field.

relation between the local strain in the lattice ($\frac{\delta V}{V}$) and the change of the electron energy (δU) is given by equation [60]:

$$\frac{\delta V}{V} = \frac{\delta U}{d_{eh}} \quad (5.8)$$

where d_{eh} is deformation potential parameter. We can see that the change in electron energy levels is directly connected to the generation of strain in the structure. It is possible to understand the deformation potential through the molecular picture, as shown in Fig.5.7. When the light pulse induces the carrier excitation, the electron (or holes) takes unoccupied electronic levels; as a result, it leads to the creation or destruction of atomic bonds. Depending on the type of the bond (bonding or anti-bonding), this process leads to compression or expansion of the bond between the atoms [60]. The photo-induced stress can be correctly described by

taking into account the existence of electronic band structure in the solid. During the photo-induced carrier excitation, we are modifying the electron population at different levels E_k ; we can then show that the measured photo-induced stress[63]:

$$\sigma_{DP} = - \sum_k \delta n_e(k) E_k \gamma_k = \sum_k \delta n_e(k) \frac{\partial E_k}{\partial \eta} \quad (5.9)$$

where k is the wavenumber of electron, $\delta n_e(k)$ denotes the change in concentration at level k , γ_k is the electronic *Grüneisen* coefficient and $\frac{\partial E_k}{\partial \eta}$ is the induced change in electronic levels because of the induced stress (i.e the deformation potential parameter).

Due to ultrafast relaxation of the photo-excited carriers in metals, the deformation potential can launch the coherent acoustic vibrations only during first picoseconds before the relaxation of the carriers at the Fermi level. This means that the coherent acoustic pulse has a typical duration of 1ps (the order of the electron-phonon thermalization time). As a consequence, such THz pulse is not easy to be detected [59, 60]. After the thermalization process is finished, the lattice has been heated up, and the thermoelastic process becomes the driving mechanism (discussed a bit later on). The role of the deformation potential can be especially important in the system in which electrons cannot easily escape and are confined within the excited region (like in the case of nanoparticles, see [62]), in such case the electron pressure can remain the largest contribution to the induced stress. In case of semiconductors with channels for fast intraband relaxation (hot electrons are relaxing towards the bottom of the conduction band), we can simplify the deformation potential:

$$\sigma_{DP} = \sum_k \delta n_e(k) \frac{\partial E_k}{\partial \eta} = N \frac{\partial E_k}{\partial \eta} = N \frac{\partial E_g}{\partial \eta} = -NB \frac{\partial E_g}{\partial P} = -d_{e-op} N \quad (5.10)$$

where B is the bulk modulus of the crystal, N is the concentration of photo-excited carriers, E_g is the bandgap, and d_{e-op} is deformation potential parameter at the bandgap energy. This model works only for frequencies that are smaller than the inverse of the intraband relaxation process time. Deformation potential, depending on the nature of electronic levels to which the carriers were excited, can take either compressive or tensile nature [59, 60, 63]. The type of

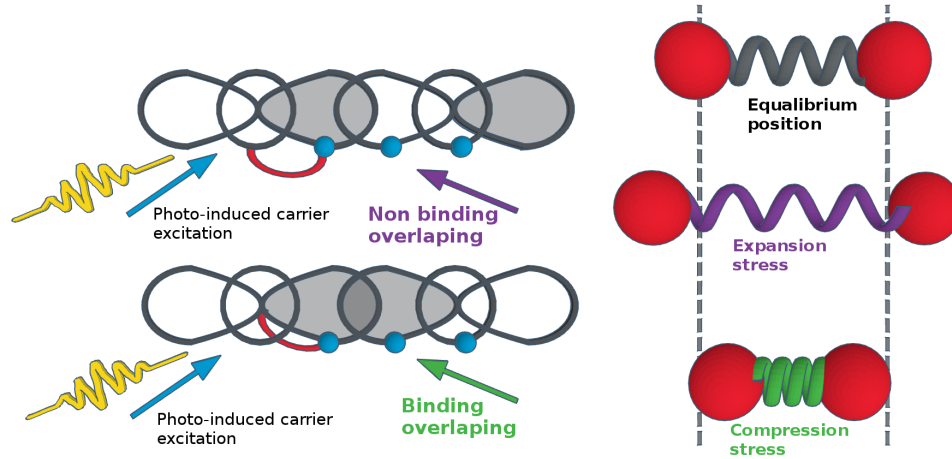


Figure 5.7: Deformation potential in molecular picture: excitation of electron from one orbital to another modifies the electronic distribution causing appearance of bonding (compression) or antibonding (expansion) interactions between atoms.

change is determined by the sign of the deformation potential parameter and can be directly obtained from the pressure dependence of the bandgap. In case of an increase with the pressure $\frac{\partial E_g}{\partial P} > 0$ the d_{e-op} is positive, and the structure expands under the electron excitation. The opposite reaction leads to structure contraction. This situation is a direct result of the nature of molecular bonds (binding, non-binding or anti-binding) Fig.5.7.

The most known mechanism of the generation of coherent acoustic phonons is the thermoelasticity. The basis of this phenomenon is the conversion of deposited laser pulse energy into lattice energy (thermal energy) by different channels of relaxation. The quick rise in thermal energy leads to an expansion of the irradiated volume through the lattice anharmonicity. This expansion, in case of ultrashort laser pulses used in our experiment, generates ultrafast expansion in a time corresponding to the electron-phonon relaxation time. If we neglect the process of electron diffusion within the structure, it is possible to describe the generated stress analytically. The function of the photo-induced stress will be dependant on the temperature rise at a depth of pump penetration ξ and on the total pulse energy Q that is deposited over the

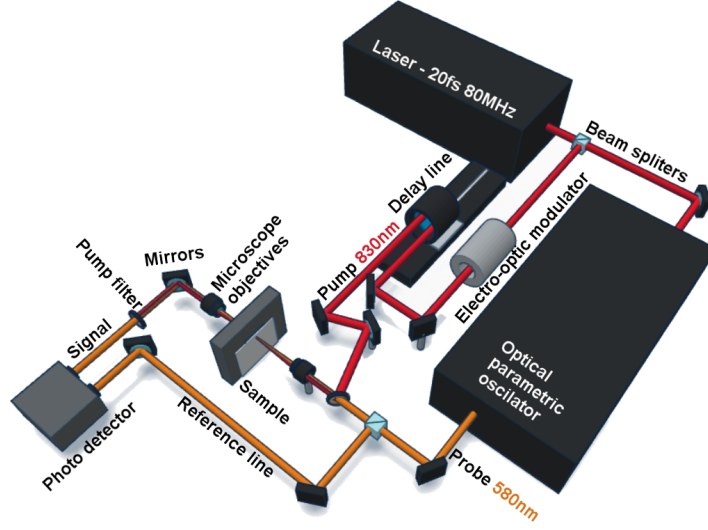


Figure 5.8: Scheme of two color pump (830nm) and probe (580nm) setup, used for the experiments.

area A of the structure. The induced change in temperature will take the following form [63]:

$$\Delta T = \frac{(1-R)Q}{CA\xi} e^{-\frac{x}{\xi}} \quad (5.11)$$

where R is the optical reflectivity of the material, C is the specific heat per unit volume, x - is the distance from the surface and ξ is the typical absorption length of the pump wavelength (in case of Bi_2Te_3 for pulse 830nm it is $\xi \sim 10nm$ [38], see Appendix 7.2). Having the expression for the temperature profile, we can now write down the time-dependent photo-induced stress profile $\sigma(x,t)$ equal to:

$$\sigma(x,t) = -3B\beta\Delta T(x,t) \quad (5.12)$$

where B is the bulk modulus and β is linear thermal expansion coefficient.

Regarding the generation of optical phonon [64, 65, 66], we can distinguish two main models used to describe this effect. Taking into account that light can couple directly with optical phonon branches, the natural first process that was discussed is the stimulated Raman process [64, 65]. The Raman active mode whose normal coordinate is given by Q is described

following:

$$\frac{d^2 Q}{dt^2} + \Omega^2 Q = \left(\frac{\partial \chi}{\partial Q} \right) |E_0(r, t)|^2 = \sum_{uv} \frac{\frac{\partial \chi_{uv}}{\partial Q} E_u E_v}{2} \quad (5.13)$$

where E_u denotes a component of the optical pump field, $\frac{\partial \chi_{uv}}{\partial Q}$ is nonlinear Raman tensor and χ_{uv} in linear electronic susceptibility. The second process is the displacive excitation of coherent phonons (DECP, deformation potential)[66]; it can describe the generation of optical phonons which conserves the crystal symmetry denoted as A_1 modes. In this model, we assume that, by a high-intensity short laser pulse, we can disturb the electronic distribution in the material. In this particular case, we can say that this process is similar to the approach based on the potential deformation coupling discussed previously for coherent acoustic phonon. By this excitation, the nuclear coordinates within a unit cell will change along A_1 symmetry. In this model, the photo-generated interband transitions excite the population of carriers N , that is linearly dependant on the equilibrium A_1 coordinate Q_0 [66]:

$$Q_0 = \kappa N \quad (5.14)$$

and it gives us the equation of optical mode motion:

$$\frac{\partial^2 Q}{\partial t^2} = -\omega^2 [Q - Q_0] - 2\gamma \frac{\partial Q}{\partial t} \quad (5.15)$$

where ω_0 is the angular frequency of A_1 optical mode, γ is the damping constant.

In the previous paragraphs, we have briefly introduced the generation mechanisms of coherent acoustic and optical phonons. These phonons can be detected in a pump-probe experiment since they both modulate the interatomic distances (at the level of a unit cell for optical phonon or a more macroscopic level for acoustic phonon), which consequently modulates the dielectric constant ($\Delta\epsilon_1$, $\Delta\epsilon_2$, see Equation 5.6). Depending on the detection scheme, reflected or transmitted probe light is collected by a photo-diode which signal provides, only indirectly, some information about the photo-induced dynamics. We say indirectly in the sense that we do not have access directly to the photo-induced strain but only through the modification of

the optical properties. For the detection of coherent acoustic phonons, we have to take into account the interferometric contribution due to the free surface motion $u(0)$ and the photo-elastic coupling leading to probe light scattering. For example, in the case of a semi-infinite system, it has been shown that the change of the complex transient optical reflectivity generated by acoustic vibration $\left(\frac{\Delta r}{r}\right)_{ac}$ is given by:

$$\left(\frac{\Delta r}{r}\right)_{ac} = -2ik_0u(0) + \frac{4ik_0n}{1-n^2} \frac{\partial n}{\partial \eta} \int_0^\infty \eta(x,t) e^{2ink_0x} dx \quad (5.16)$$

where k_0 is the probe lightwave vector in vacuum, $u(0)$ - is the free surface displacement in the sample, η - the strain, n - complex refractive index and $\frac{\partial n}{\partial \eta}$ - is the photo-elastic coefficient.

For acoustic phonon the $\frac{\Delta r}{r}$ can be sinusoidal (Brillouin, transparent materials) or have the form of a pulse (opaque materials)[59, 60]. For optical phonon, because the group velocity is nearly zero (no propagation), the transient optical properties take into account only the time dependence, even of course if the total detected signal integrates the response over a volume defined by the skin depth at the given probe wavelength. For optical phonon detection process of $\left(\frac{\Delta r}{r}\right)_{op}$ is proportional to:

$$\left(\frac{\Delta r}{r}\right)_{op} = A \frac{\partial \chi}{\partial Q} a_0 \sin(\omega_0 t + \varphi) \quad (5.17)$$

where $\frac{\partial \chi}{\partial Q}$ is a Raman tensor (that can be a complex term [64]), χ - is the electronic susceptibility. A and a_0 are terms that can be complex and involve the generation and detection process of the stimulated Raman mechanism [64, 65].

The fractional change in reflectivity, due to the pump pulse, where R denotes the reflectivity before the excitation is given by following relation (derivation in appendix)[63]:

$$\frac{\Delta R}{R} = 2 \text{Real} \left(\frac{\Delta r}{r} \right) \quad (5.18)$$

For all our analysis, we assume that the change of the reflectivity can be related to the change in voltage generated on the photo-diode:

$$\frac{\Delta U}{U} \approx \frac{\Delta R}{R} \quad (5.19)$$

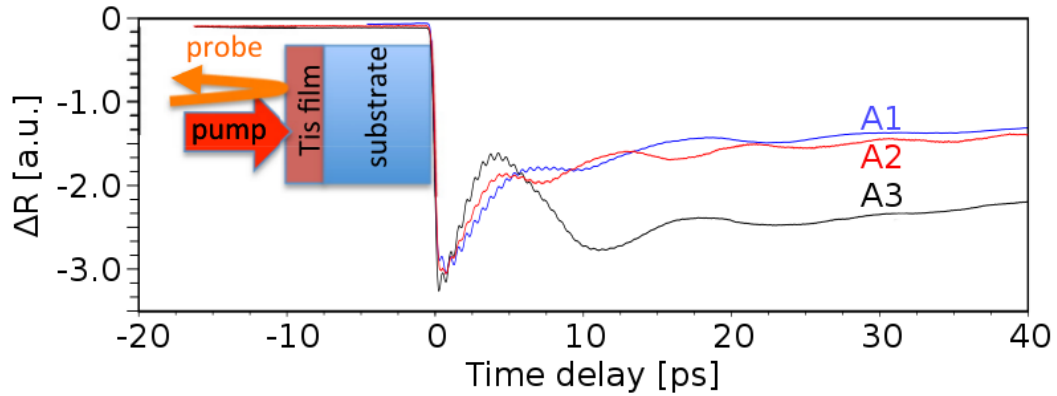


Figure 5.9: Time-resolved optical reflectivity obtained for samples A_1, A_2, A_3 , data was normalized to largest magnitude for clarity.

5.2 Femtosecond laser spectroscopy - results

5.2.1 Role of structural order on electron and phonon dynamics

Samples described in this section are a perfect example of how different structures influence the obtained time-resolved optical response [29]. The time-resolved optical reflectivities obtained for the three samples are shown in Fig.5.9. The signals are composed of different contributions. The first sharp variation of the optical reflectivity R corresponds to the electronic excitation by the pump light, with subsequent decay of the out-of-equilibrium carriers. Within the first picoseconds, several oscillatory components appear. The high-frequency component, as shown in Fig.5.10.a, is the signal of the coherent LO phonon A_{1g}^1 , well identified by its characteristic frequency [68, 69, 70, 41]. The fast Fourier transform (FFT) of this high-frequency mode is shown in Fig.5.10.b, the signals in Fig.5.10 also show a rapid birth of low-frequency component before the A_{1g}^1 mode fully decayed.

Although in our setup (Fig.5.8) we used circular probe polarization, which integrates all the contributions from the transient dielectric tensor [65], we were not able to detect the lower frequency transverse mode E_{g1}^1 or the LO mode A_{1g}^2 (Table.2.2). E_{g1}^1 was also not detected

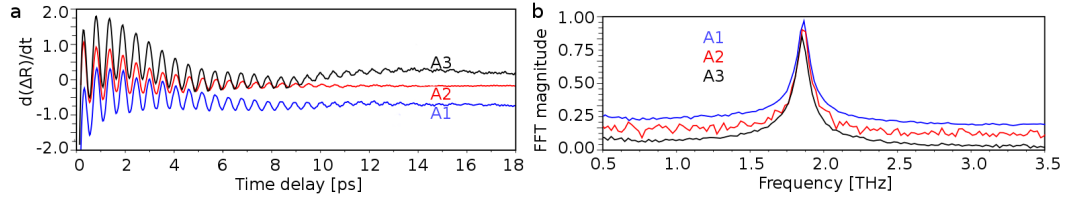


Figure 5.10: a - optical phonon signal obtained through time derivation of obtained signal, we can see a strong signal from A_{1g}^1 mode. b - Fast Fourier transformation of the derived signal.

in other studies on bulk BT [41, 68, 69, 70]. By comparing the A_{1g}^1 frequency (Fig.5.10.b), we could not detect a large difference between samples A1, A2, and A3. The phases in the case of these three samples are very similar as shown in Fig.5.10.a, and we did not detect any significant difference in the decay time of both hot carriers as well as the detected phonon dynamics. This is an indication that the relaxation of the A_{1g}^1 mode is not dependant on long-range crystallographic order, which is in agreement with the observation of a constant Raman linewidth (175cm^{-1}) conducted on cleaved films that showed variable nanostructures such as a change in the number of QL [71]. We know that in case of Bi_2Te_3 this anharmonic coupling (phonon-phonon collision) is the main cause of low thermal conductivity of this material [72, 73]. The detected frequency of A_{1g}^1 , (Fig.5.10.b) shows the same frequency as in bulk crystal and simulations (table 2.2), it is direct proof that the detected coherent optical phonon A_{1g}^1 originates from the Bi_2Te_3 structure with the right chemical environment, what is in direct agreement with performed by us x-ray photoelectron spectroscopy analysis. Consequently, the slight excess of Bi in film A1 and the excess of Te in films A2 and A3 might be isolated in the structure, probably within an interlayer between QLs for Bi and Te as suggested in the previous chapter [50].

We have to remember that despite the random distribution of Bi_2Te_3 grains in film A2 and A3 or the existence of crystallized terraces in film A1, the generation and the detection of A_{1g}^1 mode is very efficient. Thus it lets us believe that the main mechanism behind this process is due to the large and localized coupling between hot electrons and the A_{1g}^1 mode.



Figure 5.11: Optical phonon vibrations are confined to the unit cell and do not create a force that would act on the whole layer.

The mechanism of ultrafast generation of symmetry A_{1g}^1 modes has already been discussed in the literature [66] and is usually attributed to a hot electron-phonon coupling that preserves the lattice symmetry. However, the discussion of the quantitative generation process needs knowledge of the electron-phonon coupling parameter, which is usually lacking. In case of Bi_2Te_3 , recent calculations have shown that the isotropic electron/optical phonon deformation potential is in fact as large as $d_{e-op} \approx 40eV$ [73]. We have reported (Fig.5.10.b) that for our nanostructures, the A_{1g}^1 mode has the same frequency as bulk BT. This indicates that the inter-atomic potentials are similar in bulk BT and our nanostructures (for the case of enough thick layer, i.e., bulk-like layer) so that it is reasonable to use a bulk electron/optical deformation parameter, as a first approximation, to discuss the photo-induced forces. Then, following the conventions used in semiconductor physics [67], the associated photo-induced stress driven by the deformation potential can be written as:

$$\sigma_{e-op} = -d_{e-op}N$$

where N is the photo-excited carrier concentration. Since d_{e-op} is positive, this indicates first that in the early stage of excitation, there is an expansion of the BT QL's. With a concentration of photo-excited carriers of $N \sim 0.5 \cdot 10^{27}m^{-3}$, the photo-induced stress becomes as large as $\sigma_{-op} \sim -3GPa$. The force that induces atomic motion in case of optical phonons can be defined as:

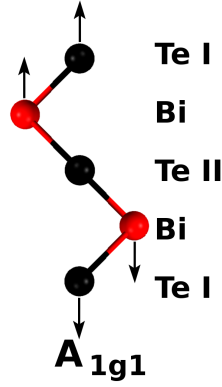
$$F_{e-op} \approx \frac{\partial \sigma_{e-op}}{\partial x}$$

Because the motion is confined (Fig.5.11) down to $h = 1QL \sim 1nm$ this force becomes:

$$F_{e-op} \sim \frac{\sigma_{e-op}}{h} = 3 \cdot 10^{18} Jm^{-4}$$

In magnitude, which is similar to what has been estimated for the A_{1g}^1 mode in Bi for an equivalent range of pump excitation [74]. It is worth emphasizing that this force does not depend on the nanostructure thickness. This is the reason why, based on our observations and our theoretical estimates, we believe that this electron/optical deformation potential mechanism could be the driving mechanism of the coherent A_{1g}^1 excitation. The photo-induced stress can, of course, be smeared because of hot electron diffusion, but we think that it should be somehow limited within a QL because of van der Waals contacts. If we consider that each QL is nearly isolated or poorly connected, due to the van der Waals bonds, then the photo-excited carriers can be contained mostly within each QL. We can assume as well that the electrons are evenly distributed within each QL. We can show that, at a Fermi velocity of $V_F \sim 3.6 \cdot 10^5 ms^{-1}$ [75], the distribution of hot electrons over a distance of 10 nm takes 30 fs. The photo-excitation induces an expansion of each QL which corresponds to 1D-like breathing of each QL. This motion is in agreement with the symmetric atomic motion of the A_{1g} LO mode sketched in Fig.5.12.

The second dominant contribution in the detected signal comes from photo-induced coherent acoustic phonons. The detected acoustic vibrations provide us with information about the elasticity of Bi_2Te_3 in confined geometries and on the electron-acoustic phonon coupling (Figs.5.13.a-c). Observed light-induced coherent acoustic phonons dynamics for the three samples show a clear difference. Conducted experiments, with a characteristic penetration depth of pump light of $\xi \sim 10nm$, assure us that several QLs are nearly simultaneously excited by the pump beam. Excitation like that allows a simultaneous in-phase motion (mechanical resonance) as already observed in similar experiments on different thin films [76, 77] or nanoparticles [78]. In the case of samples from group A, we have to take into account the elastic boundary conditions between the BT-substrate interface, to estimate the efficiency of the acoustic phonon confinement. For that, we calculate the acoustic reflection coefficient that

Figure 5.12: A_{1g}^1 optical phonon mode in Bi_2Te_3

is defined by [76, 77]:

$$R_{ac} = \frac{Z_{film} - Z_{substrate}}{Z_{film} + Z_{substrate}}$$

Where the impedance $Z = \rho V$ with ρ is the mass density, and V is the sound velocity in the material. In the case when the film and substrate impedances are different, then a part of the coherent acoustic phonons is confined. Such a situation will lead to the out-of-plane vibration of the nanostructures [76, 77]. According to the literature (bulk longitudinal sound velocity $V_{Bi_2Te_3} = 2600ms^{-1}$ [79], $\rho_{Bi_2Te_3} = 7460kgm^{-3}$) in case of bulk Bi_2Te_3 the acoustic impedance is similar to that of silicon (100) ($V_{Si} = 8400ms^{-1}$, $\rho_{Si} = 2200kgm^{-3}$) but much larger than that of mica ($\rho_{mica} = 2790kgm^{-3}$ and out-of-plane velocity $V_{mica} = 5027ms^{-1}$ [80]). As a consequence, for a perfect film-substrate interface, we expect no acoustic confinement as in the case of a sample deposited on silicon. All those conditions are met for film A2, where almost all energy of generated acoustic phonon is being transmitted into the Si substrate ($R_{ac} \sim 0.03$). Generated acoustic phonon is then detected in the substrate with the Brillouin mode signature, whose frequency is $f_{Si} = 2n_{Si}V_{Si}/\lambda = 115GHz$. What is in agreement with our observations (Fig.5.13.e), in case of a probe wavelength fixed at $\lambda = 582nm$ and $n_{Si} = 4$ [81]. In order to better understand this vibration, we fitted it with the following function:

$$R_{ac}(A2) \sim \cos(2\pi f_{A2}t + \varphi_{A2})e^{-t/\tau_{A2}}$$

with $f_{A2} = 111\text{GHz}$ and $\tau_{A2} = 24\text{ps}$ (dotted line in Fig.5.13.b). On the other hand, for film A1, the detected vibration is not that of a Brillouin nature in the mica substrate. Estimation of the Brillouin frequency gives $f_{mica} = 2n_{mica}V_{mica}/\lambda = 27\text{GHz}$, with $n_{mica} = 1.6$ [82]. The detected vibration observed in film A1 is actually mechanical resonance of eigenmodes due to the confinement of acoustic phonons ($R_{ac} \sim 0.17$). The fast Fourier transformation shown in Fig.5.13.d is a direct evidence of two modes existence:

$$f_1 \approx 80\text{GHz} \text{ and } f_2 \approx 160\text{GHz}$$

with $f_2 \sim 2f_1$. This is the result of the resonator harmonics generated in this sample, whose frequency is given by:

$$f_n = \frac{nV_{A1}}{2H_{A1}}, \text{ with } n = 1, 2, 3, \dots$$

where V_{A1} is the longitudinal sound velocity of film A1 and H_{A1} its thickness (Fig.5.8.g). Performed numerical fit using only the fundamental mode gives:

$$R_{ac}(A1) \sim \cos(2\pi f_1 t + \phi_{A1}) e^{-t/\tau_{A1}}$$

with $\tau_{A1} = 14\text{ps}$ (Fig.5.8.a) gives a very close match with the detected signal. Thanks to this model, we were able to obtain $V_{A1} = 2460\text{ms}^{-1}$, which is a very close to theoretical estimates in bulk Bi_2Te_3 ($\sim 2300\text{ms}^{-1}$) [83] and estimates obtained in pump-probe experiments performed on $\text{Bi/Sb})_2\text{Te}_3$ superlattice ($\sim 2600 \text{ m s}^{-1}$) [79]. Taking the mass density of the stoichiometric Bi_2Te_3 film, $\rho = 7642\text{kgm}^{-3}$, we can calculate the elastic constant for axial compression:

$$C_{33} = \rho \times V^2 \approx 36 - 46\text{GPa}$$

what is in accordance with other calculations [73]. We were able as well to explain this model vibration detected in sample A3. Contrary to what one may think even (though the film was grown on silicon similarly to A2), we were not able to observe only the Brillouin mode in the silicon substrate. The FFT showed in Fig.5.13.f shows a minimal Brillouin signal in Si,

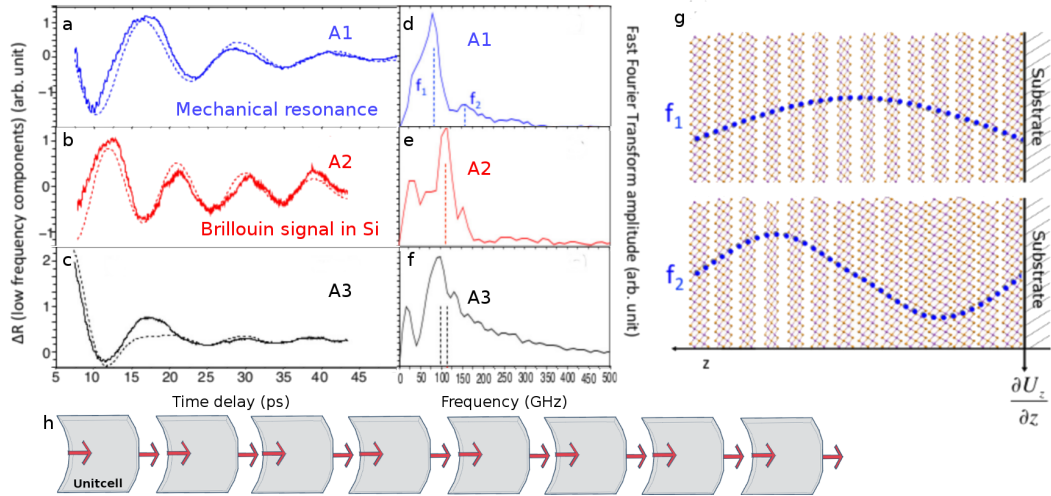


Figure 5.13: a–c Coherent acoustic phonon signals extracted from the transient optical reflectivity signals. For clarity, curves have been scaled in amplitude. Dotted lines are numerical adjustments (see text for more details). d–f Corresponding coherent acoustic phonon spectra obtained by a fast Fourier transform (FFT). (g) The first two confined acoustic eigenmodes in film A1. U_z is the normal displacement of atoms.

with additional modes not resolved yet. A numerical fitting (Fig.5.13.c) has been done with two damped cosine frequencies indicated by dotted vertical lines similar to the previous two samples (Fig.5.13.c), but it was almost impossible to reproduce the obtained signal. One of the explanations of this phenomenon would be the existence of complex interfaces and multilayer composition as well as the polycrystalline texture of Bi₂Te₃ as shown by RHEED page 47. In this situation, the sound velocity is a mixture of in- and out-of-plane sound velocity.

For sample A1 probing the assemblies of QLs with coherent acoustic phonons provided us with new insights into the QL van der Waals interactions. What is the case for most of the solids bonded with Van der Waals interaction [76] the macroscopic and mesoscopic elastic modulus originates from the Van der Waals contacts. If we assume that this is the case in

sample A1, then it is possible to obtain elastic constant of Te-Te Van der Waals force:

$$C_{VdW} \sim C_{33} \times a_{Te-Te} \sim 12 - 16 Nm^{-1}$$

where the distance between two QLs is $a_{Te-Te} = 0.364nm$ [84]. Our estimates are giving a value that is 1.5 to 2 times larger than previously obtained macroscopic measurements [84]. Of course, we have to remember that the constant C_{VdW} is ten times larger than real Van der Waals interactions that exist in rare gas crystals [73].

Last but not least, it is crucial to discuss the physical origin of the acoustic phonon emission further. We can estimate that the driving mechanism of generated coherent acoustic phonon is of an electronic nature. Calculation of the photo-induced thermoelastic stress caused by the rapid lattice heating that follows the electronic decay according to standard model [85] takes the form:

$$\sigma_{Th} = -3\beta B \Delta T \sim 0.1 - 0.2 GPa$$

with the bulk modulus $B \approx 37 GPa$ [73], out-of-plane Bi_2Te_3 thermal expansion $\beta = 2 \cdot 10^{-5} K^{-1}$ [86], and the lattice heating $\Delta T = \Delta E / C_L \approx 60 K$, where lattice heat capacity is equal to $C_L = 1.5 \cdot 10^6 Jm^{-3} K^{-1}$ [87] and laser pump energy absorbed per unit of volume $\Delta E = N \cdot 1.495 eV \sim 10^8 Jm^{-3}$ (the temperature increase is obtained with a fluence of $0.1 mJcm^{-2}$ without taking into account the heat conductivity close to the interface). This thermoelastic stress seems to be much smaller than the stress caused by the electron-acoustic phonon deformation potential given by [85, 88]:

$$\sigma_{e-ac} \approx -a_{e-ac} N = -2.5 GPa$$

where $a_{e-ac} = 35 eV$ [73] is the electron-acoustic deformation potential (four times larger than in GaAs [67]), and $N \sim 0.5 \cdot 10^{27} m^{-3}$. The dominating nature of the electron-acoustic phonon deformation potential mechanism is in line with the evaluation of this scattering process [28].

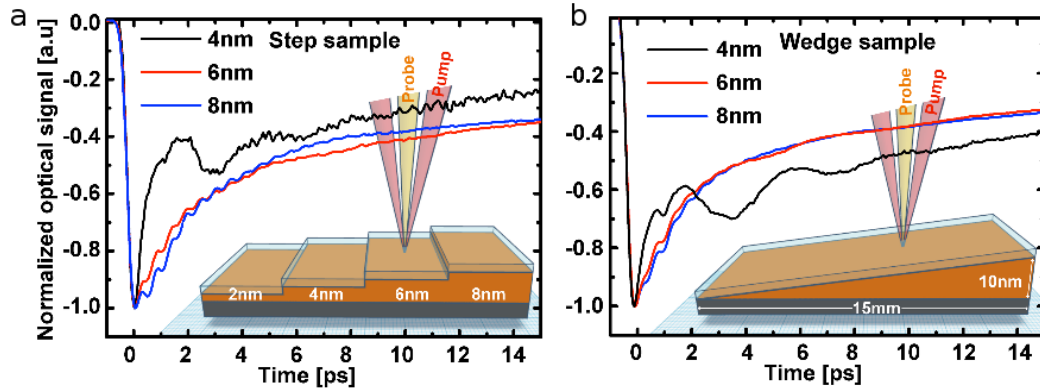


Figure 5.14: Ultrafast optical response of ultrathin layers of Bi_2Te_3 . Time-resolved optical reflectivity obtained for various layers of Bi_2Te_3 for the a - step B1 and b - wedge B2 sample. The signals are normalized to the maximum of the electronic peak. (insets) The pump and probe are represented in the artist's view as red and orange beams.

5.2.2 Quantum confinement effects

The following section presents the results focused on Quantum confinement caused by scaling down the layer of Bi_2Te_3 [12]. Showcased results gave us a clear understanding of the thickness limits of Bi_2Te_3 , which are extremely crucial for the development of new devices based on this material. The experiments were done with a standard front-front configuration with incident pump and probe beams perpendicular to the surface (hexagonal c axis perpendicular to the surface of Bi_2Te_3 , section 2) as shown in Fig.5.9. Pump-probe experiments were conducted with the step sample B1 and wedge sample B2. In our experiments, the pump and probe wavelengths were fixed at 830 nm (1.495 eV) with $\xi = 10.1nm$ and 582 nm (2.13 eV) with $\xi = 9.8nm$ [38]. Such small penetration depth, which was not explained in the previous section, is caused by the specific electronic band structure in this energy range where interband transitions exist [38]. The maximum fluence used during the experiment was in the range of $100\mu Jcm^{-2}$, which corresponds to a photo-excited carrier concentration of around $10^{16}cm^{-3}$. Both pump and probe were focused on a microscope objective providing a typical spot radius

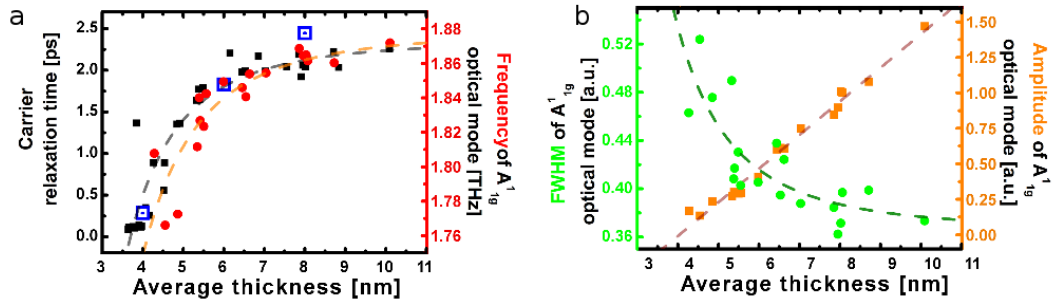


Figure 5.15: Thickness dependence of the ultrafast carrier and phonon dynamics. a - Thickness dependence of the electron-phonon relaxation time for the wedge B2 (black squares) and step B1 (centered blue squares) samples. Thickness dependence of the A_{1g}^1 optical phonon frequency (red dots). b - Thickness dependence of the A_{1g} optical phonon amplitude (gold squares) and full width at height maximum (green dots).

of ≈ 5 micrometers. With this spot diameter and sample length (along the gradient) of around 1.5 cm (very smooth gradient for the wedge sample Fig.3.8) and a width of 1cm, we were able to investigate many positions along and perpendicular to the gradient. This allowed us to get an excellent statistic of transient reflectivity signals that is of utmost importance to reveal subtle properties changes, as shown in this study.

Obtained Time-resolved and thickness-dependent optical reflectivity signals are presented in Fig.5.14 both for the B1 and B2 samples, respectively. The signals can be decomposed into three parts. The first part with a sharp variation to the transient optical reflectivity is the consequence of the electronic excitation. This phenomenon can be modeled with error function Eq.5.2. The second part describes the decay of the signals both by electronic and thermal dissipation of energy. The third part contains oscillatory components generated by the photo-excitation of different phonons (Fig.5.5 green line - phonon signal). Both of electronic decay and the phonons response were separated:

$$\frac{\Delta R}{R} = \frac{\Delta R}{R}_{electron+thermal} + \frac{\Delta R}{R}_{phonons}$$

Where the electronic and thermal contribution is composed of signal due to the excitation of the pump beam and the decay described by two exponential functions. The extracted decay times show the first extremely fast decay time τ_1 ranging from 85fs to 2ps attributed to hot carriers relaxations. The slower part τ_2 with a time spanning from 30 up to 60 ps can be associated with long-living carriers and thermal relaxation processes (Eq.5.6). For both the step (B1) or wedge sample (B2), we observed a huge modification of the carrier relaxation time (Fig.5.15.a) and phonons dynamics (Figs.5.15). In figure 5.15. we can see that for thick Bi_2Te_3 layers, the characteristic time of hot carrier relaxation τ_1 is close to $\tau_0 = 2.2ps$. This time is very similar to the relaxation of hot carriers (electron and hole) for bulk Bi_2Se_3 [92, 93] and bulk Bi_2Te_3 [94]. While for most confined Bi_2Te_3 (especially below 5nm) layers, the electron-phonon relaxation time is drastically evolving down to around 200 fs (Fig.5.10.a). This evolution of time relaxation can be described by the power of law function similar to the energy levels in quantum well system:

$$\tau_{e-ph} = \tau_0 - \frac{A}{L^\alpha} \quad (5.20)$$

where L is the thickness of the sample (black dashed line in Fig.5.15.a). This experimental observation indicates that the carrier's relaxation process efficiency is almost ten times larger in the thinner Bi_2Te_3 layer than in bulk like BT layer. We have to point out that we were not able to obtain a signal for the thinnest 2nm layer of the step sample B1. The obtained vibrations for thick Bi_2Te_3 films reveal clearly the A_{1g}^1 mode at 1.82 THz (Fig.5.16.b) in accordance with the literature [29, 96] and our reference samples (group A).

Presented time-domain optical phonon signals revealed slight optical phonon A_{1g} softening (red dots in Fig.5.15.a and 5.16). As well as a decrease of the lifetime (green Fig.5.15.b) of the optical mode. Such change in the lifetime is direct proof that a modification of the interatomic potentials that might occur for the system with strong confinement. This softening of the A_{1g}^1 frequency (around 4%) and raise in the damping time (reverse of FWHM) for ultrathin layers is in line with the observations made in Raman scattering experiments performed on Bi_2Se_3 [91, 97] and in Bi_2Te_3 [98]. The fact that this A_{1g}^1 softening occurs both with phonons

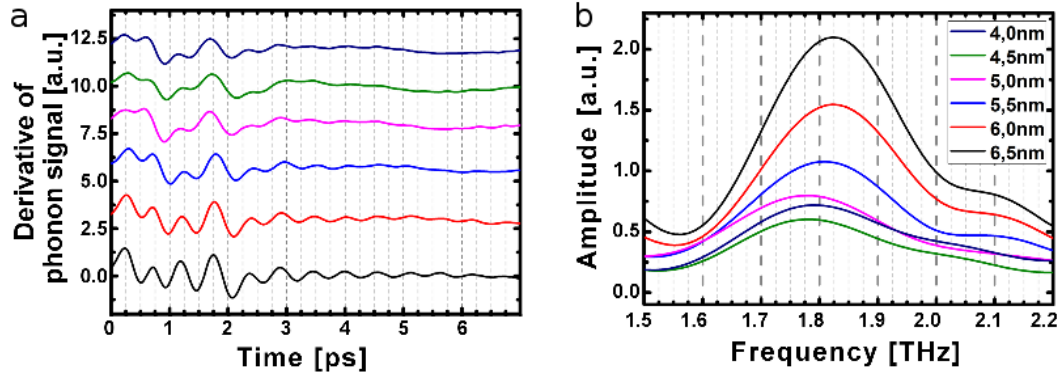


Figure 5.16: a - Typical oscillatory component at a short time scale revealing the A_{1g} optical phonon. b - Fast Fourier Transform (FFT) of the signal shown in a reveal that the A_{1g}^1 mode is softening for the ultrathin layer.

that are photo-excited with a laser pulse or with thermally excited phonons is one of the clues pointing that the softening does not originate from the hot electrons-driven potential softening (as known for bismuth crystal [99, 81]).

We can say that the size dependence we report is relevant to the entire volume of the deposited layer. Based on the observations of band structure thickness dependence which confirms that the electronic structure evolves for ultrathin layer [9, 100, 101]. The presence of the passivated layer that is a trivial phase in the sense of topology should be neutral to the surface states. We can report that the sample thickness (L) dependence is similar to that of the electronic levels (ΔE) in known quantum wells systems that are expected to follow [82]:

$$\Delta E = \frac{A}{L^\alpha}$$

where $\alpha = 2$ and can take different power of laws (α) attributed to complex effects of the confinement, such as in the case of nanocrystals [102]. In our study, we have fitted the relaxation time according to a phenomenological power law versus thickness L and found that presented above equation describes our system with $\alpha = 2.6$ and $\tau_0 = 2.2ps$ Fig.5.17. What is surprising similar power of law applies well for describing the softening of the A_{1g}^1 optical mode fre-

quency and its lifetime (Fig.5.15 dashed lines). That is as if a common phenomenon correlates these parameters, but we do not have theoretical supports at that time. We have to remember that in our situation TIs nanolayers are confined only in one direction while nanocrystals are 3D quantum-confined systems. We know that we can relate the electron-hole relaxation time to both the matrix element (deformation potential term in the Hamiltonian [103]) and the density of states (according to the Golden Fermi rule). The relationship between this experimental law and electronic structure that evolves with thickness remains challenging since a fully electronic and phonon dispersion curves are needed for bulk and surface states. Fortunately, there exist other possible explanations of this phenomenon. With the reduction of the system size, the efficiency of the carrier's surface trapping is known to rise. Since the probability for the electron to reach the surface per unit of time is much higher when the mean free path of electrons is similar in size to that of the sample thickness. Such surface recombination is the channel of efficient relaxation in semiconductor nanocrystals and in materials where the quantum size effect influence on the electron-phonon coupling [104]. Another interpretation in the case of metallic nanoparticles is based on the removal of electron-ion screening interaction. This effect is caused by lowering the carrier density near the surface, which contains a large number of atoms in comparison to the bulk for few nm nanoparticles with radius R [105, 106]. The following phenomenological equation describing the scattering rates was proposed:

$$\frac{1}{\tau_{e-ph}} = \frac{1}{\tau_0} + \frac{V_F}{\alpha R}$$

where τ_0 is bulk electron-phonon relaxation time, α an adjustable coefficient and V_F is the Fermi velocity [105]. Another interpretation was proposed in the case of Bi_2Se_3 thin films, in which the decrease of the relaxation time was attributed to the size-dependent Fröhlich interaction [107]. In our case, we can think about possible trapping at the oxide cap layer. Such trapping could lead to increased damping of hot carriers, even if it is difficult at that stage to evaluate this contribution. It has been shown that the interband scattering channel range of the bulk-surface occurs up to 5 nm in Bi_2Te_3 compounds [75]. This observation is in perfect agreement to the critical thickness that we estimate and could be a possible indication that

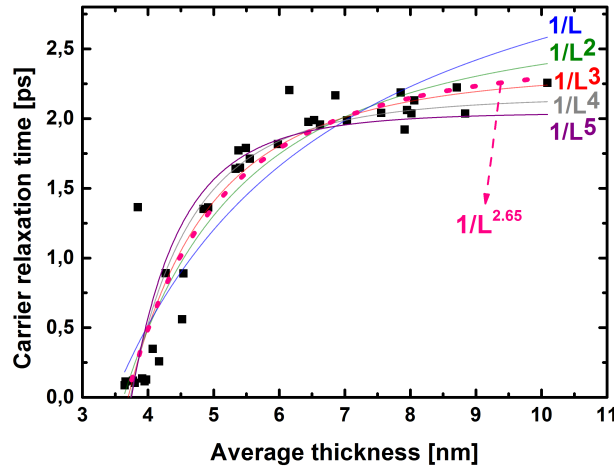


Figure 5.17: Results of fitting the power of law function to the time of relaxation of hot carriers versus the film thickness. The performed calculation resulted in the relaxation of the fitting procedure close to $\alpha = 2.65$.

the observed anomaly is a crossover from the 3D to the 2D system. Such interpretation is supported by the fact that the coupling between surfaces Dirac fermions wavefunctions from opposite sides of a thin layer has occurred in a range of few nm for BS. What is more, it is possible to detect it even in 10nm films. The additional effect could as well play a crucial role in this process, such as likely band bending, that was already observed at the free surface of a bulk crystal [108]. This would suggest that such a situation could be enhanced in confined layers of Bi_2Te_3 near the opposite surfaces. All the above-mentioned factors: the modification of the bulk electronic levels; the surface band bending; the hybridization of two opposing surfaces states; as well as the A_{1g} optical phonon softening that we report. Together correspond to a modification of the electron-ion interaction; in other words, the deformation potential parameter, which in turn influences the carrier relaxation time rate in the case of electron-phonon collision processes. The particular case of the electron-acoustic phonon deformation is now discussed on the basis of the analysis of the coherent acoustic phonon signal. We can notice first that the assignment of the origin of the acoustic phonon contribution is straightforwardly

established by the linear dependence of the period of oscillation with the BT layer thickness, as shown in Fig. 5.18b. Secondly (as shown in Fig 5.19) that the acoustic phonon signal is highly size-dependent and exhibits a resonant-like behavior for a thickness around 5nm. We try to propose an explanation in the following discussion.

Due to the evolution of electron band structure with thickness in TI, the electron-hole acoustic deformation potential is dependant on the thickness of the material [9, 101]. In order to find the thickness dependence of the deformation potential we have to consider that the excited electrons (and holes) rapidly thermalize down(/up) to the CB(/VB) (Fig.5.4), in this case the relevant deformation potential is d_{33} which is close to the bandgap E_g [59, 60, 63]:

$$d_{33}^{ac-eh} = \frac{\partial E_g}{\partial \eta_{33}}$$

This approximation is met when the frequency of the detected acoustic oscillation is smaller than the inverse of the time of thermalization in the CB and VB. The discussed acoustic phonons correspond to the thin film eigenmodes, i.e., those inducing an out-of-plane strain η_{33} . The strain associated with the acoustic eigenmode is directly connected to the layer thickness change (dL) with:

$$\eta_{33} = \frac{dL}{L}$$

in consequence, the electron-hole acoustic phonon deformation potential takes the form:

$$d_{33}^{ac-eh} = L \frac{\partial E_g}{\partial L}$$

The information about the bandgap dependence is available in literature for Bi_2Se_3 and Bi_2Te_3 compounds [9, 101], this allowed us to estimate the experimental parameter $L \frac{\partial E_g}{\partial L}$. The evaluated thickness dependence is presented in Fig.5.19.b (blue curve); it reveals the enhancement of the deformation potential parameter when reducing the thickness. In the presented graphic, we normalized the received value to the maximum of the experimental amplitude for easier comparison. There is, however, a clear deviation for the ultrathin layer where the calculated deformation potential cannot explain the sudden decrease of the experimental phonon amplitude. We believe that this effect comes from a detection process that can be numerically

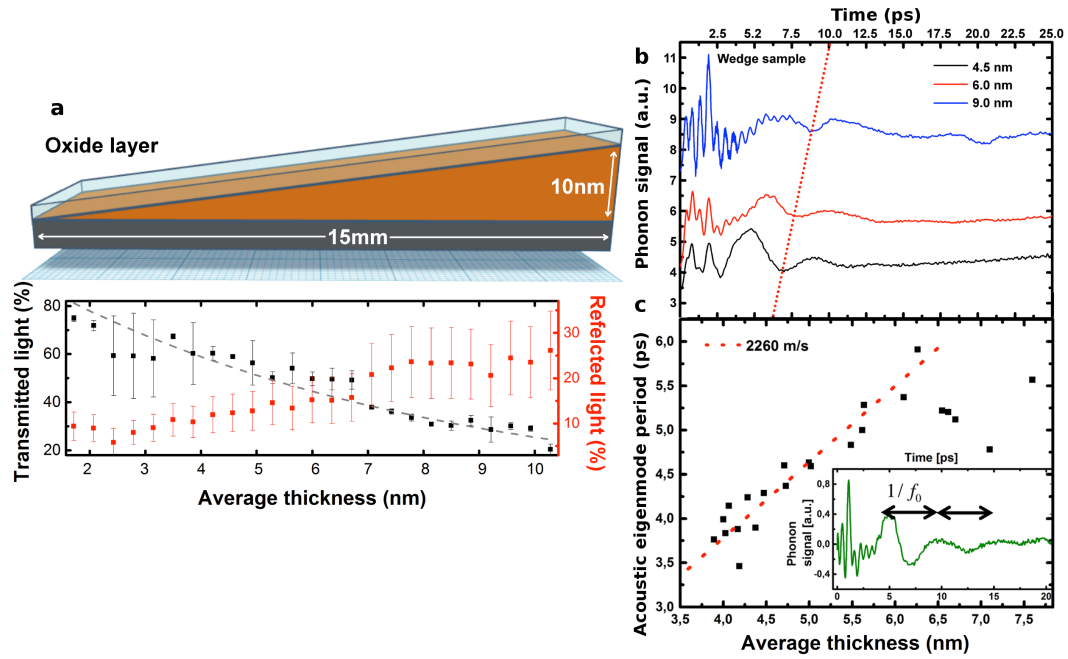


Figure 5.18: a - Art view of the cross-section of the C2 wedge sample together with continuous wavelength optical transmission, with a dashed curve, we presented calculated Beer-Lambert law, and with red reflectivity along thickness gradient. b - Contribution of the phonons signal to the transient reflectivity signal for three different thicknesses. d - Thickness dependence of the longitudinal acoustic resonance eigenmode period $1/f_0$. The red dashed slope provide an estimation of the longitudinal sound velocity of 2260m/s in Bi_2Te_3 . Inset shows an example of an acoustic signal with the period $1/f_0$ for the 6nm layer.

estimated as described below. We have realized a calculation of the contribution of coherent acoustic phonons to the transient optical reflectivity (detection process). Considering that none of the physical parameters change but only the thickness is reduced. To do that we have calculated the coherent acoustic phonon contribution to the transient optical reflectivity following the standard method [109, 110, 111]. We have performed this calculation by considering the first acoustic eigenmode (f_0) strain field contribution whose standard expression is:

$$\eta_{33}(z,t) = A \times \sin\left(\frac{\pi z}{L}\right) e^{i\omega_0 t}$$

where A is the amplitude and $\omega_0 = 2\pi f_0$. We can show that the contribution of deformation potential to the transient optical reflectivity can be calculated with the standard model where the optical reflectivity magnitude for normal incidence pump-probe experiment Eq.4.3 would possess an acoustic phonon contribution [109, 110, 111]:

$$\left(\frac{\Delta R}{2R}\right)_{ac-ph} \approx \text{Re}[-4i \times C \times r_{12} k_1 \frac{L}{\pi} e^{i\omega_0 t} - iC \frac{\partial k_1}{\partial \eta_{33}} \int_0^L A \times \sin\left(\frac{\pi z}{L}\right) e^{i\omega_0 t} \left(r_{12} e^{-ik_1[L-z]} + e^{ik_1[L-z]}\right)^2 dz] \quad (5.21)$$

with optical parameter C dependant on optical parameters of Bi_2Te_3 is:

$$C = \frac{1 - r_{01}^2}{r_{01} e^{ik_1 H} + r_{12} e^{-ik_1 H}} \times \frac{1}{e^{ik_1 H} + r_{01} r_{12} e^{-ik_1 H}}$$

where r is the complex optical reflectivity coefficient of the non-perturbed system, k_i is the probe wavevector in medium i (0, 1 and 2 are respectively air, BT layer, and the Mica substrate) and $u(z)$ is the normal mechanical displacement of the transparent layer at a position z. The notation r_{33} is used for the optical reflection coefficient at the interface between medium i/j for oblique incident probe beam whose polarization is perpendicular to the incidence plane:

$$r_{ij} = \frac{n_i - n_j}{n_i + n_j}$$

The first term of eq.5.5 corresponds to an interferometric contribution due to the change of the transparent layer thickness induced by the relative interfaces displacement driven by the

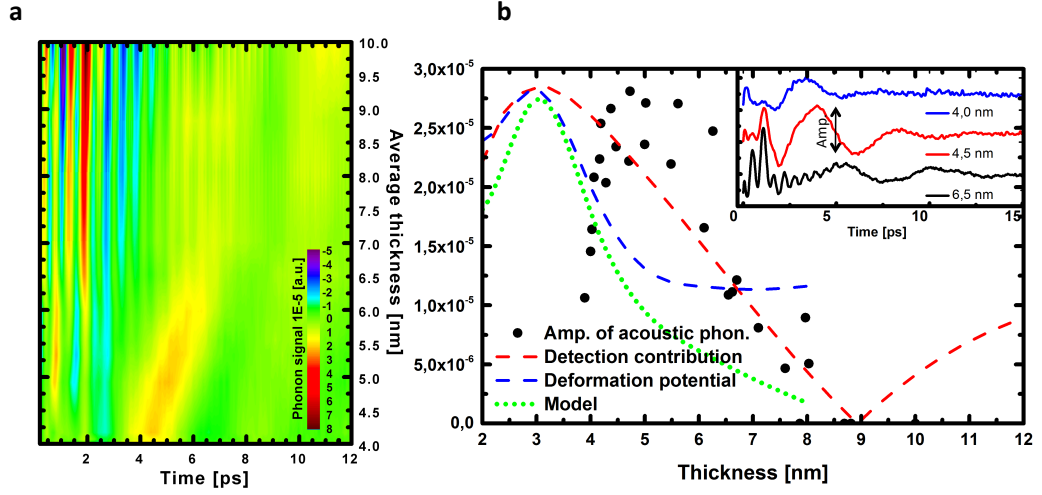


Figure 5.19: Scaling down a layer of Bi_2Te_3 revealed generation of strong coherent acoustic phonon. a - Map of the optical and acoustic phonon mode amplitudes with fixed pump power, the x-axis represents time and y-axis change of layer thickness. The experiment revealed the appearance of large acoustic phonon signals in the ultrathin layer. b - Thickness dependence of the photo-detected coherent acoustic signal amplitude. Green curve present model that takes into account the detection (red) contribution estimated size-dependent electron-hole acoustic deformation potential (blue) from the literature [9].

acoustic strain field. The second term corresponds to the photo-elastic contribution i.e., that due to the modulation of the refractive index by the coherent acoustic phonons strain field. The strain field is coupled to the internal probe light electric field given as the second term (in brackets) in the integral. $z = 0$ corresponds to the free surface of Bi_2Te_3 layer. In this model, we omitted the contribution from the passivated oxide layer. The photo-elastic coefficient $\partial k_1 / \partial \eta_{33}$, it can be derived according to:

$$k_0 \frac{\partial n_1}{\partial \eta_{33}} = k_0 \frac{\partial n_1}{\partial E_{probe}} \times \frac{\partial E_{probe}}{\partial \eta_{33}} = k_0 \frac{\partial (n_1' + i n_1'')}{\partial E_{probe}} \times \frac{\partial E_{probe}}{\partial \eta_{33}}$$

where k_0 is optical wavevector in vacuum and $\frac{\partial E_{probe}}{\eta_{33}}$ the deformation potential coefficient at the probe energy, $n_1 = n'_1 + in''_1 = 1.7 + i4.5$ is the Bi_2Te_3 refractive index at the probe energy $2.2eV$ [38], and that gives. The refractive index of Mica was taken as $n_2 = 1.6$. Equation 4.5 gives time dependant sinusoidal function of transient optical reflectivity signal with corresponding frequency eigenmode. Presented maximal amplitude is not an absolute one due to a lack of the value of deformation potential at the probe energy. It still gives us the ability to discuss the thickness dependence L . Assuming that the sound velocity of the Bi_2Te_3 does not change (Fig.5.18.c), we can say that the amplitude is proportional to the electron-hole deformation potential d_{ac-eh} and the photo-excited carriers concentration N only as [59, 60]:

$$\eta_{33}(z, t) = A \times \sin\left(\frac{\pi z}{L}\right) e^{i\omega_0 t} \propto N(L) \times d_{33}^{ac-eh} \times \sin\left(\frac{\pi z}{L}\right) e^{i\omega_0 t}$$

Because optical properties of Bi_2Te_3 do not show a drastic change at the probe energy, what has been shown with Beer-Lambert law (Fig.5.18.a), we can estimate that the carriers concentration versus thickness is roughly multiplied by two in 4nm compared to 10nm layer. This allowed us to calculate the thickness dependence of the maximum amplitude of the detected acoustic vibration (red dashed curve Fig.5.19.b). As stated before it is impossible to compare directly the absolute values but only the thickness (L) variations; because of this reason, we normalized the curve to the maximum of detected amplitude to be able to discuss the tendency. The presented detection mechanism seems to reproduce the enhancement of the coherent acoustic phonon as well as the lowering of the detected signal in ultrathin layers. By including into this calculation, the thickness-dependent deformation potential we can obtain (Fig.5.19.b green dotted curve) model of the observed effect. Presented curve show similarities in the appearance of the maximum and broadness but show as well a clear shift between the theory and the experiment that is probably due to the necessary approximations, such as value of $L \frac{\partial E_g}{L}$, as well as considering that the photo-elastic coefficient in thickness independent what is likely not true.

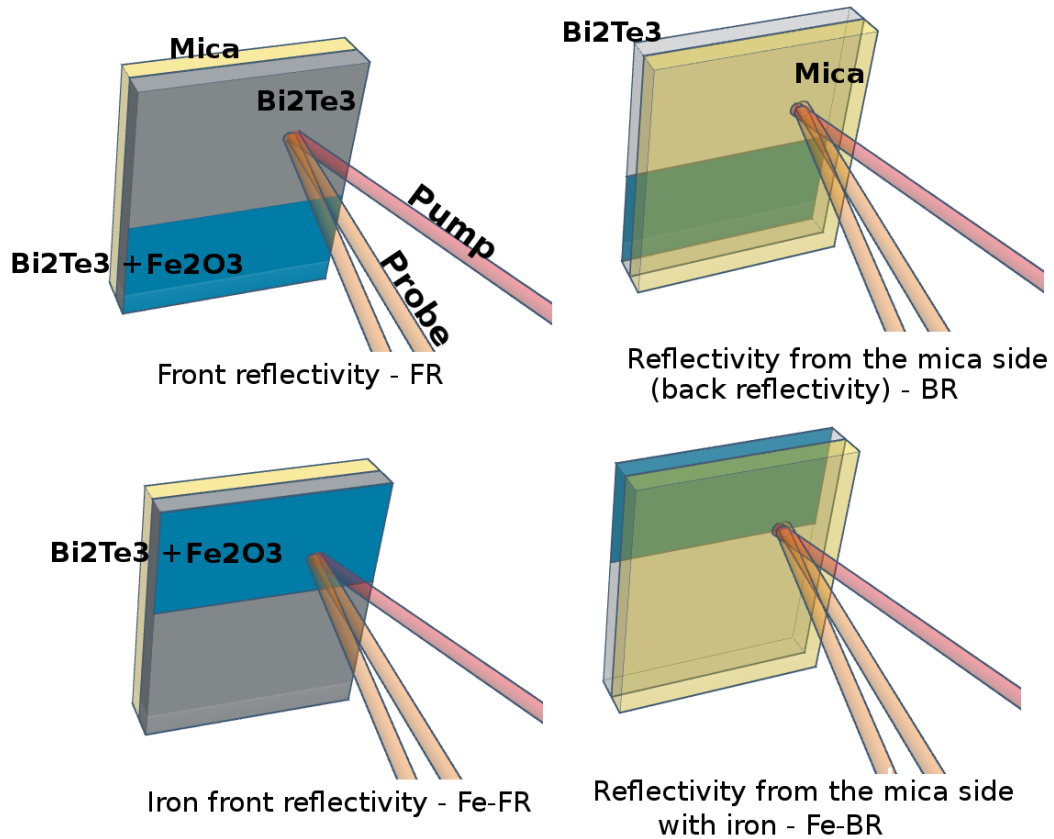


Figure 5.20: All performed configurations of reflectivity measurements made with the sample covered by iron layer.

5.2.3 Influence of iron oxide capping layers

The study of topological insulators entered the state of finding the best possible systems to harness their unique properties. The current research is mainly focused on spin-charge current conversion that requires the presence of a ferromagnetic layer or material with strong spin-orbit coupling [5, 6, 7]. The realization of such devices requires from us the understanding of the interactions of the deposited layers with topological insulators. As well as an understanding of both physical and chemical aspects of those interfaces. In this experiment we focused on changes of hot carrier relaxation time and phonon dynamics in Bi_2Te_3 structure, caused by

the proximity of Fe^{3+} oxide interface, that was in line with previous investigations [34]. In our experiments we used the laser pump with wavelength equal to 830nm (1.49eV) and 415nm (2.98eV) and the probe beam with a wavelength of 580 nm (2.14eV), that is close in energy to the reported indirect bandgap of $\alpha - Fe_2O_3$ at 2.1eV [112, 113, 114] and similar to the direct bandgap of $\gamma - Fe_2O_3$ [115, 116, 117]. Considering these optical properties, we can consider that the iron oxide is nearly transparent at both the pump and probe wavelength. Thanks to that, we can be sure that our pump and probe beams were highly transmitted through the iron oxide layer, and the exciting processes were generated mainly within the layer of Bi_2Te_3 . As shown in the previous section (see part 5.2.2), the dynamics of hot carrier dissipation after the optical excitation can be robustly changed by the modification of the bulk electronic levels, the surface band bending or the hybridization of two opposite surfaces states. The experiments, conducted on the sample C1 covered partially with iron oxide were made with both transmission and reflection geometries, from mica and free surface side (Fig.5.21). This experiment revealed a strong modification of the relaxation time of the hot carriers τ_1 (table 5.1) that at first sight looks very similar to the situation observed in the case of quantum confinement evidenced for the layer of Bi_2Te_3 thinner than 5nm Fig.5.15. On the contrary, the dynamics of hot carriers measured on the sample area where no iron was deposited looks like the signal obtained for "bulk" BT material (see Fig. 5.9 and 5.14).

It is worth to mention that similar relaxation time scales were observed in case of both $\alpha - Fe_2O_3$ and $\gamma - Fe_2O_3$ nanoparticles with decay times spanning from 0.36 up to 67ps [114, 118]. The process was attributed to the recombination of electron-hole govern by intrinsic mid-bandgap states and internal defect-induced trap states, and surface defects that create an additional fast channel of carrier relaxation (Fig.5.21.c). A similar situation was also observed in the case of $LT : GaAs$ [119], in which the excess of As within the structure is dramatically reducing the lifetime of the photo-excited carriers and shows linear change with the precipitate spacing. Because of defects in the bandgap, the recombination of the e-h pairs can be as fast as few ps.

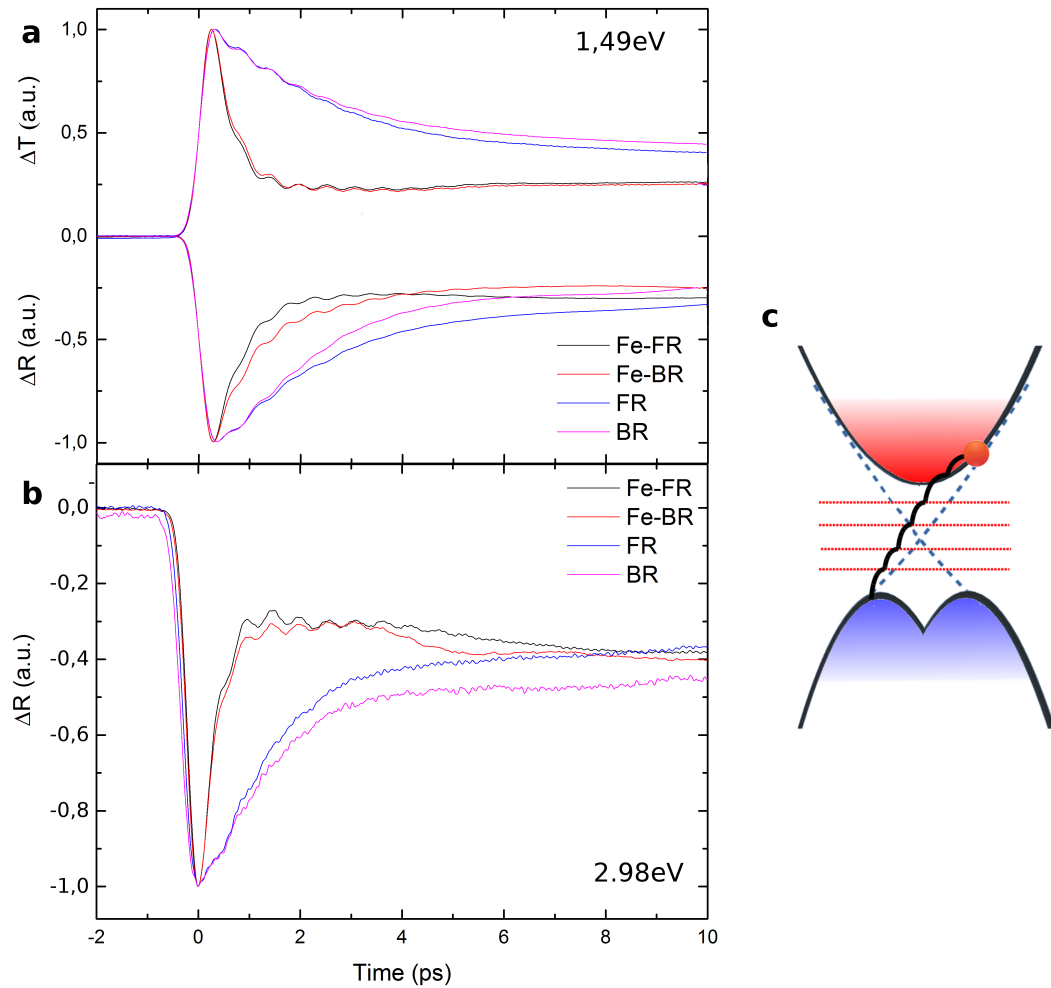


Figure 5.21: a - Time-resolved optical transmission (ΔT) and reflectivity (ΔR) obtained for the sample C1 with a pump wavelength 830nm. Signals, marked with Fe, were made on the part of the sample with iron oxide; the letter B denotes the position of excitation by a pump from the backside (mica side) similar to the front (F). The letters T and R are denoting transmission and reflection. b - Time-resolved optical reflectivity (ΔR) obtained for the sample C1 with a pump wavelength 415nm. c - Schematic of the relaxation process of photo-excited carriers in the presence of mid-bandgap states induced by the proximity of γ - Fe_2O_3 atoms within the structure of Bi_2Te_3 .

In our situation, due to the pretty large bandgap of iron oxide, as said previously, we can exclude the contribution from the intrinsic response of iron oxide. However, as presented in Fig. 4.21, the depth profile analysis revealed, aside from the presence of the $\gamma\text{-Fe}_2\text{O}_3$ layer directly on top of Bi_2Te_3 , the possible appearance of diffused iron atoms within the Bi_2Te_3 structure. These iron atoms in insertion as sketched in the inset of Fig. 4.21, can act as a defect and can create some states in the band gap (or elsewhere) in the BT band structure. As a consequence, these scattering centers may accelerate the hot carrier's relaxation. However, the existence of the iron oxide on the top of the layer may also have a contribution and may change the electronic structure of the BT layer. The existence of such material near the surface states of the topological layer can indeed lead to a substantial modification of the topological spin structure as already reported in iron-doped Bi_2Se_3 [120, 121]. Contributed to such doping, strong Coulomb and magnetic perturbations are breaking the formation process (Fig.2.1) of TI by directly influencing two crucial steps of Dirac cone formation, the crystal field symmetry, and the spin-orbit interactions. As reported by the direct ARPES measurements [120] such situation leads to bandgap opening in TI surface, what is very similar to the situation caused by scaling down the layer [9] that we have discussed in part 5.22.

As a summary, at this stage, forth origin of the fast relaxation process we evidence, we cannot disentangle the contributions coming from the possible scattering centres (created by the inserted Fe atoms) and the one coming from a possible strong magnetic interaction, that modifies the electronic structure, and consequently the electron-phonon coupling parameters. Despite this current limitation, we show that the interaction of the iron cap layer with a very thin BT layer can be complex. This is again supported by the following discussion regarding the optical phonon (A_{1g}) dynamics.

Besides the modification of the hot carriers lifetime the time-resolved femtosecond pump-probe spectroscopy revealed indeed a clear difference in the excitation of the A_{1g}^1 optical phonon mode in the presence of iron oxide doping Fig.5.22. Thanks to the specific design of the samples from the group C, where the clean part could be used as self-reference, we were

Table 5.1: Extracted with the fitting function E.q.4.1 relaxation times of hot carrier for the sample C1.

Name	τ_1	Name	τ_1	Name	τ_1	Name	τ_1
Fe-FT	350fs	Fe-BT	400fs	FT	2260fs	BT	2090fs
Fe-FR	560fs	Fe-BR	1050fs	FR	2090fs	BR	1990fs

able to directly compare properties such as frequency and amplitude of the generated phonon. Such an approach was necessary due to a higher sampling rate (number of steps of the delay line), used in this experiment, that can directly affect the frequency of the detected vibrations but provides us with much better frequency resolution. All presented data were gathered during a short period, in order to assure the same condition and parameters (such as stability of the laser, humidity, temperature, etc.) of the experiment. In the presented signal, we can see an apparent enhancement of the amplitude of the generated coherent optical mode, which is accompanied by a slight stiffening of A_{1g}^1 . In fig 5.22.b we superimpose the derivative of the transmitted phonon signal, where we can see a difference in the frequency of excited optical mode between doped (from FFT $f_{Fe} \approx 1.82Thz$) and un-doped (from FFT $f_{BT} \approx 1.80Thz$) side, the difference is at the level of about 1,1%. The blue shift of optical phonon mode was observed previously only as a function of the pump fluence or the temperature in material such as graphene, V_2O_3 or gold [122, 123, 124]. In the case of gold, performed ab initio calculations revealed that the blue shift of the phonon modes is induced by the rise of photo-excited electrons temperature (T_e from the TTM model) that increases the crystal's melting temperature [125, 126, 127]. This phenomenon was qualitatively explained by enhanced electronic delocalization accompanied by a decrease in the screening of the attractive nuclear potential leading to effective bond hardening [125, 126]. In the case of graphene, the transient stiffening of the G-mode phonons has been attributed to the reduction of strong electron-phonon coupling. In a situation when Fermi energy is close to the Dirac point, G-mode phonons can efficiently decay into electron-hole pairs. However, in the situation when Fermi energy has

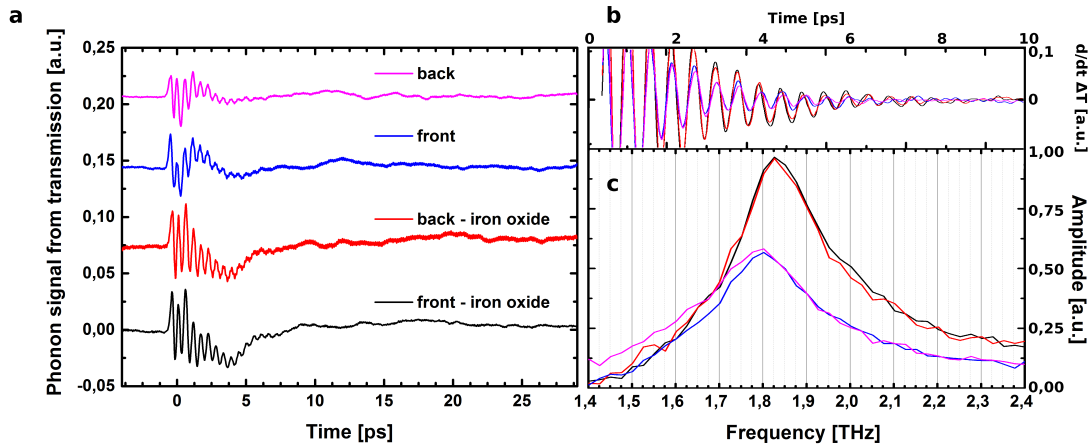


Figure 5.22: Time-resolved transmission (ΔT) obtained for the sample C1. The graph presents the extracted phonon signals. b - presents overlapped derivatives of the signal showing, in real-time, the difference in frequency. Graph c presents the FFT showing the appearance of a blue shift of A_{g1}^1 frequency in Bi_2Te_3 doped with iron oxide.

been shifted from the Dirac point, the process of quick relaxation can be no longer available once the required electron and hole states are no longer present. Such electronic decoupling can lead to an increase of the phonon energy [122]. In the case of the V_2O_3 hardening of the A_{1g} mode was explained by a decrease of the average distance between two closest vanadium atoms induced by the bonding properties of the a_{1g} orbitals. This effect was observed experimentally and confirmed by the $LDA + U$ calculations [123].

With the intention to better evidence this unique blue shift of the A_{1g}^1 optical phonon mode frequency, we prepared the sample C2. The geometry of this sample, similar to the sample B2, allowed us to perform a continuous study of the influence of the iron oxide layer on the properties of Bi_2Te_3 . In figure 5.23. we presented the FFT signal coming from the wedge sample that revealed discrete character as a function of the amount of deposited iron on the phonon hardening. The presented data clearly show the same shift in frequency as in the sample C1 from $f_{BT} = 1.80THz$ to $f_{Fe} = 1.82THz$ and the same enhancement of the detected phonon

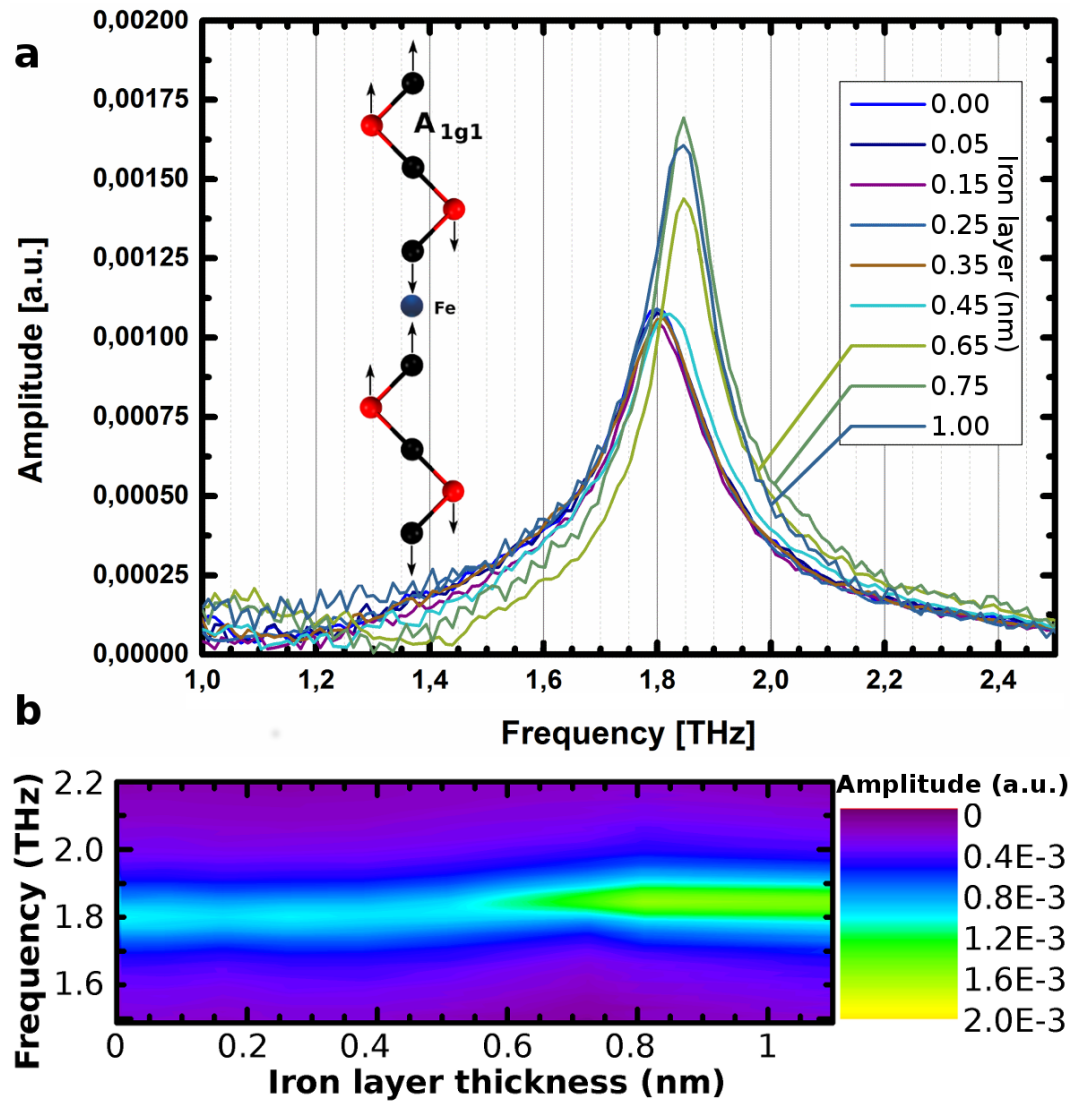


Figure 5.23: a - FFT amplitude from measurements performed on the sample C2 with the iron wedge, signal revealed that the blue shift has discrete nature dependant on the quantity of doping. The frequency shift appears when the relaxation time of the photo-excited electron is faster than $\tau_e < 0.9p$. b - Schematic of A_{g1}^1 optical phonon mode in the presence of iron in between the VdW layer.

amplitude that occurs when the deposited layer of iron is larger than 0.5nm . In fig.5.23.b, we presented the map with a larger quantity of measured points of the detected optical phonon frequency (and amplitude in color) as a function of deposited capping layer thickness. Revealed stiffening of the optical phonon mode can originate from modification of the bonds under light excitation. This effect is similar to the photo-doping effect, which modifies the interatomic potential and in result, leads to the evolution of the molecular bonds. In order to confirm this explanation, we are planning to conduct a study of the pump fluence dependence in the future. The second explanation of the observed phenomena is based on the shift of the Fermi level due to the presence of Fe in the structure, that according to the presented before depth-profiling can be accumulated in between the VdW layers. In this case, the presence of additional structures can lead to a change in the interatomic potential of Bi_2Te_3 QL's leading to the stiffening of the A_{1g}^1 mode. Such stiffening has already been observed on a transverse optical phonon dynamics, in multilayers of graphene [128]. This optical phonon mode was associated with a shear motion between neighbors layer of graphene. It was shown that the increase of the number of graphene layers increased the electrostatic interaction between each layer, leading to a final hardening of the elastic constant and consequently to the blue shift of the phonon frequency. We could imagine a similar scenario in our case, even if modeling and additional experiments are necessary to conclude. In any case, this experimental results show again the necessary detailed investigation of the composite structure associating a cap layer (in that case an iron cap layer) and the BT layer.

Chapter 6

Summary

In conclusion, in this work, we wanted to address a few problems concerning the topological insulators, in particular, bismuth telluride. Bi_2Te_3 due to its vast potential in future electronics requires us a better understanding of the limiting factors, that could put a barrier in future applications. As mentioned before one of the phenomena that so far it was disregarded in the literature was the role of electron-phonon coupling (with A_{1g}^1 mode [27] and strong coupling of 2D surface electrons with LA mode [28]) that set a limit on 2D surface electron transport. Knowing that we tried to tackle this question with complete and thorough chemical and physical investigation performed on films from group A grown by state-of-the-art molecular beam epitaxy. This group consisted of three samples, one of which was deposited on Muscovite Mica, and two deposited on Silicon (001). During their growth, we tried using different parameters of growth to see how they influence the quality of the deposited material. We manage to show differences in crystal structure between the sample from this series. In the case of sample A1, the diffraction image from the RHEED experiment showed a clear presence of tiny terraces that possess two characteristics to the hexagonal cell patterns. The formation of the crystal and its stoichiometry was confirmed as well by the LEED image and XPS spectra (Bi/Te - 46/54). In the case of samples A2 and A3, the RHEED image revealed the formation of a polycrystalline structure that probably originated from the mismatch between Bi_2Te_3 and

silicon (001) substrate. Performed XPS revealed as well that both samples A2 and A3 were rich in Te (A2: 35/65; A3: 33/67) and such composition is causing the formation of the interlayers of Te in between the Van der Waals layers of Bi_2Te_3 [50]. Finally due to diligent analysis of the deposited structures we were able to show with ultrafast two-color pump-probe technique, that it is possible to excite a coherent A_{1g}^1 mode in thin films containing 10 QLs of Bi_2Te_3 with no detectable restriction in their emission, contrary to what was suggested previously in the literature [41]. The A_{1g}^1 phonon dynamics is nearly not disturbed by the nanostructure of the films, which indicates that the phonon decay takes place locally by anharmonic coupling rather than by scattering due to geometrical inhomogeneities like islands or grain boundaries. Our estimates show that the optical-phonon deformation potential photo-induced stress appears to be as high as -3GPa for a photo-excited carrier concentration of $N \sim 0.5 \times 10^{27} m^{-3}$, which is quite large and likely to launch atomic motion of the A_{1g}^1 mode in our nanostructures. It is important to note here that we did not detect two different A_{1g}^1 mode components arising from the so-called bulk and surface phonons as reported on bulk Bi_2Se_3 with time-resolved angle-resolved photoemission spectroscopy [92]. The origin of the difference is not clear yet, since this could be either due to the confinement of our nanostructures or due to the lack of sensitivity of optical methods even if in the particular case of Bi_2Te_3 , the pump/probe light penetrates only around 10 nm, which is still a characteristic distance over which surface and bulk electrons may interact [75]. Besides the A_{1g}^1 phonon dynamics, we also show, before the A_{1g}^1 mode decays, the birth of coherent acoustic phonons whose spectrum drastically depends on the film's nanostructure, contrary to that of the A_{1g}^1 mode. This clearly shows the sensitivity of the longitudinal acoustic modes to the nanostructure arrangement. The generation mechanism of these acoustic phonons is also attributed to the deformation potential mechanism. Finally, the measurement of the time of flight (sound velocity) of these longitudinal acoustic phonons in the single-crystalline film (A1) provides an evaluation of the out-of-plane elastic modulus (36–46 GPa) of these assemblies of QLs.

The second task that we wanted to address with this work was an enhancement of the sur-

face state's contribution to the overall properties of the topological insulator material. In case of ultra-thin films the ratio of surface states to bulk states starts to be not negligible, in the case of thin films, at a critical thickness the surface states from opposite surfaces of the films can couple together and open thickness-dependent gap (Fig.2.4) [9, 31, 32], which is non trivial and may give rise to quantum spin Hall state similarly to HgTe quantum wells [33]. In order to gain a better understanding of the processes of electron and phonon dynamics, under working conditions or exposure to the air, we created second group B of the samples. Thin-film in this series was created in order to better understand the influence of critical thickness in the Bi_2Te_3 [9, 31, 32, 33] on electron and phonon dynamics. We managed to deposit two unique samples on Muscovite Mica with different geometry: one with large steps (that grants us an access to large surface area with uniform thickness that provides a precise description of the thickness dependence), second one with continuous slope (that allow us to conduct experiments with higher number of investigated spots). Chemical and physical investigation of the structural properties of the samples from group B revealed that the deposition technique developed for sample A1 gives stable and repeatable high-quality films of Bi_2Te_3 . Due to the unique opportunity given by planned variation in thickness, we were able to reveal that layers of Bi_2Te_3 tend to grow with Stransky-Krastanov dynamics. Similarly to sample A1, films from group B, shown stoichiometry rich in bismuth, which should, in a result, give a stable superstructure Bi-BT within the QL's. Performed after the oxidation XPS, measurements revealed the existence of a passivated layer ($\sim 2nm$) of Te and Bi oxides, that is stable in time and acts as a protective layer from further degradation of deposited layers. Due to diligent preparation of this set of samples, we were able to reveal in this work a clear modification of the out-of-equilibrium carriers and phonons dynamics when the Bi_2Te_3 layer is reduced to few nanometers. Performed time-domain investigation provided us with a new insight into the size-dependent physical properties of topological insulators, while in the past the size-dependent electronic properties were probed only at the thermodynamic equilibrium. We were able to show a drastic decrease of the electron-phonon relaxation time with an increase of the confinement that before that

was only fully described for semiconductor and metallic nanostructures, while only partially characterized regarding its ultrafast response for BS layers for example [107]. It was possible to assign this effect to a size-dependent electron-hole phonon deformation potential parameter which still needs to be confirmed by ab-initio calculation. One of the most interesting phenomena observed in this experiment was increased of the coherent acoustic phonons signals with the decreasing thickness (L) that could be explained by an enhancement of the electron-hole acoustic deformation potential parameter. The performed experimental optical measurement integrates bulk and surface electrons into the final response, but nonnegligible surface carrier's contribution could exist since our film thickness scaled down with the characteristic to Bi_2Te_3 distance for surface Dirac fermions states to hybridize. Unfortunately, it is difficult to give a quantitative estimate by of separated contributions to the received signal. Apart from the quantum-confinement effect contribution of the carrier surface recombination could as well enhance the carrier relaxation time, especially near the oxidized layer. All these new physical insights showed us that downscaling the layer of topological insulators is changing its properties is not straightforward ways that have to be taken into account for potential TIs based spintronic nanodevices.

The last question that we wanted to address in this work is related to the creation of new devices, that would efficiently use the properties of TI's. Mainly reaction of bismuth telluride to the presence of doping and additional layers [34]. Due to necessity of using ferromagnetic (Fig.2.5) or metallic layers with strong spin-orbit coupling like platinum or cobalt [5, 6, 7], to create working spin-current converters, we have to be able to create stable chemically systems, that would not disturb the topological insulator surface states and would still allow the transfer of generated polarized spin current into other layers. To better understand these processes, we created the last group of samples C. The synthesized films possessed an additional oxidized iron layer. For this study, we created two samples one with a uniform thin cap of iron ($\sim 1nm$) covering half of the sample and a second similar to sample B2 with a uniform continuous wedge of iron ($1nm \rightarrow 0nm$) deposited on $15nm$ layer of Bi_2Te_3 . Such configura-

tions gave us means to directly compare the effects induced by the presence of other materials, on both crystal structure as well as phonon and hot carrier dynamics. Thanks to the design, half of the surface was not covered by the iron element, which consequently permitted us to have an in-situ reference. By this, we were able to eliminate effects that could be induced by different growth conditions and give us a chance to compare the measured signals directly. With performed X-ray photoelectron spectroscopy, we were able to identify the state of iron (Fe^{3+}) and type of the formed oxide ($\gamma-Fe_2O_3$). In order to better understand the created structure, we performed depth profiling of the layer C2 (with an iron wedge) that revealed the presence of iron within the structure of Bi_2Te_3 . Lack of change in energy of core levels of both Bi and Te, characteristic to the formation of Bi_2Te_3 , leads us to the conclusion that the additional iron within the layer might be in the oxidized form or compound with Te. The formed compound containing the iron element seems not to disturb the Bi_2Te_3 structure. The information, received after the analysis of the depth profiling, allowed us to create a possible model, for the Fe-doped superstructure, that was presented at the end of chapter 4. A time-domain investigation revealed first a strong modification of the photo-excited carriers. In particular, the Fe-doped system exhibits a swift electron-phonon relaxation thermalization time in comparison to the iron-free layer. The observed phenomenon could originate from the change in electronic band distribution caused by the proximity of iron within the structure. Such doping within the TI layer can directly influence the Fe-doped layer through a change in the crystal field symmetry and/or through a strong spin-orbit coupling. Consequently, the electron-phonon matrix element would be drastically modified. This possibility has already been discussed in the literature [120,121], but our detailed sample characterization shows that we have to be careful since we evidenced some possible migration over a couple of nanometers of the Fe element. Therefore, this information could be indicated that we form some mid-gap states or internal change in crystal field symmetry and spin-orbit interaction, that still has to be confirmed numerically. An effect like that could as well originate from the appearance of additional mid-bandgap states or internal defect-induced traps that allow fast relaxation of carriers.

The second effect that was observed in this study shows a clear blue shift of the A_{1g}^1 optical mode. Such hardening of the optical phonon mode was only observed in materials such as graphene, gold, or V_2O_3 . The revealed stiffening can originate from two possible mechanisms, similar to the photo-doping evolution of molecular bonds or similar to the case of graphene shift of the Fermi level, in the presence of iron compound between QL's. This presented explanation still requires further study of the material. After achieving promising results from this set of samples, we launched two scientific programs. Their main goal is further investigation of the metallic (Fe, Pt, Ag, Cu, Co, and Au) interface interactions with TI layers, in order to find the optimal structures that could be used in future electronics. The future study will be expanded by addition SQUID, PEEM, ARPES, and Time-resolved Kerr effect and ellipticity rotation.

Chapter 7

Appendix

7.1 Second harmonic generation

Second harmonic generation can occur in crystal materials which lack inversion symmetry and can exhibit so-called $\chi^{(2)}$ non-linearity. This can give rise to the phenomenon of frequency doubling, where an source (pump) wave generates another wave with doubled optical frequency in the medium. In most cases, the pump wave is delivered in the form of a laser beam, and the frequency doubled (second-harmonic) wave is generated in the form of a beam propagating in a similar direction

To better understand the basic concept we should approach it from theoretical point of view. Let us expand the polarization P as power series in energy, in result we receive:

$$P(t) = \epsilon_0[\chi^{(1)}E + \chi^{(2)}E^2 + \chi^{(3)}E^3 + \dots] \quad (7.1)$$

Because $\chi^{(1)} \gg \chi^{(2)} \gg \chi^{(3)} \gg \dots \gg \chi^{(n)}$ and $\chi^{(3)}$ is very small we can leave only two parts:

$$P(t) = \epsilon_0[\chi^{(1)}E + \chi^{(2)}E^2] \quad (7.2)$$

Now let us consider the simplest electromagnetic wave in shape of cosine function:

$$E(t) = E_0 \cos(\omega t) \quad (7.3)$$

and insert it to the simplified equation, we will receive:

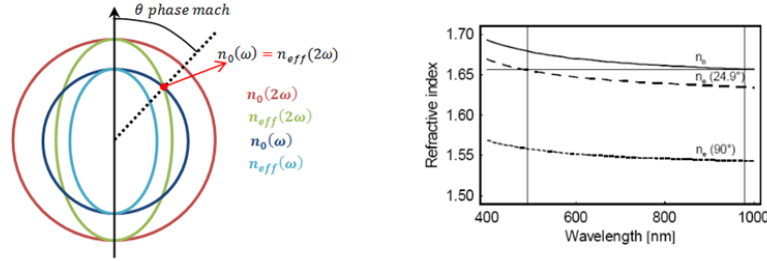
$$P(t) = \epsilon_0 [\chi^{(1)} E_0 \cos(\omega t) + \chi^{(2)} E_0^2 \cos^2(\omega t)] \quad (7.4)$$

$$P(t) = \epsilon_0 [\chi^{(1)} E_0 \cos(\omega t) + \frac{1}{2} \chi^{(2)} E_0^2 (1 + \cos(2\omega t))] \quad (7.5)$$

Where part $\frac{1}{2} \chi^{(2)} E_0^2 \cos(2\omega t)$ is our second harmonic generation. Frequency doubling mechanism can be understood as follows. Due to the $\chi^{(2)}$ non-linearity, the fundamental wave generates a non-linear polarization wave which oscillates with twice the fundamental frequency. According to Maxwell's equations, this non-linear polarization wave radiates an electromagnetic field with this doubled frequency. Due to phase-matching issues, the generated second-harmonic field propagates dominantly in the direction of the non-linear polarization wave.

The phase matching of the radiated electric field of ω and 2ω is crucial in SHG. If both beam would not be in phase they would interfere destructively. The applied electric field is strong enough to generate the second order radiation, but not so strong so that the dominant term is higher, because of that we can think of second harmonic generation signal as a perturbation, and as such is small. To met this phase matching condition both waves should travel our crystal with the same speed, but in order to do that the refractive index for the two different frequencies should be the same. What is not possible in standard medium, but is possible for birefringent crystals, which posses double refractive index. This phenomenon arises from the anisotropy of the crystal structure, in which structure posses ordinary and extraordinary refractive index. In microscopic sense, different molecules radiate in different ways and this leads to difference in refractive index. Crystals which exhibit such properties are for example calcite ($CaCO_3$), ruby (Al_2O_3), barium borate (BaB_2O_4) or even ice. The indices are dependent on both the frequency of light and the angle between propagation and optical axis:

$$\frac{1}{n_e^2(\theta)} = \frac{\sin^2(\theta)}{n_e^2} + \frac{\cos^2(\theta)}{n_o^2} \quad (7.6)$$



and for correct angle $n_{e,2\omega} = n_{o,\omega}$ we can obtain equation for correct angle, at which phase match can exist:

$$\sin^2(\theta) = \frac{n_{o,\omega}^{-2} - n_{o,2\omega}^{-2}}{n_{e,2\omega}^{-2} - n_{o,2\omega}^{-2}} \quad (7.7)$$

So for the particular θ angle we can expect that phase matching conditions might be met. And this is indeed true, as shown in figure 2 in case of BBO crystal. This method is so called angle tuning. Unfortunately ordinary and extraordinary rays with parallel propagation vectors will quickly diverge from one another, and because of that in such structure the overlap between them can only be maintained for a short distance. This effect is so called walk-off. Other methods of generating efficient SHG include non-critical phase matching which is particular case of angular phase matching. Which occurs when ordinary and extraordinary rays intersect at angle $\theta = 90^\circ$, it usually occurs at higher temperatures. But the most efficient technique is so called quasi-phase matching, in periodically alternating structures, which can give high efficiency over a long length of crystal. It can be achieved through mechanical slicing of crystal into thin segments and rotating them by 180° , or in more sophisticated way of inversion of the orientation of the ferroelectric domains by external static electric field. It can be achieved in normal crystals as well as polymer structures, which are much cheaper and easy to deal with.

7.1.1 Frequency mixing and parametric generation of light

Frequency mixing is a process in non-linear crystal materials in which sum frequency generation (SFG) or difference frequency generation (DFG) can occur. In this effect two pump

beams generate another beam with the sum or difference of the optical frequencies of the pump beams. In order for efficient work our pumps needs to be in phase match, and usually there is no simultaneous phase matching for sum and difference frequency generation.

To better understand origins of this effect, lets return to the equation 7.2 for quadratic dielectric polarization, from previous section. And consider a case when two independent sources of light enter non-linear medium. The wave will take following form:

$$E(t) = E_1 \cos(\omega_1 t) + E_2 \cos(\omega_2 t) \quad (7.8)$$

Then let us insert this wave into equation 7.2, in result we will get:

$$P(t) = \epsilon_0 [\chi^{(1)} E + \chi^{(2)} E^2] \quad (7.9)$$

$$= \epsilon_0 [\chi^{(1)} (E_1 \cos(\omega_1 t) + E_2 \cos(\omega_2 t)) + \chi^{(2)} (E_1 \cos(\omega_1 t) + E_2 \cos(\omega_2 t))^2] \quad (7.10)$$

$$= \epsilon_0 [\chi^{(1)} (E_1 \cos(\omega_1 t) + E_2 \cos(\omega_2 t)) + \chi^{(2)} E_1^2 \cos^2(\omega_1 t) + \chi^{(2)} E_2^2 \cos^2(\omega_2 t) + 2\chi^{(2)} E_1 E_2 \cos(\omega_2 t)] \quad (7.11)$$

We can see that aside of SHG terms for ω_1 and ω_2 we obtained additional term:

$$P_{1,2} = 2\epsilon_0 \chi^{(2)} E_1 E_2 \cos(\omega_2 t) \quad (7.12)$$

$$= 2\epsilon_0 \chi^{(2)} E_1 E_2 (\cos([\omega_1 + \omega_1]t) + \cos([\omega_1 - \omega_1]t)) \quad (7.13)$$

that contains sum and difference of beams that enter our medium. Thus, the second-order nonlinear medium can be used to mix two optical waves of different frequencies and generate a third wave at the sum frequency or at the difference frequency. The former process is called frequency up-conversion (or SFG) and is shown in figure 7.1, whereas the latter frequency down-conversion (or DFG) shown in figure 7.2.

Very similar effect to the SFG and DFG can be created with only single coherent pump beam to produce so called signal and idler beams. This effect can be created in so-called optical parametric oscillator. Typical optical parametric oscillator consist of nonlinear crystal placed

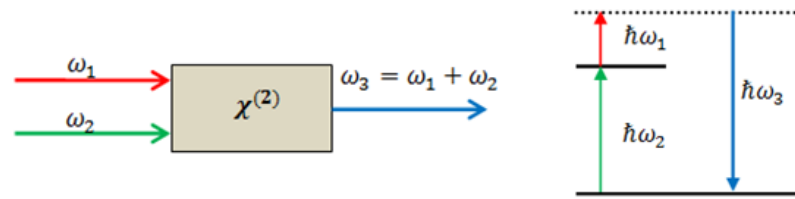


Figure 7.1: SHG process

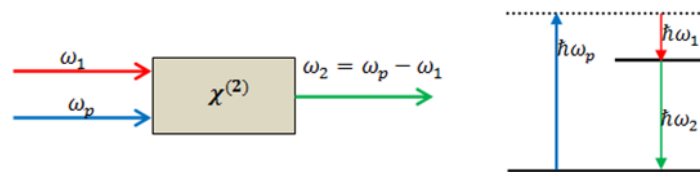


Figure 7.2: DFG process

inside of the optical resonator, as shown in figure 7.1.1. In nonlinear crystal, pump, signal and idler beams overlap. The interaction between these waves leads to amplitude gain for signal and idler waves (so-called parametric amplification) and a corresponding lowering of the pump wave. Created gain allows the resonating waves to continue oscillating in the resonator and compensate the loss that the resonating waves have experienced at each cycle.

OPO is a light source very similar to a laser (also using laser resonator), but it is based on optical gain from parametric amplification in a nonlinear crystal rather than stimulated emission. A main appeal of OPO is that the signal and idler wavelengths, which are determined by a phase-matching condition, can be varied in wide ranges. It is possible to access through OPO wavelengths which are difficult or impossible to obtain from any laser (i.e. green laser light or infra-red light source). Because of this, and the ability to produce output beams with narrow line width and high power, the OPO are very popular in spectroscopy.

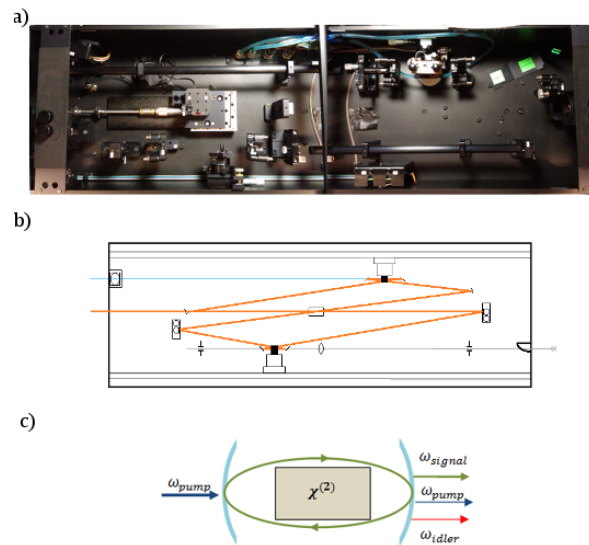


Figure 7.3: a) Photography of used setup; b) Schematic of ring OPO, optical unit with external spectrometer; c) Schematic of OPO.

7.2 Optical parameters of Bi_2Te_3

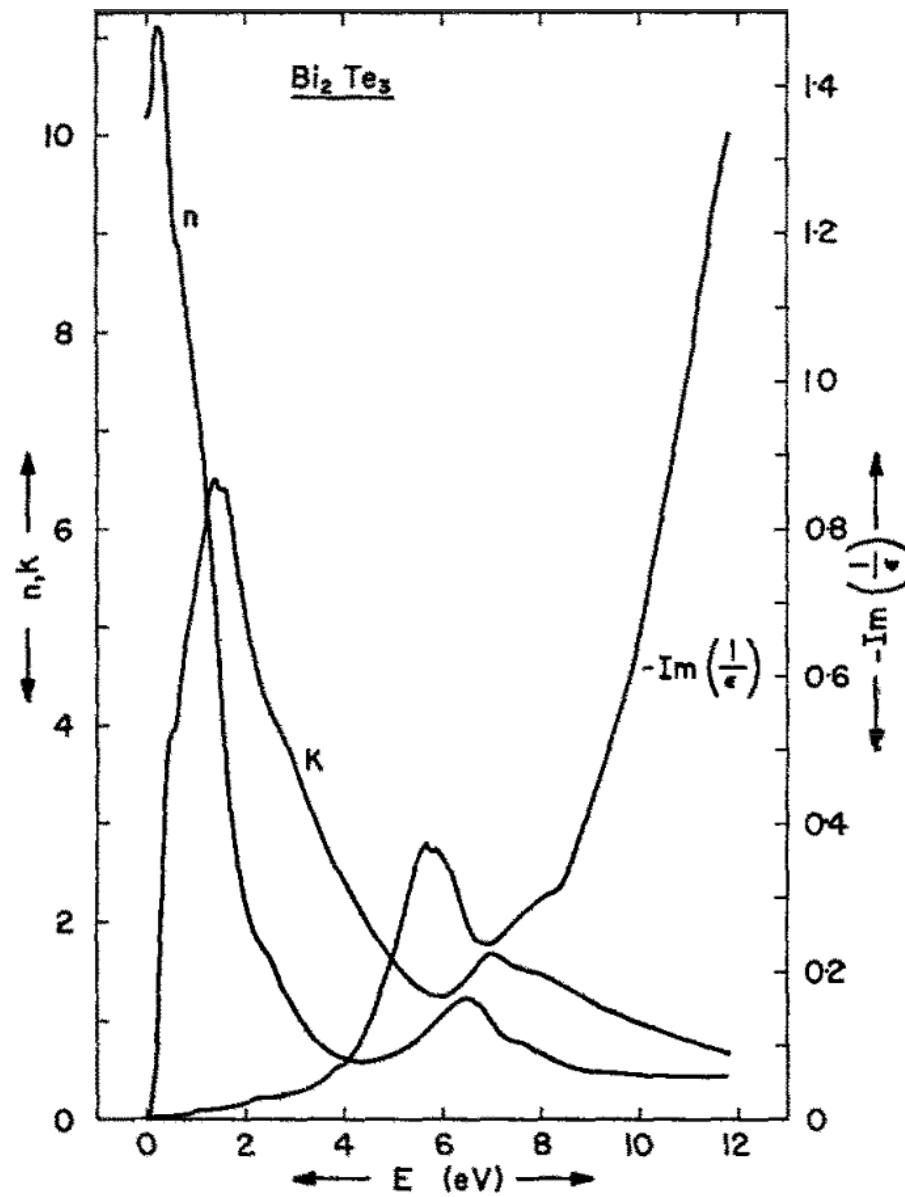


Figure 7.4: Optical constants n and k of Bi_2Te_3 and energy loss function $-\text{Im}(1/\epsilon)$ from Kramers-Kronig analysis, $E \perp c$. From Greenaway J. Phys. Chem. Sol. (1965)[38].

7.3 Reflectivity change

Optical reflectivity is given by:

$$r = r_0 e^{i+\varphi}$$

first derivative:

$$r' = r_0(1 + \varphi) e^{i\varphi + id\varphi}$$

The change of the system reflectivity is given by:

$$\begin{aligned} \frac{\Delta R}{R} &= \frac{r'^* r' - r r^*}{r r^*} \\ &= \frac{r_0^2 r_0^2 \varphi + r_0^2 \varphi^2 - r_0^2}{r_0^2} = 2\varphi + \varphi^2 \end{aligned}$$

we will assume that $\varphi \ll 1$ then the term φ^2 is negligible in result:

$$\frac{\Delta R}{R} = 2\varphi \tag{7.14}$$

The change of optical reflectivity can be defined as:

$$\begin{aligned} \frac{\Delta r}{r} &= \frac{r' - r}{r} = \\ &= \frac{r_0(1 + \varphi) e^{i(\varphi + d\varphi)} - r_0 e^{i\varphi}}{r_0 e^{i\varphi}} = \\ &= (1 + \varphi) e^{id\varphi} - 1 \end{aligned}$$

by Taylor expansion:

$$\frac{\Delta r}{r} = (1 + \varphi)(1 + id\varphi) - 1 = \varphi + id\varphi + i\varphi d\varphi$$

the part $i\varphi d\varphi$ is negligible giving us:

$$\frac{\Delta r}{r} = \varphi + id\varphi \rightarrow \varphi = \text{Real} \frac{\Delta r}{r}$$

knowing that the reflectivity change of the system eq.6.1 takes form:

$$\frac{\Delta R}{R} = 2 \text{Real} \left(\frac{\Delta r}{r} \right)$$

7.4 Publications

PHYSICAL REVIEW B **92**, 014301 (2015)**Ultrafast light-induced coherent optical and acoustic phonons in few quintuple layers of the topological insulator Bi_2Te_3** M. Weis,^{1,2} K. Balin,¹ R. Rapacz,¹ A. Nowak,¹ M. Lejman,² J. Szade,^{1,*} and P. Ruello^{2,†}¹*A. Chetkowski Institute of Physics and Silesian Center for Education and Interdisciplinary Research, 75 Pułku Piechoty 1A, University of Silesia, 41-500 Chorzów, Poland*²*Institut des Molécules et Matériaux du Mans, UMR CNRS 6283, Université du Maine, 72085 Le Mans, France*
(Received 28 January 2015; published 14 July 2015)

Ultrafast lattice dynamics of a few quintuple layers (QLs) of the topological insulator (TI) Bi_2Te_3 is studied with time-resolved optical pump-probe spectroscopy. Both optical and acoustic phonons are photogenerated and detected. Here, in order to get new insights into out-of-equilibrium electron-phonon coupling and phonons dynamics in confined TI, different nanostructures are investigated (single or polycrystalline QL assemblies and nanocrystallized islands). Contrary to previous literature claims, we show that even for nanostructures containing only 10 QLs, the symmetric $A_{1g}(I)$ coherent optical phonon is efficiently photogenerated and no restriction due to structural confinement appears. We also observe that whatever the arrangement of the nanostructures, the $A_{1g}(I)$ optical phonon features are similar (lifetime). We also report the observation of confined coherent acoustic phonons propagating from QLs to QLs whose spectrum is, this time, very sensitive to the atomic arrangement. In the case of the single-crystalline ultrathin film, time-of-flight analysis of these acoustic phonons provides direct estimates of the elastic properties of these nanostructures as well as some estimates of van der Waals interactions between QLs.

DOI: [10.1103/PhysRevB.92.014301](https://doi.org/10.1103/PhysRevB.92.014301)

PACS number(s): 78.66.–w, 63.20.kd, 78.47.D–, 78.47.J–

I. INTRODUCTION

Topological insulators (TIs) are a new electronic state in condensed matter with semiconducting bulk solid and conduction on the surface. Moreover, surface Dirac electronic states exhibit natural spin-polarized current and appear to be robust regarding backward nonmagnetic scattering, which is unique and heralds possible very attractive applications for next-generation spintronic devices [1]. Besides the crucial spin-orbit coupling effect on the features of surface and bulk electron dynamics [2] and the features of confined electrons in two-dimensional (2D) TIs [3], electron-phonon coupling is the object of active discussion and plays a pivotal role in the transport properties of TIs [4–7]. This is also of prime importance for the thermoelectric properties of this class of materials. In particular, it has been observed recently in Bi_2Se_3 (BS) that the longitudinal optical (LO) phonon, with an energy of 8 meV, plays a crucial role in electron scattering and sets a limit on the conductivity [4]. This LO mode is the Raman active mode $A_{1g}(I)$ (2.13 THz in BS [8] and 1.85 THz in Bi_2Te_3 (BT) [9]). Electron-acoustic phonon coupling through the deformation potential also makes an important contribution that likely limits the electrical conductivity [5]. Additionally, some theoretical reports suggest some driving contributions of this electron-phonon coupling in the appearance of the topological state [10]. Witnessing probably the large electron-phonon coupling, it is remarkable that this $A_{1g}(I)$ LO phonon is the one which is efficiently photoexcited by a femtosecond laser optical pulse in bulk BT [9,11,12] or BS [13]. However, Wang *et al.* [14] recently reported that the large confinement of light-induced hot electrons in BT films as thin as 10 nm down to 5 nm cannot lead to sufficiently large photoinduced force to

induce lattice displacement. This peculiar situation could be a drawback from the perspective of manipulation of coherent phonons in such nanostructures. Moreover, these reports could indicate that hot electrons could couple differently in bulk BT than in thin films made of a few BT quintuple layers (QLs; shown in Fig. 1), which is a fundamental question, as well as crucial for applications in future nanodevices. Thin films a few nanometers thick are key nanostructures since they are naturally a rich playground for investigation of electron-phonon coupling with variable ratios of Dirac-like surface electrons to bulk electrons and also because, in the particular case of BT, at least, the characteristic length over which the intervalley scattering process between surface and bulk electrons is effective has been recently estimated as 5 nm, which actually scales with 5 QLs [2].

In this article, femtosecond pump-probe spectroscopy has been used to demonstrate that, contrary to what has been previously proposed, it is actually possible to generate coherent optical phonons in BT nanostructures, and a discussion of the driving force is developed. The mechanisms of excitation and detection are efficient whatever the nanostructure of the system is (single-crystalline film, polycrystalline film, or crystallized islands). The lifetime of the A_{1g} optical mode appears to be fairly insensitive to the long-range crystallographic order, showing that the LO decay is a local mechanism. In addition to optical phonons, coherent acoustic phonons have also been laser generated and detected with this technique. In particular, we report the observation of confined quantized coherent acoustic eigenmodes in a single-crystalline 15-nm-thick film. Analysis of the eigenmode frequencies leads to estimates of the sound velocity (i.e., elastic modulus) along the [001] direction, which is the direction along which the QLs are connected with van der Waals bonds [Fig. 1(c)]. A discussion of electron-acoustic phonon coupling mechanisms is also given.

*jacek.szade@us.edu.pl

†pascal.ruello@univ-lemans.fr

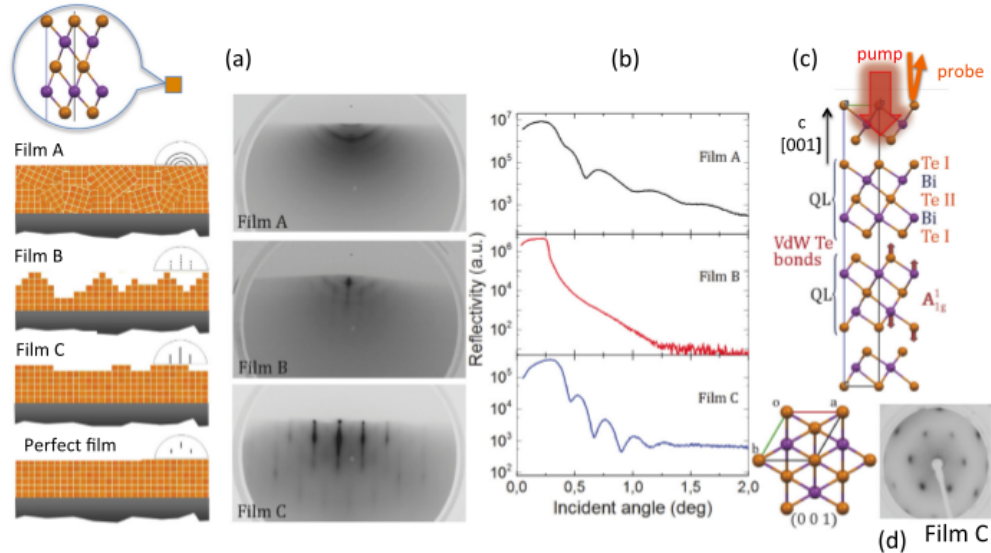


FIG. 1. (Color online) Physical characteristics of thin TI films. (a) Experimental RHEED images for films labeled A–C (see text for details on growing conditions). Corresponding sketches of the nanostructures are shown, where the QL is represented by a sphere, along with the corresponding theoretical RHEED images. (b) The x-ray reflectivity spectra. (c) Crystallographic structure of Bi_2Te_3 , with QLs connected through van der Waals Te bonds. (d) LEED image of film C showing its single crystallinity and the sixfold symmetry of the (001) plane.

II. SAMPLE GROWTH AND METHODS

All studied films of Bi_xTe_y of various compositions were grown on Si(100) or mica (muscovite) substrates by thermal evaporation with the use of a molecular beam epitaxy system from Prevac. Growth was performed in the codeposition mode. Electronic and crystallographic characterizations were carried out *in situ* with the use of x-ray photoelectron spectroscopy, reflection high-energy electron diffraction (RHEED), low-energy electron diffraction (LEED), and atomic force microscopy. Additionally, *ex situ* x-ray reflectivity (XRR) measurements were performed. Figure 1 shows the different characteristics of each BT film. Preparation of the Si substrate and details of the films grown on Si (samples A and B) are given in our earlier work [15]. Film C was deposited on a (110) freshly cleaved Muscovite mica substrate (Ted Pella, Inc.) which was then annealed at 230 °C in the molecular beam epitaxy chamber for 1.5 h. For both types of substrate it was kept at 130 °C during the deposition. The deposition rate was controlled by a quartz crystal microbalance. Film A shows a polycrystalline structure, while for sample B the well-visible streaks in the RHEED pattern indicate at least a partial long-range atomic order on the surface [Fig. 1(a)]. For sample B we found no oscillations in the XRR results [Fig. 1(b)], which can be related to a large roughness detected in the atomic force microscopy tests where a root mean square (RMS) value of up to 5–6 nm (per $1 \mu\text{m}^2$) was obtained. This film was then arranged more according to some crystallized islands induced by the growing process. It is noteworthy that the RMS value for the substrates was lower than 1 nm. For

film C deposited on mica, the electron diffraction experiments [RHEED in Fig. 1(a) and LEED in Fig. 1(d)] show that this film is single crystalline. The thickness of the films was derived from the quartz crystal microbalance and XRR data. For sample C grown on mica a good agreement was found between the data obtained from two methods (about 15 nm). For sample A, the BT layer has a thickness close to 10 nm, but fitting of the XRR data indicates the presence of an overlayer of a lower density and a thickness of about 7 nm. The upper layer is formed probably by Te and tellurium oxides. The x-ray photoelectron spectroscopy analysis (not shown) allowed us to determine the atomic composition and chemical state of the components. All the films appeared to be free of any contamination and the atomic composition characterized by the Bi/Te ratio varied from 34/66 (film A), through 44/56 (film B), to 46/54 (film C). Analysis of the most prominent Bi and Te photoemission lines showed, for films B and C, only one chemical state with the positions of the characteristic lines of BT [15]. For sample A an additional line in the Te 3D spectrum was found which could be assigned to pure Te. The Bi_xTe_y system is known to form many layered nanostructures, especially for compositions $y/x < 3/2$. The stacking sequence of the QLs, characteristic for BT, and additional layers of Bi leads to the formation of many structures [16].

The pump-probe technique used here is based on an 80-MHz-repetition-rate, Ti:sapphire femtosecond laser. The beam is split with a polarizing beam splitter into a pump and a probe beam. The probe beam is introduced in a synchronously pumped Optical Parametric Oscillator (OPO)

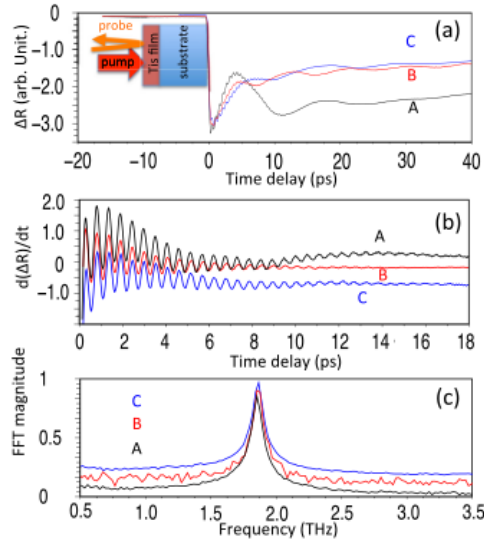


FIG. 2. (Color online) (a) Time-resolved optical reflectivity obtained for Bi_2Te_3 thin films deposited on various substrates: films A–C (see text for details on samples). Curves have been normalized to the largest magnitude point for clarity. (b) $\text{A}1\text{g}(\text{I})$ optical phonon signals. (c) Corresponding fast Fourier transform of curves shown in (b).

that allows us to tune the wavelength and, finally, to do two-color pump-probe experiments (pump and probe are linearly and circularly polarized, respectively). The transient optical reflectivity signals are obtained thanks to a mechanical stage delay (delay line) which enables control of the arrival time of the probe beam with regard to the pump pulse excitation. Experiments were conducted using a front-front configuration with incident pump and probe beams perpendicular to the surface as shown in Figs. 1(c) and 2(a). In our experiments, the pump and probe wavelengths were fixed at 830 nm (1.495 eV) and 582 nm (2.13 eV), with a corresponding absorption length of ~ 10.1 and ~ 9.8 nm [17]. This very small penetration depth is due to the specific electronic band structure in this energy range where interband transitions exist [17]. In particular, in the energy range of around 1.2–2.2 eV, there is sharp variation of both the real and the imaginary parts of the dielectric constant, which is a favorable situation for the detection of phonons [18,19]. Furthermore, in the experiments, the pump and probe are focused with a microscope objective providing a typical spot radius of $\approx 5 \mu\text{m}$. Additional details on the setup can be found in previous articles [20,21].

III. RESULTS AND DISCUSSION

The time-resolved optical reflectivities obtained for the three samples are shown in Fig. 2(a). The signals are composed of different contributions. The first sharp variation of the optical reflectivity R corresponds to the electronic excitation

by the pump light, with subsequent decay of the out-of-equilibrium carriers. Within the first picoseconds, several oscillatory components appear. The high-frequency component, as shown in Fig. 2(b), is the signal of the coherent LO phonon [$\text{A}1\text{g}(\text{I})$], well identified by its characteristic frequency [9,11,12,14] and whose corresponding atom displacements are shown for the structure displayed in Fig. 1(c). The fast Fourier transform (FFT) of this high-frequency mode is shown in Fig. 2(c). The signals in Fig. 2(a) also show a rapid birth of low-frequency components [coherent acoustic phonon spectra shown in Figs. 3(a)–3(c)] even before the $\text{A}1\text{g}(\text{I})$ mode decays.

These results, contrary to previous reports [14] and for a similar range of photoexcitation, show that it is actually possible to generate and to detect coherent optical phonons $\text{A}1\text{g}(\text{I})$ in BT nanostructures containing 10 QLs and no apparent restriction exists on the photoinduced forces for the investigated pump fluence range 0.005–0.1 mJ cm^{-2} . Although we monitored the detection of coherent phonons with circular probe polarization, which integrates all the contributions from the transient dielectric tensor [19,22], we did not detect the lower frequency transverse optical mode [$\text{Eg}1(\text{I})$] or the LO mode $\text{A}1\text{g}(\text{II})$. $\text{Eg}1(\text{I})$ was also not observed in studies on bulk BT [9,11,12,14]. If we now compare the $\text{A}1\text{g}(\text{I})$ frequency [Fig. 2(c)], no detectable difference is reported among polycrystalline film, single-crystalline film, and crystallized islands. The phases of these modes are also very similar as shown in Fig. 2(b). No significant difference in the decay time appears, indicating that the decay of the LO mode is not so sensitive to the long-range crystallographic order, in agreement, for example, with the observation of a constant Raman linewidth (mode at 175 cm^{-1}) observed for exfoliated films having variable nanostructures, i.e., a variable number of QLs of BS [23]. This property indicates that the LO mode [$\text{A}1\text{g}(\text{I})$] does not propagate in the film, due likely to the very low group velocity and due to the rapid damping caused by the intrinsic anharmonic decay (phonon-phonon collision). This anharmonic coupling is known to be large in BT and leads to a low thermal conductivity [24,25]. We actually know how sensitive optical phonons are to the unit cell force distribution. As a matter of fact, this FFT feature (same frequency as in bulk crystal) is thus direct proof that the detected coherent optical phonon $\text{A}1\text{g}(\text{I})$ comes from the right BT structure with the right chemical environment, in agreement with our x-ray photoelectron spectroscopy analysis. Consequently, the slight excess of Bi in films B and C and the excess of Te in film A might be isolated in the structure, probably within interlayers as already suggested by XRR for film A and probably within an interlayer between QLs for Bi as suggested in the literature [16].

Generation of the $\text{A}1\text{g}(\text{I})$ mode even with 10 QLs must be discussed. Because of the large pump optical absorption in the case of our experiment, the relevant mechanism is not impulsive stimulated Raman scattering (called IRSR or electrostriction), which does not require light absorption as stated years ago in the literature [22]. Furthermore, it is important to emphasize that, despite the random distribution of BT grains in film A or the existence of crystallized islands (film B) [see RHEED images in Fig. 1(a)], the generation/detection of the $\text{A}1\text{g}(\text{I})$ mode is still efficient and remarkable similarities are reported for the experimental properties of the $\text{A}1\text{g}(\text{I})$ mode. Thus we believe that the mechanism is due to a large

density and V the sound velocity) of the film is close to that of the substrate, then the acoustic phonons generated in the TI film are transmitted nearly perfectly into the substrate (no confinement of acoustic phonons, i.e., the acoustic reflection coefficient $R_{ac} = (Z_{film} - Z_{substrate}) / (Z_{film} + Z_{substrate}) \ll 1$ [21,27]). If the film and substrate impedances are different, then a portion of the coherent acoustic phonons is confined, leading to out-of-plane ringing of the nanostructures [21,27]. Based on literature data known for bulk BT, it appears that the acoustic impedance (bulk longitudinal sound velocity $V_{BT} = 2600 \text{ m s}^{-1}$ [29], $\rho_{BT} = 7460 \text{ kg m}^{-3}$) is very close to that of (100) silicon ($V_{Si} = 8400 \text{ m s}^{-1}$, $\rho_{Si} = 2200 \text{ kg m}^{-3}$) but clearly larger than that of mica ($\rho_{mica} = 2790 \text{ kg m}^{-3}$ and out-of-plane velocity $V_{mica} = 5027 \text{ m s}^{-1}$ [30]). As a consequence, for a perfect film/substrate interface, no acoustic confinement is expected for film deposited on silicon. This situation is actually met for film B, where most of the acoustic phonon energy is transmitted into the Si substrate ($R_{ac} \sim 0.03$). The emitted acoustic phonons are then detected in the substrate as evidenced by the Brillouin mode in Si characterized by the frequency $f_{Si} = 2n_{Si}V_{Si}/\lambda = 115 \text{ GHz}$, in agreement with observations [Fig. 3(e)], where $\lambda = 582 \text{ nm}$ and $n_{Si} = 4$ [31]. A numerical adjustment with a damped cosinus function gives $\Delta R_{ac}(B) \sim \cos(2\pi f_B t + \phi_B)e^{-t/\tau_B}$ with $f_B = 111 \text{ GHz}$ and $\tau_B = 24 \text{ ps}$ [dotted line in Fig. 3(b)]. On the other hand, for film C, the mode that is detected is not that of a Brillouin nature in the mica substrate (a similar estimate shows that the Brillouin frequency is expected at $f_{mica} = 2n_{mica}V_{mica}/\lambda = 27 \text{ GHz}$, with $n_{mica} = 1.6$ [32]). The oscillatory components detected for film C actually correspond to mechanical resonance eigenmodes due to the confinement of acoustic phonons ($R_{ac} \sim 0.17$). The FFT shown in Fig. 3(f) evidences two modes ($f_1 \approx 80 \text{ GHz}$ and $f_2 \approx 160 \text{ GHz}$ with $f_2 \sim 2f_1$). This is the sequence of the expected harmonics of our resonator, whose frequency is given by $f_n = nV_C/2H_C$, with $n = 1, 2, 3, \dots$, where V_C is the longitudinal sound velocity of film C and H_C its thickness [Fig. 3(g)]. A numerical adjustment with only the fundamental mode gives $\Delta R_{ac}(C) \sim \cos(2\pi f_1 t + \phi_C)e^{-t/\tau_C}$, with $\tau_C = 14 \text{ ps}$ [Fig. 3(c)]. Thanks to this resonator model, we immediately obtain $V_C = 2460 \text{ m s}^{-1}$, which is consistent with theoretical estimates in bulk BT ($\sim 2300 \text{ m s}^{-1}$) [33] and with previous estimates obtained in pump-probe experiments carried out on a BT/Sb₂Te₃ superlattice ($\sim 2600 \text{ m s}^{-1}$) [29]. Considering the mass density of the stoichiometric BT film, $\rho = 7642 \text{ kg m}^{-3}$, this leads to an elastic constant $C_{33} = \rho \times V^2 \approx 36\text{--}46 \text{ GPa}$, also in accordance with recent calculations [25]. Finally, according to this model, and because film A was grown on silicon too, we should observe only the Brillouin mode in the silicon substrate. The spectrum in Fig. 3(d) shows a small Brillouin signal in Si, with additional modes not resolved yet. A numerical adjustment [Fig. 3(a)] has been done with two damped cosinus frequencies indicated by dotted vertical lines in Fig. 3(d) and hardly reproduces the experimental signal. Because of the complex interfaces and multilayer composition as well as the polycrystalline texture (the relevant sound velocity is probably a mixture of out-of-plane and in-plane sound velocity), this spectrum requires further investigations which are not the topic of the present paper.

Furthermore, in the case of film C, probing the assemblies of QLs with coherent acoustic phonons could provide new insights into the QL van der Waals interactions. Usually in van der Waals bonded solids [21] the macroscopic/mesoscopic elastic modulus is driven by the van der Waals contacts; as a matter of fact, if we consider that this is the case for the 1D assemblies of QLs, then we obtain a Te-Te van der Waals force elastic constant of the order of $C_{v\text{dW}} \sim C_{33} \times a_{\text{Te-Te}} \sim 12\text{--}16 \text{ N m}^{-1}$, where the Te-Te distance between two QLs is $a_{\text{Te-Te}} = 0.364 \text{ nm}$ [34]. These estimates are 1.5 to 2 times larger than previous values obtained thanks to macroscopic measurements [34]. As noted previously, we must keep in mind that these constants $C_{v\text{dW}}$ remain 10 times larger than real van der Waals interactions existing in rare gas solids [25].

Finally, it is necessary now to discuss the physical origin of the acoustic phonon emission. A rapid estimate shows that the driving mechanism of coherent acoustic phonon generation is of an electronic nature. Evaluation of the photoinduced thermoelastic stress (σ_{Th}), due to the rapid lattice heating that follows the electronic decay, can be done following the standard model [35]. We find $\sigma_{Th} = -3\beta B \Delta T \sim 0.1\text{--}0.2 \text{ GPa}$, with $B \approx 37 \text{ GPa}$ the bulk modulus [25], $\beta = 2 \times 10^{-5} \text{ K}^{-1}$ [36] the out-of-plane BT thermal expansion, and $\Delta T = \Delta E / C_L \approx 60 \text{ K}$ the lattice heating, where $C_L = 1.5 \times 10^6 \text{ J m}^{-3} \text{ K}^{-1}$ [37] is the BT lattice heat capacity and $\Delta E = N \times 1.495 \text{ eV} \sim 10^8 \text{ J m}^{-3}$ the total laser pump energy per unit of volume absorbed by the material (this maximum temperature increase is obtained with a fluence of 0.1 mJ cm^{-2} and without considering the heat conductivity at the film/substrate interface). This thermoelastic stress is much smaller than the electron-acoustic phonon deformation potential stress given by [35,38] $\sigma_{e-ac} \approx -a_{e-ac} N = -2.5 \text{ GPa}$, where $a_{e-ac} = 35 \text{ eV}$ [25] is the electron/acoustic deformation potential (four times larger than that in GaAs [18]) and $N \sim 0.5 \times 10^{27} \text{ m}^{-3}$. The prevailing contribution of the electron-acoustic phonon deformation potential mechanism is also consistent with the evaluation of this scattering process made on the basis of recent transport properties measurements [5].

IV. SUMMARY

In summary, thanks to a complete ultrafast two-color pump-probe investigation performed on various films grown by state-of-the-art molecular beam epitaxy, we show that it is possible to excite a coherent Alg(I) LO mode in thin films containing 10 QLs, and no restriction appears. The Alg(I) LO phonon dynamics is nearly not disturbed by the nanostructure of the films, which indicates that the decay takes place locally by anharmonic coupling rather than by scattering due to geometrical inhomogeneities like islands (film B) or grain boundaries (film A). Our estimates show that the LO deformation potential photoinduced stress appears to be as high as -3 GPa for a photoexcited carrier concentration of $N \sim 0.5 \cdot 10^{27} \text{ m}^{-3}$, which is quite large and likely to launch atomic motion of the Alg(I) mode in our nanostructures. It is important to note here that we did not detect two different Alg(I) mode components arising from the so-called bulk and surface phonons as reported recently on bulk BS with time-resolved angle-resolved photoemission spectroscopy [39]. The

M. WEIS *et al.*PHYSICAL REVIEW B **92**, 014301 (2015)

origin of the difference is not clear yet, since this could be either due to the confinement of our nanostructures or due to the lack of sensitivity of optical methods even if in the particular case of BT, the pump/probe light penetrates only around 10 nm, which is still a characteristic distance over which surface and bulk electrons may interact [2]. This point will need to be clarified in the near-future. Besides the LO phonon dynamics, we also show, before the LO mode decays, the birth of coherent acoustic phonons whose spectrum drastically depends on the film's nanostructure, contrary to that of the LO mode. This clearly shows the sensitivity of the longitudinal acoustic modes to the nanostructure arrangement. The generation mechanism of these acoustic phonons is also attributed to the deformation potential mechanism. Finally, the measurement of the time of flight (sound velocity) of these longitudinal acoustic phonons in the single-crystalline film

(C) provides an evaluation of the out-of-plane elastic modulus (36–46 GPa) of these assemblies of QLs. As a final perspective, the coexistence of both optical and acoustic phonons could make these systems a rich playground for studying LO–longitudinal acoustic anharmonic couplings, which are two important phonon populations involved in thermal properties [24,25].

ACKNOWLEDGMENTS

We thank G. Vaudel, V. Gusev, and A. Bulou for helpful discussions. This work was supported by the French Ministry of Education and Research, the CNRS, and Region Pays de la Loire (CPER Femtosecond Spectroscopy equipment program). R. Rapacz is supported by the FORSZT project co-funded by EU from the European Social Fund.

-
- [1] J. E. Moore, *Nature* **464**, 194 (2010).
- [2] M. Hajlaoui, E. Papalazarou, J. Mauchain, G. Lantz, N. Moisan, D. Boschetto, Z. Jiang, I. Miotkowski, Y. P. Chen, A. Taleb-Ibrahimi, L. Perfetti, and M. Marsi, *Nano Lett.* **12**, 3532 (2012).
- [3] Y. Zhang, K. He, C.-Z. Chang, C.-L. Song, L.-L. Wang, X. Chen, J.-F. Jia, Z. Fang, X. Dai, W.-Y. Shan, S.-Q. Shen, Q. Niu, X.-L. Qi, S.-C. Zhang, X.-C. Ma, and Q.-K. Xue, *Nature Phys.* **6**, 584 (2010).
- [4] M. V. Costache, I. Neumann, J. F. Sierra, V. Marinova, M. M. Gospodinov, S. Roche, and S. O. Valenzuela, *Phys. Rev. Lett.* **112**, 086601 (2014).
- [5] D. Kim, Q. Li, P. Syers, N. P. Butch, J. Paglione, S. D. Sarma, and M. S. Fuhrer, *Phys. Rev. Lett.* **109**, 166801 (2012).
- [6] A. A. Reijnders, Y. Tian, L. J. Sandilands, G. Pohl, I. D. Kivlichan, S. Y. Frank Zhao, S. Jia, M. E. Charles, R. J. Cava, N. Alidoust, S. Xu, M. Neupane, M. Z. Hasan, X. Wang, S. W. Cheong, and K. S. Burch, *Phys. Rev. B* **89**, 075138 (2014).
- [7] H. Steinberg, D. R. Gardner, Y. S. Lee, and P. Jarillo-Herrero, *Nano Lett.* **10**, 5032 (2010).
- [8] M. Eddrief, P. Atkinson, V. Etgens, and B. Jusserand, *Nanotechnology* **25**, 245701 (2014).
- [9] J. Flock, T. Dekorsy, and O. V. Misochko, *Appl. Phys. Lett.* **105**, 011902 (2014).
- [10] K. Saha and I. Garate, *Phys. Rev. B* **89**, 205103 (2014).
- [11] N. Kamaraju, S. Kumar, and A. K. Sood, *Eur. Phys. Lett.* **92**, 47007 (2010).
- [12] K. Norimatsu, J. Hu, A. Goto, K. Igarashi, T. Sasagawa, and K. G. Nakamura, *Sol. State Commun.* **157**, 58 (2013).
- [13] N. Kumar *et al.*, *Phys. Rev. B* **83**, 235306 (2011).
- [14] Y. Wang, L. Guo, X. Xu, J. Pierce, and R. Venkatasubramanian, *Phys. Rev. B* **88**, 064307 (2013).
- [15] R. Rapacz, K. Balin, A. Nowak, and J. Szade, *J. Cryst. Growth* **401**, 567 (2014).
- [16] J.-W. G. Bos, F. Faucheux, R. A. Downie, and A. Marcinkova, *J. Sol. State Chem.* **193**, 13 (2012).
- [17] D. L. Greenaway and G. Harbere, *J. Phys. Chem. Solids* **26**, 1585 (1965).
- [18] P. Yu and M. Cardona, *Fundamentals of Semiconductors* (Springer-Verlag, Heidelberg, 1996).
- [19] R. Merlin, *Solid State Commun.* **102**, 207 (1997).
- [20] M. Lejman, G. Vaudel, I. C. Infante, P. Gemeiner, V. E. Gusev, B. Dkhil, and P. Ruello, *Nature Commun.* **5**, 4301 (2014).
- [21] A. Ayouch, X. Dieudonne, G. Vaudel, H. Piombini, K. Valle, V. Gusev, P. Belleville, and P. Ruello, *ACS Nano* **6**, 10614 (2012).
- [22] H. J. Zeiger, J. Vidal, T. K. Cheng, E. P. Ippen, G. Dresselhaus, and M. S. Dresselhaus, *Phys. Rev. B* **45**, 768 (1992).
- [23] S. Y. F. Zhao, C. Beekman, L. J. Sandilands, J. E. J. Bashucky, D. Kwok, N. Lee, A. D. LaForge, S. W. Cheong, and K. S. Burch, *Appl. Phys. Lett.* **98**, 141911 (2011).
- [24] C. B. Satterthwaite and R. W. Ure Jr., *Phys. Rev.* **108**, 1164 (1957).
- [25] B.-L. Huang and M. Kaviani, *Phys. Rev. B* **77**, 125209 (2008).
- [26] T. Garl, E. G. Gamaly, D. Boschetto, A. V. Rode, B. Luther-Davies, and A. Rousse, *Phys. Rev. B* **78**, 134302 (2008).
- [27] C. Mechri, P. Ruello, and V. Gusev, *New. J. Phys.* **14**, 023048 (2012).
- [28] V. Juve, A. Crut, P. Maioli, M. Pellarin, M. Broyer, N. Del Fatti, and F. Vallée, *Nano Lett.* **5**, 1853 (2010).
- [29] Y. Wang, C. Liebig, X. Xu, and R. Venkatasubramanian, *Appl. Phys. Lett.* **97**, 083103 (2010).
- [30] D. J. Cebula *et al.*, *Clays Min.* **17**, 195 (1987).
- [31] D. E. Aspnes and A. A. Studna, *Phys. Rev. B* **27**, 985 (1983).
- [32] A. I. Bailey and S. M. Kay, *Br. J. Appl. Phys.* **16**, 39 (1965).
- [33] Y. Wang, B. Qiu, A. J. H. McGaughey, X. Ruan, and X. Xu, *J. Heat Trans.* **135**, 091102 (2013).
- [34] J. R. Wiese and L. Muldrew, *J. Phys. Chem. Solids* **15**, 13 (1960).
- [35] C. Thomsen, H. T. Grahn, H. J. Maris, and J. Tauc, *Phys. Rev. B* **34**, 4129 (1986).
- [36] M. H. Francombe, *Br. J. Appl. Phys.* **9**, 415 (1958).
- [37] L. Xue-Dong and Y.-H. Park, *Mat. Trans.* **43**, 681 (2002).
- [38] P. Ruello, S. Zhang, P. Laffez, B. Perrin, and V. Gusev, *Phys. Rev. B* **79**, 094303 (2009).
- [39] J. A. Sobota, S.-L. Yang, D. Leuenberger, A. F. Kemper, J. G. Analytis, I. R. Fisher, P. S. Kirchmann, T. P. Devereaux, and Z.-X. Shen, *Phys. Rev. Lett.* **113**, 157401 (2014).

SCIENTIFIC REPORTS

OPEN Quantum size effect on charges and phonons ultrafast dynamics in atomically controlled nanolayers of topological insulators Bi_2Te_3

Received: 3 May 2017

Accepted: 11 September 2017

Published online: 23 October 2017

M. Weis^{1,2}, B. Wilk^{1,2}, G. Vaudel², K. Balin¹, R. Rapacz¹, A. Bulou², B. Arnaud², J. Szade¹ & P. Ruello²

Heralded as one of the key elements for next generation spintronics devices, topological insulators (TIs) are now step by step envisioned as nanodevices like charge-to-spin current conversion or as Dirac fermions based nanometer Schottky diode for example. However, reduced to few nanometers, TI layers exhibit a profound modification of the electronic structure and the consequence of this quantum size effect on the fundamental carriers and phonons ultrafast dynamics has been poorly investigated so far. Here, thanks to a complete study of a set of high quality molecular beam epitaxy grown nanolayers, we report the existence of a critical thickness of around ~6 nm, below which a spectacular reduction of the carrier relaxation time by a factor of ten is found in comparison to bulk Bi_2Te_3 . In addition, we also evidence an A_{1g} optical phonon mode softening together with the appearance of a thickness dependence of the photoinduced coherent acoustic phonons signals. This drastic evolution of the carriers and phonons dynamics might be due an important electron-phonon coupling evolution due to the quantum confinement. These properties have to be taken into account for future TIs-based spintronic devices.

Topological Insulators (TIs) provide new perspectives for next generation spintronics devices thanks to a natural spin polarized surface current that is topologically protected^{1,2}. After an intense effort to develop a comprehensive understanding of the bulk properties^{1,2}, the age of the investigation of integration of TIs at nanoscale is heralded by now³. Among exciting perspectives for nano-spintronics, TIs can be used for charge-to-spin current conversion³ or Dirac fermions based nanometer Schottky diode⁴. However, as known in quantum wells, dots or nanocrystals^{5,6} or in metallic nanostructures⁷⁻⁹, the downscaling usually leads to apparition of size dependent properties and an enhancement of the quantum confinement effect. In the case of TIs films, it has been reported that the electronic properties are deeply affected indeed under a reduction of the layer thickness where the electronic structure deviates from the bulk one with the lost of surface Dirac states properties^{10,11}. A gap opening in the surface Dirac states appears as well as a profound modification of the bulk electronic levels (conduction-CB and valence-VB bands). This phenomenon revealed by Angle-Resolved Photoemission Spectroscopy (ARPES), appears around below 4 nm in Bi_2Se_3 (BS) compound^{10,11} and 3–4 nm in Bi_2Te_3 ¹². A sketch of the thickness dependence electronic structure is shown in Fig. 1a¹². Different mechanisms have been discussed to elucidate this phenomenon, including substrate-mediated Rashba effect¹⁰ and the existence of a crossover from a 3D to a 2D topological insulator¹³. The band gap opening has been reproduced theoretically and it has been reported that additional quantum size effects should appear leading to topological quantum phase transitions that depend on the film thickness¹⁴⁻¹⁶. While this drastic evolution of the electronic structure submitted to a strong confinement has been well described in TIs at the thermodynamic equilibrium with photoemission spectroscopy¹⁰⁻¹² and with transport properties measurements^{17,18}, the consequence of this confinement on the ultrafast dynamics of carriers and phonons has been debated only recently in BS^{19,20}. The ultrafast dynamics of carriers and phonons are only well characterized in bulk crystals of TIs with either time-resolved ARPES or optical methods²¹⁻²⁶. Moreover,

¹A. Chelkowski Institute of Physics and Silesian Center for Education and Interdisciplinary Research, 75 Pulku Piechoty 1A University of Silesia, 41–500, Chorzów, Poland. ²Institut des Molécules et Matériaux du Mans, UMR CNRS 6283, Université du Maine, 72085 Le Mans, France. Correspondence and requests for materials should be addressed to J.S. (email: jacek.szade@us.edu.pl) or P.R. (email: pascal.ruello@univ-lemans.fr)

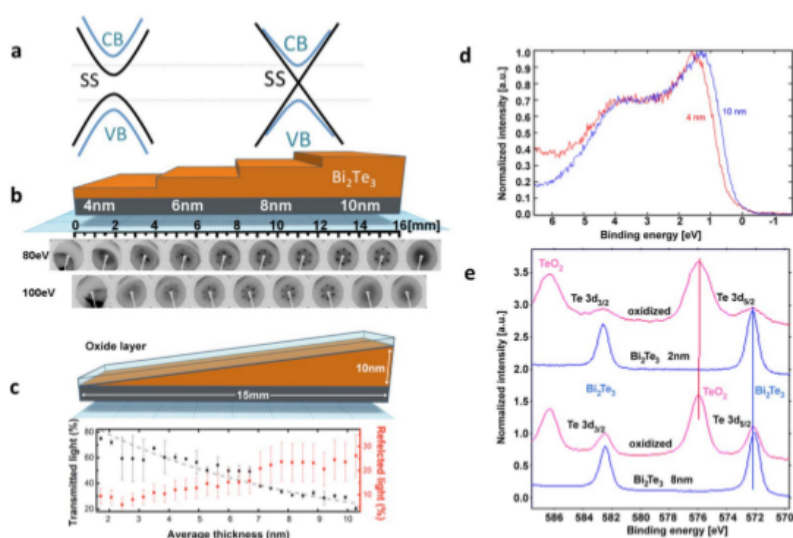


Figure 1. Electronic structure characterization of ultrathin Bi_2Te_3 layers with thickness gradient. (a) Sketch of the thickness dependence of the bulk and surface electronic states in Bi_2Te_3 ¹². CB, VB and SS mean conduction and valence bands and surface states respectively. (b) Art view of the cross section of the step sample 1 with as inset in the bottom of the figure the thickness dependence of the LEED image obtained for two energies. These images confirm the six-fold symmetry of the z-grown BT layers. (c) Art view of the cross-section of the wedge sample together with the continuous wavelength optical transmission (dashed curve is the calculated optical transmission following the Beer-Lambert law, see Methods) and reflectivity along the thickness gradient. (d) Valence X-ray photoemission spectra of BT films for variable thicknesses obtained *in-situ* (vacuum) for step sample 2. (e) Examples of XPS spectra of the step sample 1 for two thicknesses (8 and 2 nm) obtained for as-grown BT layer (blue curves) and after passivation with oxide cap layer (red curves).

while a theoretical prediction of the enhancement of the coupling between the surface electrons and the acoustic phonons has been reported for a confined structure²⁷, no direct experimental reports confirm these predictions so far while ultrafast optics can provide new insights.

In this article, we study the confinement effect on the electronic structure as well as on the ultrafast dynamics of carriers and phonons. We first confirm the appearance of the evolution of the electronic structure for very thin layers with X-ray Photoemission Spectroscopy (XPS) in accordance with what was observed in BS^{10,11} and BT¹² compounds. Secondly, thanks to femtosecond optical pump-probe methods, we reveal several anomalies on the carriers and coherent phonons ultrafast dynamics in Bi_2Te_3 (BT) when the layers thickness is typically smaller than the critical value of ~ 6 nm. We report indeed a dramatic modification of the hot carriers relaxation time with a reduction from around 2.2 ps (bulk) down to around 200 fs for layer as thin as 4 nm. This transition appears somehow universal since it has been observed for two different samples exhibiting both thickness gradient but having been grown according either to a step or wedge geometry. In parallel to the electron-phonon relaxation time determination, we also report a modification in the spectrum of the photoinduced phonons in the confined nanostructures. While for so-called thick BT layers, the optical phonon mode A1g is clearly generated and detected as expected from bulk behavior, a clear softening and a decrease of its lifetime are observed for ultrathin layers. Surprisingly, while the A1g phonon signal vanishes for ultrathin layers, an increasing contribution of coherent acoustic phonons signal appears with a clear resonant effect. These carriers and phonons dynamics size dependence suggests the existence of a transition in the mechanism of the electron-phonon coupling when reducing the TIs layer which has to be taken into account in the perspectives of the development of TIs nanodevices.

Results

Electronic structure of ultrathin BT layers. The investigations were carried out with single crystalline Bi_2Te_3 (BT) ultrathin films having thickness varying from around 2 nm up to 10 nm and grown with molecular beam epitaxy with PREVAC system²⁸. Different samples were grown with a step or a wedge geometry as shown in Fig. 1b,c (see Methods). Low Energy Electron Diffraction (LEED) image was realized for the step sample (step sample 1) as a function of the BT layer thickness (Fig. 1b confirms the films grow along the c-axis having a six-fold symmetry). Additional LEED analysis are shown in the Supplementary Figures 1–2 of Supplementary Note 1. A wedge sample was also grown and a continuous wavelength optical transmission experiment (bottom of Fig. 1c) was carried out to confirm the thickness gradient of the wedge sample (see Methods). *In-situ* XPS measurements

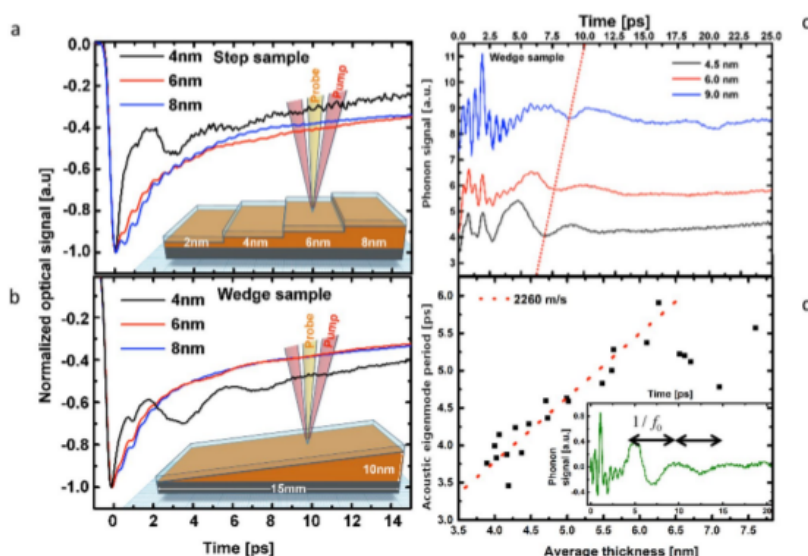


Figure 2. Ultrafast optical response of ultrathin layers of Bi_2Te_3 . Time-resolved optical reflectivity obtained for various layers of BT for the step (a) or the wedge (b) sample. The signals are normalized to the maximum of electronic peak. (insets) The pump and probe are represented in the artist view as red and orange beams. (c) Contributions of the phonons signals to the transient reflectivity signals for three different thickness. (d) Thickness dependence of the longitudinal acoustic resonance eigenmode period $1/f_0$. The slope of the red dashed line provides the estimates of the longitudinal sound velocity (2260 m/s) of BT. Inset shows an example of the typical longitudinal acoustic signal with the period $1/f_0$ for a BT layer thickness of 6 nm.

(Fig. 1d) performed on step sample 2 within two regions of 4 and 10 nm of thickness confirms that the electronic structure evolves for ultrathin layer in agreement with the literature^{10–12}. The general structure of the valence band is in agreement with the previous experimental results and calculations of total DOS (density of states) for the thick layer (10 nm)²⁵. However, a clear difference is visible at the valence band offset where the lowering of the top of valence band by about 0.2 eV with respect to the thicker films is detected for the 4 nm thick film. At the same time the intensity in the vicinity of the Fermi level is unchanged. This is related with the position of the Fermi level which is crossing the bottom of the bulk conduction band. This indicates a n-type doping for our BT films. Regarding the core-levels XPS data (realized on step sample 1 and shown in Fig. 1e), the analysis of the Bi and Te most prominent photoemission lines show one chemical state characteristic for Bi_2Te_3 ²⁸ (more complete description of XPS analysis is given in the SI). In Fig. 1e we show the Te $3d_{5/2}$ line for the as grown film and after the oxidation in air (Bi lines are shown in the Supplementary Figures 3–5 in the Supplementary Note 1). The native and optically transparent oxides layer is formed by TeO_2 and Bi_2O_3 which stabilizes the surface. An angle dependent XPS investigation taking into account the variation of the various components intensity and electron inelastic mean free path have shown that the oxides are on the surface and have a typical thickness of ~2 nm (see SI)²⁹. It is important to underline that under surface passivation by the oxides, the core levels (Bi and Te lines) characteristic to BT TIs remain unchanged confirming the stability of the bulk properties of the layer over several months. We are aware that the passivation may affect the surface states^{30,31} since they are very sensitive to a small amount of extrinsic surface defects and are submitted to a rapid aging (few minutes) even in high vacuum. However, we did not observe any changes in the *in-situ* obtained XPS spectra within several minutes and hours after deposition. Consistently with our XPS analysis, we will see in Figs 1 and 2, the ultrafast light-excitation of the A1g Raman active mode of BT films confirming the right structure is obtained. Moreover, the analysis of the evolution in time of the light-excited acoustic phonons (Supplementary Figure 1 in Supplementary Note 1) permits to confirm that the oxide layer is stable in time in agreement with XPS analysis.

Ultrafast carriers and phonons dynamics. Some typical time-resolved and thickness dependent optical reflectivity signals are given in Figs. 1a,b for the step sample 1 and the wedge sample respectively. The signals are composed first of a sharp variation of the transient optical reflectivity consecutively to the electronic excitation. Then the decay of the signals is evidenced with, as superimposed, some oscillatory components due to the photo-excitation of phonons (Fig. 1c) that we will discuss latter on. The electronic and the phonons contributions to the transient optical reflectivity were separated as $\Delta R/R = \Delta R/R_{\text{electron}} + \Delta R/R_{\text{phonons}}$, where the electronic contribution is composed of a fast rising signal due to the carriers excitation induced by the pump beam followed by a

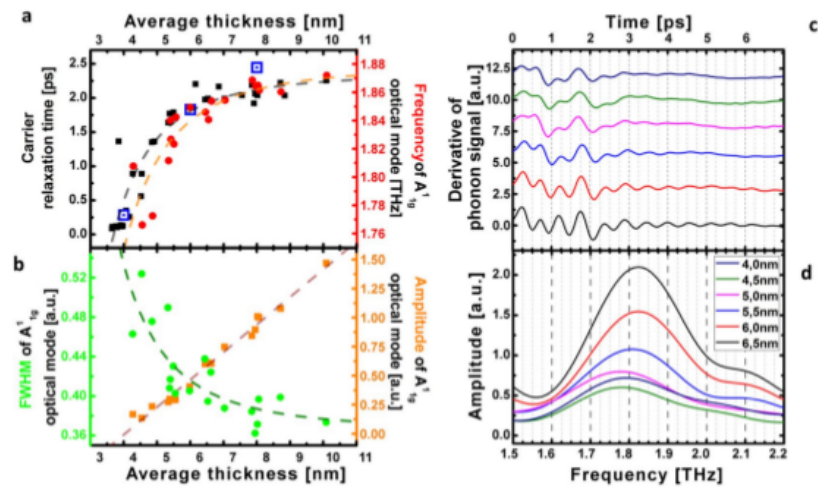


Figure 3. Thickness dependence of the ultrafast carrier and phonon dynamics. (a) Thickness dependence of the electron-phonon relaxation time for the wedge (black squares) and step (centred blue squares) samples. Thickness dependence of the A1g optical phonon frequency (red dots). (b) Thickness dependence of the A1g optical phonon amplitude (gold squares) and FWHM (green dots) (c) Typical oscillatory component at short time scale revealing the A1g optical phonon. (d) Fast Fourier Transform (FFT) of signal shown in (c) revealing the A1g mode softening for ultrathin layer.

decay described by two exponential functions with a fast decay time ranging from 200 fs to 2 ps (depending on the layer thickness) and a slower component with a time ranging from 30 to 60 ps associated to long living carriers and thermal relaxation process (see Supplementary Note 2 and Supplementary Figure 7 for a detailed example of the fitting procedure). Whatever the step or wedge sample, the first striking evidence we report, is a huge modification of the carrier relaxation time and phonons dynamics (Figs 1–4) for topological insulator films having a very small thickness (typically <6 nm). Moreover, we observed similar behavior when performing the optical transmission measurements ($\Delta T/T$) as shown in the Supplementary Figure 8 indicating the response is really intrinsic to the BT layer. For thick BT layers, the characteristic time of around 2.2 ps is similar to the relaxation of hot carriers (electron and hole) probed in the visible range for bulk Bi_2Se_3 ^{21,22} and bulk Bi_2Te_3 ²⁶, while for most confined BT layers, the carrier relaxation time drastically diminishes down to around 200 fs (Fig. 2a). This indicates that the scattering process is close to ten times stronger in the confined BT. We also notice that we were not able to get a clear signal for the thinnest BT layer (2 nm) of the step sample 1. The oscillatory components obtained for thick BT films reveal clearly the A1g mode at 1.86 THz in accordance with the literature^{33–36} (Fig. 2c). An additional modulation of the signal, well visible for the 4.5 nm layer in Fig. 2c (time range 0–2.5 ps), which does not depend on the sample thickness is assigned to the vibration of the top oxide layer (2 nm). While scrutinizing the time-domain optical phonon signals, we evidence a slight optical phonon A1g softening (Fig. 2a,c,d) as well as a decrease of the lifetime (Fig. 2b), confirming that a modification of the interatomic potentials might occur for most confined layers. This softening (~4%) and damping enhancement is consistent with the observations made in Raman scattering measurements where the incoherent A1g phonon exhibits such softening in Bi_2Se_3 ^{20,37,38} and in Bi_2Te_3 ³⁹. The fact that this A1g softening occurs both with phonons that are photoexcited with a laser pulse or with thermally excited phonons (Raman spectroscopy) indicates that the softening does not come from hot electrons-driven potential softening as known for bismuth crystal^{40,41}. A detailed description of our pump power dependence of the A1g mode is shown in Supplementary Figure 9. As a last observation, our experimental results evidence the appearance of a larger coherent acoustic phonons signal when the layer becomes thin enough (Figs 1c and 2a,b). The spectral analysis of this acoustic phonon signal reveals that the main oscillatory part we observed comes from the excitation/detection of the first acoustic eigenmode of the thin film with $f_0 = V/2L$, where V is the sound velocity of the BT layer. The analysis of the eigenmode frequency scales indeed with the inverse of the thickness (Fig. 1d) without any clear anomaly on the sound velocity we estimate at around 2260 m.s⁻¹. However a resonant-like effect is observed in the thickness dependence of the coherent acoustic phonons amplitude as depicted in Fig. 4. The coherent acoustic phonon amplitude (first eigenmode amplitude) clearly increases from 10 to 5 nm while below 5 nm a new regime appears. It is worth to mention that this critical value of 5 nm corresponds quite well to the characteristic thickness below which the carrier relaxation time suddenly falls down (Fig. 2a). As a summary, this set of physical parameters measurements provide a new insight on the ultrafast dynamics of carriers and phonons while submitting the BT compound to a strong confinement. In the next section we discuss the possible fundamental physical origins of these phenomena never reported in TIs BT up to now.

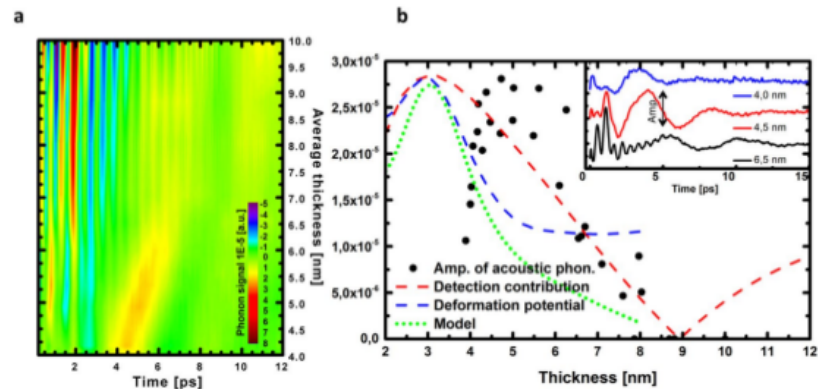


Figure 4. Coherent acoustic phonon generation and detection. (a) Map of the optical and acoustic phonon mode amplitudes (fixed pump power) versus time and along the thickness gradient revealing the appearance of larger acoustic phonon signals for ultrathin layers. (b) Thickness dependence of the amplitude of the photodetected coherent acoustic signal. A model (green curve) taking into account the detection process and an estimated size dependent electron-hole acoustic deformation potential from the literature¹⁰ provides a semi-quantitative explanation of the experimental observations.

Discussion

Carrier relaxation dynamics. The thickness (L) dependence of the electronic levels (ΔE) is known in quantum wells and is expected to follow the $\Delta E = A/L^2$ ⁴². This leads in general to size dependent carrier relaxation time with different power of law due to complex dynamics⁶. Reduction of the relaxation time has been reported several time in the literature like in the case of CdSe or CdS nanocrystals⁵ where it is reduced by a factor of 3 (from 270 fs to 85 fs) when the nanocrystal diameter is reduced from 4 nm to 2 nm. Similar decrease of the carrier lifetime τ_{e-ph} was also observed when reducing the diameter of metallic nanoparticles to few nanometers²⁴. In our case, a numerical adjustment leads to the phenomenological thickness dependent relaxation time as:

$$\tau_{e-ph} = \tau_{e-ph}^0 - B/L^\alpha \quad (1)$$

with $\alpha = 2.6$ and $\tau_{e-ph}^0 = 2.2$ ps (see dashed red curves in Fig. 2(a) and Supplementary Figure 7). Similar power of law applies well for describing the evolution of the A1g optical mode frequency (ν_{A1g}) and its width $\Delta\nu_{A1g}$ as if a common physical mechanism correlates these parameters. It is important to remind that TIs nanolayers are confined only in one direction while nanocrystals are 3D quantum-confined systems. We know that the electron-hole relaxation time depends both on the matrix element (deformation potential term in the Hamiltonian⁴⁰) and on the final density of states according to the Golden Fermi rule, but the quantitative relationship between this experimental law and the size dependent electronic structure is not an easy task since a complete electronic and phonon dispersion curves are required for bulk and surface states. No complete theoretical formulation of the size dependence relaxation time of the photoexcited population in CdSe and CdS was reported so far due to the same complexity⁵. Different possible contributions can be proposed. When the size of the system is reduced, the carriers surface trapping is known to be more efficient since the probability per unit of time for an electron to reach the surface increase as soon as the mean free path of electrons is comparable with the size of the object. This has been already discussed in the case of semiconductor nanostructures⁵. This surface recombination was one channel of relaxation in semiconductor nanocrystals but quantum size effect on the electron-phonon coupling was also evoked⁵. In the case of metallic nanoparticles, the proposed interpretation was based on the reduction of electron-ion screening interaction due to a decrease of the carrier density close to the surface which contains a non-negligible number of atoms compared to volume ones for few nm nanoparticles radius R ^{7,8}. A phenomenological scattering rate equation was proposed with $1/\tau_{e-ph} = 1/\tau_0 + V_F/\alpha R$, where τ_0 , α and V_F are the bulk e-ph relaxation time, an adjustable coefficient and the Fermi velocity⁹. In the case of BS thin films, a decrease of the relaxation time driven by a size dependent Fröhlich interaction was proposed¹⁹ but many other mechanisms can contribute. In the case of BT nanolayers, we can of course think about possible trapping at the oxide cap layer/BT layer interface which could increase the hot carrier damping, even if it is difficult at that stage to evaluate this contribution. Furthermore, it has been also shown that the range of the bulk-surface interband scattering channel has been estimated to occur up to 5 nm in BT compounds²⁴, which matches well the critical thickness we estimate and could indicate that the anomaly we observe is a crossover from the 3D to the 2D system. This is supported by the fact that it is known that the coupling between surfaces Dirac fermions wavefunctions of two opposite sides of a thin layer has been reported to occur over few nm for BS, and even detectable in film of 10 nm of thickness¹⁸. Moreover, additional effect could be possible such as band bending. It was previously observed at the free surface

of a bulk crystal⁴ which means that such situation can be enhanced in ultrathin layers of BT with the closeness of the two opposite surfaces. As a consequence, the hybridization of two opposite surfaces states, the surface band bending, the modification of the bulk electronic levels (see Fig. 1d) as well as the A1g optical phonon softening that we report, are all physical parameters that obviously must correspond to a modification of the electron-ion interaction, i.e the deformation potential parameter, which might influence the carrier relaxation time. The question is why there is an enhancement of the relaxation under the confinement? Beside the surface trapping effect, our observation of an important enhancement of the coherent acoustic phonon signals (Fig. 4a) could be a signature of an enhancement of the electron-hole acoustic phonon deformation potential coupling, which could also contribute to the hot carrier damping rate in the case of electron/acoustic phonon collision processes. This electron-hole acoustic phonon deformation potential is also the driving parameter for the photoexcitation process of coherent acoustic phonon²³; as a matter of fact, discussing the thickness dependence of the coherent acoustic phonon signal may provide new insight on this electron-phonon coupling strength as presented in the following.

Electron-hole acoustic phonon deformation potential. The electron-hole acoustic phonon deformation potential is expected to be thickness dependence in topological insulators ultrathin films since the energy bands evolve quite a lot as we observed (Fig. 1c) and accordingly to the literature refs^{10,12}. The question is how much this deformation potential varies as a function of the thickness. If we consider that the hot electrons (holes) rapidly thermalize down (up) to the conduction (valence) bands, the relevant deformation parameter is the one close to the band gap (E_g) with:⁴⁴⁻⁴⁷

$$d_{33}^{ac-eh} = \frac{\partial E_g}{\partial \eta_{33}} \tag{2}$$

This approximation is justified as soon as the frequency of the detected coherent acoustic phonons is smaller than the inverse of the time of thermalization in the conduction and valence bands respectively with^{44,46,47}. As mentioned above in the description of our results, the coherent acoustic phonons under discussion are those corresponding to the thin film eigenmodes, i.e. those inducing an out-of-plane strain η_{33} . The forth and back bouncing coherent acoustic phonons modulate the entire thickness L so that the relevant strain associated to the deformation potential is $\eta_{33} = dL/L$. Consequently the relevant deformation potential becomes:

$$d_{33}^{ac-eh} = L \frac{\partial E_g}{\partial L} \tag{3}$$

We have access to the thickness dependence of the band gap in the literature with different precisions for BS and BT compounds^{10,12}. As a first element of discussion, we have estimated the experimental parameter $L \frac{\partial E_g}{\partial L}$ in BS compound based on experimental data¹⁰ (we used so-called CB1 and VB1 values of ref.³⁰, to evaluate the band gap E_g). The thickness dependence is shown (blue dashed curve) in Fig. 3b where we clearly see the enhancement of the deformation potential parameter when reducing the thickness as expected. For the purpose of the comparison we normalize this parameter to the maximum of the experimental amplitude. We are aware that BS and BT are not identical, but this approach shows that an enhancement of the photo induced coherent acoustic phonon could explain partially the experimental observation. There is however a clear deviation for ultrathin layer where the calculated deformation potential cannot explain the sudden decrease of the experimental phonon amplitude. We believe that this effect comes from a detection process that can be numerically estimated as described below. We have realized a calculation of the contribution of coherent acoustic phonons to the transient optical reflectivity (detection process) by considering that none of the physical parameters change but only the thickness is reduced. To do that we have calculated the coherent acoustic phonon contribution to the transient optical reflectivity following the standard method⁴⁸⁻⁵⁰. We have performed this calculation by considering the first acoustic eigenmode (f_0) strain field contribution whose standard expression is $\eta_{33}(z, t) = A \times \sin[\frac{\pi z}{L}]e^{i\omega_0 t}$ where A is the amplitude and $\omega_0 = 2\pi f_0$. We can show (see details in Supplementary Note 2) that this contribution to the transient optical reflectivity is given by⁴⁸⁻⁵⁰:

$$\begin{aligned} \left(\frac{\Delta R}{2R}\right)_{ac-ph} &\approx Re[-4i \times C \times r_{12}k_1 \frac{L}{\pi} e^{i\omega_0 t} \\ &- iC \frac{\partial k_1}{\partial \eta_{33}} \int_0^L A \times \sin\left[\frac{\pi z}{L}\right] e^{i\omega_0 t} [r_{12}e^{-ik_1(L-z)} \\ &+ e^{ik_1(L-z)}]^2 dz] \end{aligned} \tag{4}$$

where Re corresponds to the real part of the formula. C is an optical parameter that depends on the optical properties of the BT layer and on those of the mica substrate and the details are given in the Supplementary Note 2. The subscripts 1 and 2 define the BT and mica medium and r_{12} is the optical reflectivity coefficient at the interface BT/mica. k_1 is the probe wavevector in the BT medium. The first term in the formula is the contribution of the interferometric effect due to the thickness change induced by the coherent acoustic phonon strain field and the second term corresponds to the photoelastic contribution, i.e. that due to the modulation of the refractive index by the coherent acoustic phonons strain field. This strain field is coupled to the internal probe light electric field given as the second term (into the brackets) in the integral term. We remind that $z=0$ corresponds to the free surface of BT layer (we have neglected the contribution of the passivation oxide layer at this level). $\frac{\partial k_1}{\partial \eta_{33}}$ is the photoelastic coefficient.

cient. We can derive the latter one according to $k_0 \frac{\partial n_1}{\partial \eta_{33}} = k_0 \frac{\partial n_1}{\partial E_{\text{probe}}} \times \frac{\partial E_{\text{probe}}}{\partial \eta_{33}} = k_0 \frac{\partial(n'_1 + in''_1)}{\partial E_{\text{probe}}} \times \frac{\partial E_{\text{probe}}}{\partial \eta_{33}}$, where k_0 and $\frac{\partial E_{\text{probe}}}{\partial \eta_{33}}$ are the optical wavevector in vacuum and the deformation potential coefficient at the probe energy E_{probe} and $n_1 = n'_1 + in''_1$ is the BT refractive index ($n_1 = 1.7 + i4.5$ at the probe energy³³). From the literature³³ one can extract both the real and the imaginary part of the derivative of the refractive index at the probe energy (2.2 eV) and we found that $\frac{\partial n'_1}{\partial E_{\text{probe}}} / \frac{\partial n''_1}{\partial E_{\text{probe}}} \sim 1.5$. The refractive index of Mica was taken as $n_2 = 1.6$. The result of the calculation gives a time-dependent sinusoidal function for transient optical reflectivity signal with the corresponding frequency of the eigenmode. We focus on the thickness dependence of the magnitude of this signal. This maximum amplitude is not the absolute one, since A as well as $\frac{\partial E_{\text{probe}}}{\partial \eta_{33}}$ (deformation potential at the probe energy) are not known. But, importantly, we can discuss the thickness L dependence at least. Considering that the sound velocity of the BT layers does not change (see Fig. 1d), we can say that A is proportional to the electron-hole acoustic deformation potential ($d_{\text{ac-ph}}$) and the photoexcited carriers concentration N only as:⁴⁵⁻⁴⁷

$$\eta_{33}(z, t) = A \times \sin\left[\frac{\pi z}{L}\right] e^{i\omega t} \propto N(L) \times d_{33}^{\text{ac-ph}} \times \sin\left[\frac{\pi z}{L}\right] e^{i\omega t} \quad (5)$$

As shown in Fig. 1c, the Beer-Lambert approach appears reasonable which shows that the optical properties do not drastically change at the probe energy. We can then estimate how N varies versus the layer thickness L and show that N is roughly multiplied by two in a layer of 4 nm compared to a 10 nm thick one. We have taken this into consideration in the calculation.

The calculated thickness dependence of the maximum of amplitude of the detected eigenmode is shown in Fig. 4b (red dashed curve). A comparison is given with the experimental amplitude (black dots) of the maximum of the eigenmode oscillation (see comparison of some signals in the inset of Fig. 4b). As mentioned before, we cannot compare the absolute values, but only L variations; as matter of fact we have normalized the curve to their maximum for discussing the tendency. It appears that the detection mechanism reproduce an enhancement of the detection of the coherent acoustic phonons as well as a decrease of the detected signal for ultrathin layers. If now we include in this calculation the thickness dependence of the deformation potential, we obtain the green curve (curve labelled as model). Some similitude in the thickness dependence appears but there is a clear shift between theory and experiments that might comes from the approximations we did. Among them, we have used the $L \frac{\partial E_g}{\partial L}$ parameter of BS due to the lack of enough precise data for BT. Moreover, we considered the photoelastic coefficient as thickness independent which is very likely not true.

At this level we do not claim that we have definitive conclusion but we have to admit that the comparison between experiments and the theoretical calculation, supports a quantum size effect on the electron-hole acoustic phonon deformation potential as never reported before. As an intermediate important conclusion, this model could establish a possible partial correlation between the size dependent electron-hole acoustic phonon deformation potential and the observation of the increase of the carrier relaxation rate, in the case of predominant scattering of carriers by the acoustic phonons. As discussed above, surface trapping also play probably a role. Moreover, it is worth to underline that our model (Eq. 3) is related only to bulk electronic level and does not take into account the electron-hole acoustic phonon coupling with surface states. Recent theoretical consideration done by Giraud *et al.*²⁷, have shown that the quantum size effect leads also to an enhancement of the Dirac surface electron-acoustic phonon coupling which shows that both approaches go in the same direction suggesting an enhancement of coherent acoustic phonon generation in quantum-confined BT layer. This size dependence of the electron-hole acoustic phonon deformation potential parameter needs to be confirmed with ab-initio calculations.

As a conclusion, this work reveals a clear modification of the out-of-equilibrium carriers and phonons dynamics when the BT layer is reduced to few nanometers. This time-domain investigation provides a new insight in the size-dependent physical properties of topological insulators while size-dependent electronic properties were probed in the past only at the thermodynamic equilibrium. While known for semiconductor and metallic nanostructures up to now, we report a similar drastic decrease of the electron-phonon relaxation time with an increase of the confinement. We can assign this effect to a size-dependent electron-hole phonon deformation potential parameter which need to be confirmed by ab-initio calculation. In particular, the increase of the coherent acoustic phonons signals with decreasing L can be explained at least partially by an enhancement of the electron-hole acoustic deformation potential parameter according to our theoretical proposition. The experimental optical measurement integrates bulk and surface electrons, but non negligible surface carriers contribution could exist since our film thickness scales with the required characteristic distance for surface Dirac fermions states to hybridize¹⁸, but it is difficult to give a quantitative estimate by now of separated contributions. Apart this quantum-confinement effect, one cannot exclude the contribution of the carrier surface recombination that could enhance the carrier relaxation as well. All these new physical insights show that downscaling the topological insulators properties is not straightforward and these new experimental reports have to be taken into account for potential TIs based spintronic nanodevices.

Methods

Sample Preparation. The growth of ultrathin BT layers was performed in the co-deposition mode. The electronic and crystallographic characterizations were carried out *in-situ* with the use of XPS (Fig. 1d) and the low energy electron diffraction (LEED) (Fig. 1b). The samples were deposited on the (110) freshly cleaved Muscovite mica substrate (Ted Pella, Inc.), in the MBE chamber with mechanical shutter to realize the step and wedge geometries and to control the thickness gradient. Deposition rate was controlled with quartz crystal micro balance,

which permits to estimate the thickness with accuracy of $\pm 0.2\text{nm}$. Stoichiometry analysis was done by XPS analysis and details are given in the SI. Static optical transmission (T) measurements were done on the wedge sample to evidence the gradient of the thickness (Fig. 1(c)). From the thickness of 10 nm down to around 2 nm, the optical transmission increases following well the Beer-Lambert law $I_T = I_0 e^{-L/\xi}$, with $\xi = 10\text{ nm}$ at an optical wavelength of 582 nm³², and I_0 is the transmitted intensity with only the mica substrate. In the very thin regions of the wedge sample (less than 4 nm) some deviations are observed probably due to the electronic properties changes as revealed by XPS (Fig. 1d).

Time-resolved optical measurements. The pump-probe technique used here is based on a 80 MHz repetition rate Ti:sapphire femtosecond laser (120 fs). The pump wavelength is fixed at the harmonic of the Ti:sapphire laser (830 nm, 1.495 eV) while the probe beam is introduced in a synchronously pumped OPO to tune the wavelength to 582 nm (2.13 eV). The experiments were conducted with the front-front configuration with incident pump and probe beams perpendicular to the surface as shown in Fig. 1 but also in transmission geometry (not shown) since mica substrate is transparent to both pump and probe. Pump-probe experiments were conducted with the wedge sample (passivated) and the step sample 1 (passivated). The pump (1.495 eV) and probe (2.13 eV) absorption lengths are $\sim 10.1\text{ nm}$ and $\sim 9.8\text{ nm}$ respectively³². This very small penetration depth is due to the specific electronic band structure in this energy range where interband transitions exist³². The maximum fluence was $100\ \mu\text{J}\cdot\text{cm}^{-2}$ which corresponds to a photoexcited carriers concentration of around 10^{16} cm^{-3} . Furthermore, in the experiments, the pump and probe are focused with a microscope objective providing a typical spot radius of $\approx 5\text{ micrometers}$. With this spot diameter and sample length (along the gradient) of around 1.5 cm (very smooth gradient for the wedge sample) and a width of 1 cm, we were able to investigate many positions along and perpendicular to the gradient which permitted to get a very good statistic of transient reflectivity signals, crucial to reveal subtle properties changes.

Data availability. The authors declare that the data supporting the findings of this study are available within the article and its Supplementary Information.

References

- Moore, J. E. The birth of topological insulators. *Nature* **464**, 194–198 (2010).
- Hazan, M. Z. & Kane, C. L. *Colloquium: Topological Insulators*. *Rev. Mod. Physics* **82**, 3045–3067 (2010).
- Kondou, K. *et al.* Fermi-level-dependent charge-to-spin current conversion by Dirac surface states of topological insulators. *Nature Phys.* **12**, 1027–1032 (2016).
- Hajlaoui, M. *et al.* Tuning a Schottky barrier in a photoexcited topological insulator with transient Dirac cone electron-hole asymmetry. *Nature Comm.* **5**, 3003 (2014).
- Mittleman, D. M. *et al.* Quantum size dependence of femtosecond electronic dephasing and vibrational dynamics in CdSe nanocrystals. *Phys. Rev. B* **49**, 14435 (1994).
- Allan, G. & Delerue, C. Confinement effects in PbSe quantum wells and nanocrystals. *Phys. Rev. B* **70**, 245321 (2004).
- Stella, A. *et al.* Size effects in the ultrafast electronic dynamics of metallic tin nanoparticles. *Phys. Rev. B* **53**, 15497–15500 (1996).
- Arbouet, A. *et al.* Electron-Phonon Scattering in Metal Clusters. *Phys. Rev. Lett.* **90**, 177401–4 (2003).
- Kirchmann, P. S. *et al.* Quasiparticle lifetimes in metallic quantum-well nanostructures. *Nature Phys.* **6**, 782–785 (2010).
- Zhang, Y. *et al.* Crossover of the three-dimensional topological insulator Bi₂Se₃ to the two-dimensional limit. *Nature Phys.* **6**, 584–8 (2010).
- Vidal, F. *et al.* Photon energy dependence of circular dichroism in angle-resolved photoemission spectroscopy of Bi₂Se₃ Dirac states. *Phys. Rev. B* **88**, 241410 (2013).
- Li, Y.-Y. *et al.* Intrinsic Topological Insulator Bi₂Te₃ Thin Films on Si and Their Thickness Limit. *Adv. Mater.* **22**, 4002–4007 (2010).
- Lu, H.-Z., Shan, W.-Y., Yao, W., Niu, Q. & Shen, S.-Q. Massive Dirac fermions and spin physics in an ultrathin film of topological insulator. *Phys. Rev. B* **81**, 115407 (2010).
- Linder, J., Yokoyama, T. & Sudbo, A. Anomalous finite size effects on surface states in the topological insulator Bi₂Se₃. *Phys. Rev. B* **80**, 205401 (2009).
- Zhou, B. *et al.* Finite Size Effects on Helical Edge States in a Quantum Spin-Hall System. *Phys. Rev. Lett.* **101**, 246807 (2008).
- Liu, C.-X. *et al.* Oscillatory crossover from two-dimensional to three-dimensional topological insulators. *Phys. Rev. B* **81**, 041307 (2010).
- Kim, Y. S. *et al.* Thickness-dependent bulk properties and weak antilocalization effect in topological insulator Bi₂Se₃. *Phys. Rev. B* **84**, 073109 (2011).
- Kim, D. *et al.* Surface conduction of topological Dirac electrons in bulk insulating Bi₂Se₃. *Nat. Phys.* **8**, 459–463 (2012).
- Glinka, Y. D. *et al.* Ultrafast carrier dynamics in thin-films of the topological insulator Bi₂Se₃. *Appl. Phys. Lett.* **103**, 151903 (2013).
- Kim S. *et al.* Resonance effects in thickness-dependent ultrafast carrier and phonon dynamics of topological insulator Bi₂Se₃. *Nanotech.* **27** 045705 (2016)
- Sobota, J. A. *et al.* Ultrafast Optical Excitation of a Persistent Surface-State Population in the Topological Insulator Bi₂Se₃. *Phys. Rev. Lett.* **108**, 117403 (2012).
- Hsieh, D. *et al.* Selective Probing of Photoinduced Charge and Spin Dynamics in the Bulk and Surface of a Topological Insulator. *Phys. Rev. Lett.* **107**, 077401 (2011).
- Wang, Y. H. *et al.* Measurement of Intrinsic Dirac Fermion Cooling on the Surface of the Topological Insulator Bi₂Se₃ Using Time-Resolved and Angle-Resolved Photoemission Spectroscopy. *Phys. Rev. Lett.* **109**, 127401 (2012).
- Hajlaoui, M. *et al.* Ultrafast Surface Carrier Dynamics in the Topological Insulator Bi₂Te₃. *Nano Lett.* **12**, 3532–3536 (2012).
- Onishi, Y. *et al.* Ultrafast carrier relaxation through Auger recombination in the topological insulator Bi_{1.5}Sb_{0.5}Te_{1.5}Se_{1.5}. *Phys. Rev. B* **91**, 085306 (2015).
- Golias, E. & Sanchez-Barriga, J. Observation of antiphase coherent phonons in the warped Dirac cone of Bi₂Te₃. *Phys. Rev. B* **94**, 161113(R) (2016).
- Giraud, S., Kundu, A. & Egger, R. Electron-phonon scattering in topological insulator thin films. *Phys. Rev. B* **85**, 035441 (2012).
- Rapacz, R., Balin, K., Nowak, A. & Szade, J. Spectroscopic characterization of high-purity polycrystalline BiTe films grown by thermal evaporation. *J. Cryst. Growth* **401**, 567–572 (2014).
- Seah, M. P. & Spicer, S. J. Ultrathin SiO₂ on Si II. Issues in quantification of the oxide thickness. *Surf. Interf. Anal.* **33**, 631 (2002).
- Hatch, R. C. *et al.* Stability of the Bi₂Se₃ (111) topological state: Electron-phonon and electron-defect scattering. *Phys. Rev. B* **83**, 241303(R) (2011).

31. Park, B. C. *et al.* Terahertz single conductance quantum and topological phase transitions in topological insulator Bi₂Se₃ ultrathin films. *Nat. Comm.* **6**, 6552 (2015).
32. Greenaway, D. L. & Harber, G. Band structure of bismuth telluride and their alloys. *J. Phys. Chem. Solids* **26**, 1585–1604 (1965).
33. Weis, M. *et al.* Ultrafast Light-Induced Coherent Optical and Acoustic Phonons in few Quintuple Layers of Topological Insulators Bi₂Te₃. *Phys. Rev. B* **92**, 014301 (2015).
34. Flock, J., Dekorsy, T. & Misochko, O. V. Coherent lattice dynamics of the topological insulator Bi₂Te₃ probed by ultrafast spectroscopy. *App. Phys. Lett.* **105**, 011902 (2014).
35. Kumar, N. *et al.* Spatially resolved femtosecond pump-probe study of topological insulator Bi₂Se₃. *Phys. Rev. B* **83**(83), 235306 (2011).
36. Wang, Y., Guo, L., Xu, X., Pierce, J. & Venkatasubramanian, R. Origin of coherent phonons in Bi₂Te₃ excited by ultrafast laser pulses. *Phys. Rev. B* **88**, 064307 (2013).
37. Eddrief, M., Atkinson, P., Etgens, V. & Jusserand, B. Low-temperature Raman fingerprints for few-quintuple layer topological insulator Bi₂Se₃ films epitaxially on GaAs. *Nanotech.* **25**, 245701 (2014).
38. Glinka, Y. D., Babakiray, S. & Lederman, D. Plasmon-enhanced electron-phonon coupling in Dirac surface states of the thin-film topological insulator Bi₂Se₃. *J. Appl. Phys.* **118**, 135713 (2015).
39. Shahil, K. M., Hossain, M. Z., Teweldebrhan, D. & Balandin, A. A. Crystal symmetry breaking in few-quintuple Bi₂Te₃ films: Applications in nanometrology of topological insulators. *Appl. Phys. Lett.* **96**, 153103 (2010).
40. Giret, Y., Gellé, A. & Arnaud, B. Entropy Driven Atomic Motion in Laser-Excited Bismuth. *Phys. Rev. Lett.* **106**, 155503 (2011).
41. Johnson, S. L. *et al.* Nanoscale Depth-Resolved Coherent Femtosecond Motion in Laser-Excited Bismuth. *Phys. Rev. Lett.* **100**, 155501 (2008).
42. J.M. Ziman, *Principle of Theory of Solids*, Cambridge University Press, 1964.
43. Huang, B.-L. & Kaviani, M. Ab initio and molecular dynamics predictions for electron and phonon transport in bismuth telluride. *Phys. Rev. B* **77**, 125209 (2008).
44. Thomsen, C., Grahn, H. T., Maris, H. J. & Tauc, J. Surface generation and detection of phonons by picosecond light pulses. *Phys. Rev. B* **34**, 4129 (1986).
45. Yu, P. & Cardona, M. *Fundamentals of Semiconductors*, Springer Verlag Heidelberg (1996).
46. Gusev V. and Karabutov A. *Laser Optoacoustics*, AIP, New York (1993).
47. Ruello, P. & Gusev, V. Physical mechanisms of coherent acoustic phonons generation by ultrafast laser action. *Ultrasonics* **56**, 21–35 (2015).
48. Wright, O. B. Thickness and sound velocity measurement in thin transparent films with laser picosecond acoustics. *J. Appl. Phys.* **71**, 1617 (1992).
49. Gusev, V. *Acustica Acta Acustica* **82**, S37 (1996).
50. Matsuda, O. & Wright, O. B. Laser picosecond acoustics with oblique probe light incidence. *Rev. Sci. Instrum.* **74**, 895 (2003).

Acknowledgements

This work was supported by the French Ministry of Education and Research, the CNRS, Region Pays de la Loire (CPER Femtosecond Spectroscopy equipment program) and the LIA-CNRS (Laboratoire International Associé) IM-LED. The partial financial support from National Science Center under project 2016/21/B/ST5/02531 is acknowledged. R. Rapacz was supported by FORSZT PhD fellowship. We are grateful to V. Juvé, D. Boschetto and M. Lejman for stimulating discussions.

Author Contributions

M.W. and B.W. did the time-resolved optical experiments. M.W., B.W., K.B., R.R. and J.S. prepared the samples. M.W., B.W. and J.S. performed the XPS and LEED analysis. G.V., and P.R. provided help during the time-resolved optical experiments. All authors contributed to the analysis of the results. P.R. and J.S. conceived the project and all the authors contributed to the preparation of the paper.

Additional Information

Supplementary information accompanies this paper at <https://doi.org/10.1038/s41598-017-12920-4>.

Competing Interests: The authors declare that they have no competing interests.

Publisher's note: Springer Nature remains neutral with regard to jurisdictional claims in published maps and institutional affiliations.

 **Open Access** This article is licensed under a Creative Commons Attribution 4.0 International License, which permits use, sharing, adaptation, distribution and reproduction in any medium or format, as long as you give appropriate credit to the original author(s) and the source, provide a link to the Creative Commons license, and indicate if changes were made. The images or other third party material in this article are included in the article's Creative Commons license, unless indicated otherwise in a credit line to the material. If material is not included in the article's Creative Commons license and your intended use is not permitted by statutory regulation or exceeds the permitted use, you will need to obtain permission directly from the copyright holder. To view a copy of this license, visit <http://creativecommons.org/licenses/by/4.0/>.

© The Author(s) 2017



Physicochemical analysis of Bi_2Te_3 – (Fe, Eu) – Bi_2Te_3 junctions grown by molecular beam epitaxy method

K. Balin,^{1,2} R. Rapacz,^{1,2} M. Weis,^{1,2} and J. Szade^{1,2}

¹Silesian Center for Education and Interdisciplinary Research, University of Silesia, 75 Pułku Piechoty 1A, 41-500 Chorzów, Poland

²A. Chełkowski Institute of Physics, University of Silesia, Uniwersytecka 14, 40-007 Katowice, Poland

(Presented 2 November 2016; received 23 September 2016; accepted 29 November 2016; published online 2 March 2017)

Topological insulators (TI) are a class of materials gaining in importance due to their unique spin/electronic properties, which may allow for the generation of quasiparticles and electronic states which are not accessible in classical condensed-matter systems. Not surprisingly, TI are considered as promising materials for multiple applications in next generation electronic or spintronic devices, as well as for applications in energy conversion, such as thermo-electrics. In this study, we examined the practical challenges associated with the formation of a well-defined junction between a model 3D topological insulator, Bi_2Te_3 , and a metal, Fe or Eu, from which spin injection could potentially be realized. The properties of multilayer systems grown by molecular beam epitaxy (MBE), with Fe or Eu thin films sandwiched between two Bi_2Te_3 layers, were studied *in-situ* using electron diffraction and photoelectron spectroscopy. Their magnetic properties were measured using a SQUID magnetometer, while the in-depth chemical structure was assessed using secondary ion mass spectroscopy. An examination of impact of Bi_2Te_3 structure on chemical stability of the junction area has been realized. For Fe, we found that despite room temperature growth, a reaction between the Fe film and Bi_2Te_3 takes place, leading to the formation of FeTe and also the precipitation of metallic Bi. For the Eu tri-layer, a reaction also occurs, but the Te chemical state remains intact. © 2017 Author(s). All article content, except where otherwise noted, is licensed under a Creative Commons Attribution (CC BY) license (<http://creativecommons.org/licenses/by/4.0/>). [<http://dx.doi.org/10.1063/1.4978005>]

I. INTRODUCTION

Topological Insulators (TI) are a new quantum state of matter which exhibits unique quantum-mechanical properties, driving peculiar characteristics of the surface states.^{1,2} It is well known that defects, strain and doping influence the existence of metallic surface states. The explanations of particular effects observed in pure TI are complex, and become even more complicated when TI heterostructures are considered. In such cases, quantum proximity effects must be considered, but one also must inevitably consider the effects of inter-diffusion and chemical stability as well. Although studies of phenomena occurring at the interfaces of TI heterostructures were recently conducted, knowledge in this field is in its infancy. The effects related to TI - metal interfaces are very important from both a fundamental and application point of view. Due to their exotic spin nature and topological protection of the surface states, TI are viewed as promising materials for multiple applications in next generation electronic or spintronic devices. There are many ideas for novel TI-based devices,^{3,4} which would use the surface electronic states, and would allow for spin manipulation via ferromagnetic electrodes. Such devices could be based on TI – ferromagnetic (FM) junctions, in concept made to inject spins from the ferromagnetic contact to the TI material. Spin transport properties across FM/TI interfaces have been studied by ferromagnetic resonance (FMR).⁵⁻⁷ The engineering of such junctions is a crucial step for further development of diverse TI-based spintronic devices. Unfortunately, reports on the fabrication of such devices have been rare, which is inevitably connected to the technical



challenges of their engineering. To help overcome these engineering issues, our main point of interest is directed towards obtaining a detailed and broad characterization of TI-metal heterostructures. Such characterization includes analysis of crystallographic, electronic, and chemical structure, but is also aimed at the determination of their transport and magnetic properties.

II. EXPERIMENTAL DETAILS

For our model TI, we have chosen bismuth telluride; a material with well-known electronic structure, good separation of the core levels of heterostructure components (XPS spectra), and a number of high quality papers describing its properties.⁸⁻¹⁰ For the fabrication of heterostructures with Bi₂Te₃ TI, we selected two magnetic metals (M) which are potential electrodes for the future devices. One of those metals, Fe, is a well-known ferromagnet with relatively stable ferromagnetic properties starting from several monolayers.¹¹ We also selected one of the rare earth metals, Eu, mostly due to the fact that rare earths have a localized magnetic moment connected with the partly filled *4f* shells. Divalent Europium exhibits a high, pure spin magnetic moment, but its valence is unstable, and trivalent europium is non-magnetic.¹²

The subjects of our analysis are heterostructures prepared in the form of a multilayer stack of alternately deposited Bi₂Te₃ and (*3d*, *4f*)-M layers on a mica substrate. Monocrystalline mica was selected to allow for monocrystalline growth of the Bi₂Te₃ film. A Molecular Beam Epitaxy (MBE) system was used to grow each layer of the heterostructures, starting from growth in co-deposition mode of the 15nm thick, monocrystalline Bi₂Te₃ film. The next step was to deposit the M layer of ~2 nm thick iron or europium, and then finally to cap the structure with an additional 2 nm thick Bi₂Te₃ layer. Figure 1a is a visual representation of the final structure. For us, the regions of interest were located at both of the TI – (*3d*, *4f*)-M interfaces. Since Bi₂Te₃ grows in a quintuple layer (QL ~ 1 nm) structure with the lattice parameters $a=4.38 \text{ \AA}$, $c=30.49 \text{ \AA}$ we decided to focus on two cases; (1) interfacing 15 QLs of Bi₂Te₃ with the Fe or Eu, (2) interfacing the Fe or Eu layer with 2 QLs of Bi₂Te₃.

The *in-situ* measurements were made at each step of the deposition process, while the *ex-situ* measurements were performed after the growth of the entire heterostructure. Our studies were predominantly done in a large ultra-high vacuum (UHV) cluster, which connects the growth chamber with the analytical chamber under UHV conditions, allowing for *in-situ* crystallographic characterization (Reflection High Energy Electron Diffraction, Low Electron Energy Diffraction) and electronic structure determination (X-ray Photoelectron Spectroscopy). Certain magnetic and chemical properties of these heterostructures were then determined *ex-situ* using a SQUID magnetometer, while a 3D analysis of the chemical structure was performed using Time of Flight Secondary Ion Mass Spectrometry (TOF-SIMS).

III. RESULTS AND DISCUSSIONS

The crystallographic measurements, RHEED and LEED, indicated growth of monocrystalline iron (see Fig. 1c), polycrystalline europium (see Fig. 1f), on the surface of monocrystalline 15 nm thick Bi₂Te₃ (Fig. 1d and 1g). Visible at the RHEED diffraction pattern of europium weak streaks (see Fig 1f) are associated with the underlying Bi₂Te₃ layer. The top Bi₂Te₃ layer deposited on iron exhibits monocrystalline structure (see Fig. 1b), whereas the Bi₂Te₃ deposited on the europium layer is polycrystalline (see Fig 1e). LEED measurements show that the monocrystalline Bi₂Te₃ layers crystallize in a trigonal system. Weak LEED pattern have been observed for Fe deposited on 15 nm thick Bi₂Te₃ layer (see Fig 1c round shaped inset). Additional layers of Eu or TI do not give a LEED diffraction pattern, indicating the lack of single-crystalline structure.

Angle dependent XPS measurements were performed to determine the electronic structure at the interfaces. Two different analysis geometries were used to change the surface sensitivity of the measurements (studies performed with tilted heterostructures). Particular attention was paid to the chemical states at the TI-(*3d*, *4f*)-M junction, done mostly by detecting evidence of a chemical reaction between junction components. In previous work, we precisely studied the electronic and crystalline structure of non-stoichiometric polycrystalline Bi_xTe_y thin films¹³ as well as stoichiometric Bi₂Te₃

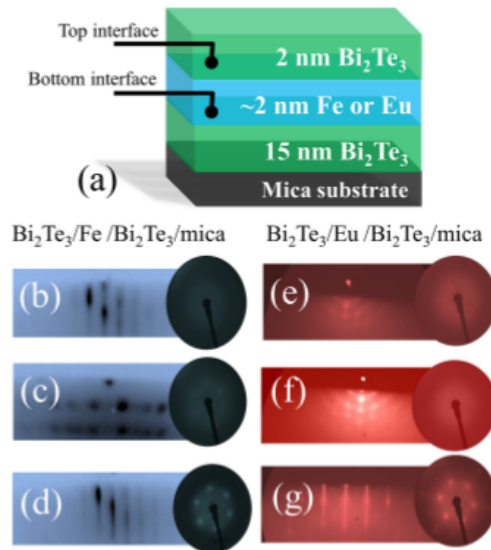


FIG. 1. Structure of deposited heterostructures (a) combined with diffraction patterns obtained with the use of RHEED and LEED at each step of deposition process for (b) 2nm of Bi_2Te_3 top layer, (c) 2.4nm Fe, (d) 15nm Bi_2Te_3 bottom layer along [100] direction, (e) 2nm Bi_2Te_3 top layer, (c) 2 nm Eu, (d) 15nm of Bi_2Te_3 bottom layer along [1-20] direction.

monocrystalline films.¹⁴ Based on that knowledge, we are able to distinguish effects related to the widely understood disorder from effects occurring due to interfacing the TI surface with the surface of deposited on TI layer metal.

The results of XPS measurements (see Fig 2) allowed us to analyze the behavior of the sample in several different aspects. First, Eu remains in the divalent state (see Fig. 2(a1)–2(a3)), however some weak $\text{Eu}^{2+} \leftrightarrow \text{Eu}^{3+}$ transition were observed in measurements of the bottom $\text{Eu-Bi}_2\text{Te}_3$ interface (highlighted yellow area and Fig. 2(a2)). A weak $\text{Eu}^{2+} \leftrightarrow \text{Eu}^{3+}$ transition was observed for

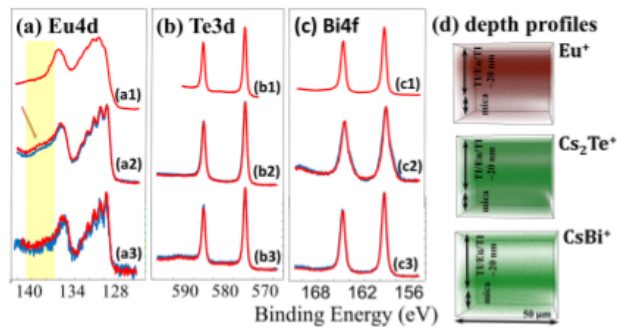


FIG. 2. The XPS photoemission spectra of (a) Eu4d (b) Te3d (c) Bi4f. Spectra obtained (a1) for 20nm thick Eu grown on Mo substrate, (b1, c1) Te3d and Bi4f of 15 nm thick Bi_2Te_3 layer respectively, (a2, b2, c2) after deposition of 2 nm thick Eu layer, (a3, b3, c3) after deposition of 2 nm thick Bi_2Te_3 top layer. Blue lines correspond to angle dependent XPS measurements. 3D depth profiles (d) represent distribution of Eu ions and (Te or Bi) cesium ions within the heterostructure.

heterostructures with 2 nm thick Eu, while for the heterostructure with 0.5 nm thick Eu (not shown), this transition was not observed. For Eu in the divalent state, exchange splitting leads to the very well resolved structure of the Eu $4d_{5/2}$ core level seen in Fig. 2(a2–3). The splitting of particular states, which can be ascribed to the various 9D_J final states, is measured to be 0.9 eV, the same as in pure Eu. Interestingly, the known effect of reduced intensity of the lowest binding energy lines originating from the high spin states¹⁵ (see referenced spectrum of pure europium Fig. 2(a1)) is, surprisingly, removed by when Eu is in contact with Bi_2Te_3 (Fig. 2(a2) and 2(a3)). This phenomenon requires further studies. Inter-mixing of the junction components at room temperature was observed, the evidence of which was seen in the chemical shifts of the core levels, as well as in the TOF-SIMS depth profiles. The influence of the Eu layer on the electronic structure of the bottom Bi_2Te_3 layer manifests in the $\text{Bi}4f$ spectrum as an additional chemical state of Bi (see Fig. 2(c2)), clearly visible as a broadening of the $\text{Bi}4f_{7/2}$ line. The additional Bi state is associated with a layer of metallic Bi, as well as the partial $\text{Eu}^{2+} \leftrightarrow \text{Eu}^{3+}$ transition. Tilting the sample does not significantly change the ratio of metallic Bi to Bi bound with Te in the Bi_2Te_3 compound. From this we conclude that the intermixing depth at the bottom interface is about 4 nm. The influence of europium on the electronic structure of tellurium is minor. Finally, when compared to a pure Bi_2Te_3 film, no significant changes were observed in the electronic structure of Bi or Te forming the top 2 nm thick Bi_2Te_3 top layer. The cap layer, therefore, seems to be unaffected by the underlying Eu layer. It is worth noting that intermixing between the Bi_2Te_3 and Eu layers occurs preferably when the Bi_2Te_3 under-layer is monocrystalline (compare Fig. 2(c1) and 2(c2) with Fig 1g and e).

TOF-SIMS depth profiles have been presented in Fig. 2d. Due to the weak signal of Te and Bi ions in TOF-SIMS measurements, the distribution of Cs_2Te^+ and CsBi^+ ions is presented. The signal-boosting Cs came from a Cs source which was used as a sputtering gun. The TOF-SIMS depth profiles indicate that Eu diffused into the Bi_2Te_3 bottom-layer (Fig 2d for Eu^+), which was accompanied by a change in the distribution of Bi. In other words, some of the bismuth ions were displaced from their original position in the layer stack (see Fig. 2d for CsBi^+). This data confirms the reaction observed in XPS measurements.

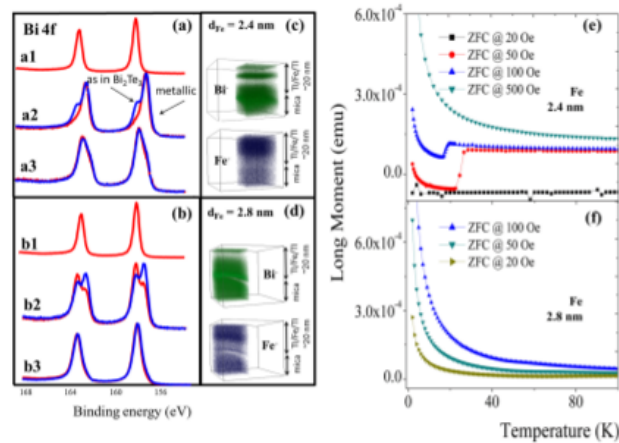


FIG. 3. The XPS photoemission spectra of (a) $\text{Bi}4f$ – obtained (a1) for 15 nm thick Bi_2Te_3 bottom layer, (a2) after deposition of 2.4 nm thick Fe layer, (a3) after deposition of 2 nm thick Bi_2Te_3 top layer. XPS of (b) $\text{Bi}4f$ – obtained (b1) for 15 nm thick Bi_2Te_3 bottom layer, (b2) after deposition of 2.8 nm thick Fe layer, (b3) after deposition of 2 nm thick Bi_2Te_3 top layer. Blue lines correspond to angle dependent XPS measurements. 3D TOF-SIMS depth profiles of (c) heterostructure with 2.4 nm thick Fe layer, (d) 2.8 nm Fe. The M(T) curves obtained in zero-field-cooled experiment at several different fields for (e) heterostructure with 2.4 nm thick Fe, (f) 2.8 nm thick Fe.

For the heterostructures with Fe inter-mixing at room temperature was observed through chemical shifts of the Bi4f photoemission line indicating strong changes in the electronic structure of Bi. We relate intermixing to the reaction between Fe and Te, the reaction leads to formation of, most probably, a thin TeFe layer. The reaction leads to separation of metallic Bi. In case of heterostructure where thickness of Fe, $d_{Fe}=2.4$ nm, this is accompanied by the separation of a metallic Bi layer (see Fig.3(a2), 3(a3), 3c). The effect of segregation of metallic Bi layer are not seen in the heterostructure with a slightly different Fe layer thickness, $d_{Fe}=2.8$ nm (see Fig 3d), probably metallic Bi is distributed in FeTe+Bi₂Te₃ matrix. Angle dependent XPS measurements (see blue lines in Fig. 3a and 3b) as well as TOF-SIMS investigations (Fig.3c and 3d) allowed us to conclude that both the geometrical alignment of the layers, as well as chemical instability at both interfaces occurred in the heterostructures. Surprisingly those factors are different for two structures with slightly different Fe content. The observed at layer/mica interface curved region (see Fig. 3d) in distribution maps of Bi-and Fe-is due to different charging of heterostructure and mica.

The magnetic properties of the heterostructures containing Fe strongly depend on the processes taking place at Bi₂Te₃-Fe interfaces and the deposition conditions. More precisely, a slight difference in the thickness of the deposited Fe caused enormous changes of the magnetic properties of the system. In case of our studies, for a certain thicknesses of Fe, $d_{Fe}=2.4$ nm, a transition to a diamagnetic state was observed below (relatively high) temperatures reaching 35 K with an applied parallel to the film surface magnetic field of 100 Oe (see Fig. 3e). The M(H) curves showed a narrow (40 Oe) hysteresis loop at 2 K with the exchange bias effect. These characteristics were not observed, however, in the sample with $d_{Fe}=2.8$ nm (see Fig. 3f). This data seems to exclude the presence of superconductivity in the sample; we are probably dealing with unusual transitions between different magnetic states. An interesting question, which will be investigated in future studies, is related to possible superconductivity in the FeTe layer formed when $d_{Fe}=2.4$ nm.

IV. CONCLUSIONS

The determination of the nature and properties of novel heterostructures based on topological insulators can be used to help develop new classes of devices and technologies for future applications. The studies of two model junctions were performed in terms of chemical stability at the TI - M interfaces. From the XPS studies we showed that even at room temperature, the deposition of Fe and Eu films on well-defined monocrystalline bismuth telluride leads to chemical instability and the formation of new phases at the interfaces, such as FeTe and metallic Bi. Facts like this must be taken into account when planning and engineering future devices based on TI. In our study, we also found that the macroscopic magnetic properties of the heterostructures are very sensitive to the thickness of the Fe layer. The influence of the metallic ferromagnetic films should be studied thoroughly after taking the chemical reactions taking place at the interfaces into account. Our results indicate that both the geometry and chemical stability of such junctions have a critical influence on the magnetic properties of TI-M-TI heterostructures. *Ex-situ* characterization, for example via 3D depth profiling using a TOF-SIMS spectrometer, can help verify structural and compositional agreement between nominal/assumed vs. fabricated junctions.

- ¹M. Z. Hasan and C. L. Kane, *Reviews of Modern Physics* **82**, 3045 (2010).
- ²X. L. Qi and S. C. Zhang, *Reviews of Modern Physics* **83**, 1057 (2011).
- ³M. Eschbach *et al.*, *Nature Communications* **6**, 8816 (2015).
- ⁴M. Q. He, J. Y. Shen, A. P. Petrović, Q. L. He, H. C. Liu, Y. Zheng, C. H. Wong, Q. H. Chen, J. N. Wang, K. T. Law, I. K. Sou, and R. Lortz, *Scientific Reports* **6**, 32508 (2016).
- ⁵A. A. Baker, A. I. Figueroa, L. J. Collins-McIntyre, G. van der Laan, and T. Hesjedal, *Scientific Reports* **5**, 7907 (2015).
- ⁶A. A. Baker, A. I. Figueroa, G. van der Laan, and T. Hesjedal, *Results in Physics* **6**, 293 (2016).
- ⁷M. Jamali, J. S. Lee, J. S. Jeong, F. Mahfouzi, Y. Lv, Z. Zhao, B. K. Nikolić, K. A. Mkhoyan, N. Samarth, and J. P. Wang, *Nano Letters* **15**(10), 7126 (2015).
- ⁸H. Zhang, C. X. Liu, X. L. Qi, X. Dai, Z. Fang, and S. C. Zhang, *Nature Physics* **5**(9), 438 (2010).
- ⁹D. Hsieh, Y. Xia, D. Qian, L. Wray, F. Meier, J. H. Dil, J. Osterwalder, L. Patthey, A. V. Fedorov, H. Lin, A. Bansil, D. Grauer, Y. S. Hor, R. J. Cava, and M. Z. Hasan, *Physical Review Letters* **103**, 146401 (2009).
- ¹⁰Y. L. Chen *et al.*, *Science* **325**, 178 (2009).

056323-6 Balin *et al.*

AIP Advances 7, 056323 (2017)

- ¹¹U. Gradmann, H. Elmers, and M. Przybylski, *Journal de Physique Colloques* **49**(C8), 1665 (1988).
¹²A. R. Miedema, *Journal of the Less Common Metals* **46**, 167 (1976).
¹³R. Rapacz, K. Balin, A. Nowak, and J. Szade, *Journal of Crystal Growth* **401**, 567 (2014).
¹⁴R. Rapacz, K. Balin, M. Wojtyniak, and J. Szade, *Nanoscale* **7**(38), 16034 (2015).
¹⁵J. Szade and M. Neumann, *Journal of Physics: Condensed Matter* **11**(19), 3887 (1999).

List of Figures

1.1	Artistic view of Dirac cone in topological insulators.	5
2.1	a - Evolution of the molecular band structure leading to appearance of TI state. b - Schematic of the spin-polarized surface-states dispersion in bismuth based TI. Green and blue arrow indicate the polarization of the spin. c - 3D visualization of the Dirac cone in TI. From Hasan and Kane (2010).	10
2.2	Example of object with genus $g=0$ (a) and $g=1$ (b) . c and d depict model of insulator. e and f are model of quantum Hall state. From Hasan and Kane. . .	13
2.3	Crossover of the three-dimensional topological insulator Bi_2Se_3 to the two-dimensional limit. From Yi Zhang Nature Phys. (2010).	15

2.4 Presentation of effects generated by spin-orbit coupling for working spin-current conversion: a Thanks to the Magnus effect spin Hall effect creates a force that acts on spinning particles. b, On schematic heavy metal with strong spin-orbit coupling, is marked with blue, with yellow ferromagnetic layer and on top (orange) protective capping layer. The torque created by the spin Hall effect in a magnetic bilayer separates moving spins into aligned parallel (blue arrows) and anti-parallel (red arrows) to the direction of flow; this produces polarized spin current J_S (green arrow). This effect generates anti-damping torque T_{DL} that depends on the magnetization m and the direction of the spin accumulation y . c To nullify the effect of the Magnus force spin angular momenta (dashed arrows) must be frozen along the current direction. d In the case of a system without inversion symmetry like in topological insulators, this effect creates a spin-polarized current. In the case of breaking the inversion symmetry directly at the interface between the material with strong spin-orbit coupling (blue) and ferromagnetic layer (yellow) spin accumulates along the transverse direction leading to the appearance of non-equilibrium spin-orbit torque T_{FL} . From A. Manchon Nat.Phys.(2014). 17

2.5 Crystallographic structure of Bi_2Te_3 with the quintuple layers (QL,s) connected through Van der Waals Te bonds. a Depicts view from **c** plane and b from the **b** plane. 19

2.6 Band structure a) without and b) with spin orbit interactions. 21

2.7 Optical phonon modes in Bi_2Te_3 . The “+” and “-” signs in presented figure describe motions toward and from the observer. 22

3.1 Steps of thin film growth: 1 - absorption, 2 - surface diffusion, 3 - chemical bond formation, 4 - nucleation, 5 - microstructure formation, 6 - bulk changes. 24

3.2 Physisorption potential energy for Helium calculated for various metal substrates (from E. Zaremba et.al [43]). 25

<i>LIST OF FIGURES</i>	148
3.3 Frank van der Merwe crystal growth - Layers.	26
3.4 a - Volmer Weber crystal growth - Islands. b - Stranski-Krastanov crystal growth - Mixed	28
3.5 Model of MBE chamber used in our experiments.	30
3.6 High vacuum cluster in laboratory of Surface Physics in Institute of Physics, University of Silesia.	32
3.7 Sample B1 - art view of monocrystalline sample of Bi_2Te_3 with terraces' thickness of 4, 6, 8 and 10nm	35
3.8 Sample B2 - art view of monocrystalline wedge of Bi_2Te_3 with slope of 0.66nm/mm. 36	
3.9 Sample C2 - art view of monocrystalline sample of Bi_2Te_3 with 3 sections: 1st - plateau of iron with a thickness 1nm and lenght 5mm; 2nd - wedge of iron with gradient 1Å/mm; 3rd - free surface sample of BT.	37
4.1 a - $1 \times 1 \mu m$ AFM image of sample A2, Bi_2Te_3 grown on Si(001). b - $0.45 \times 0.45 \mu m$ AFM image of sample A1 grown on Muscovite mica (110). From R.Rapacz [30]	41
4.2 a - View on the c plane (001) of Bi_2Te_3 cell. b - Two main symmetry planes in the hexagonal cell, the difference between them is precisely 30° . c and d - Artistic representation of diffraction pattern made with RHEED along with two main symmetries, colors are corresponding to the planes marked in picture b; the received pattern is in reciprocal lattice.	42
4.3 RHEED diffraction image from: a) Polycrystalline sample; b) Monocrystalline sample with additional 3D structures (for example islands or quantum dots); c) Monocrystalline structure with small terraces; d) Monocrystalline and perfectly flat structure	43
4.4 RHEED diffraction image of sample A1 along two main planes of symmetry characteristic to Bi_2Te_3 hexagonal crystal structure. Detected streaks are proof of monocrystalline terrace growth of the sample.	44

4.5	RHEED diffraction image of sample a - A2 and b - A3. Observed half circles are proof polycrystalline growth of the sample.	45
4.6	a - RHEED diffraction image of sample B2 along principal planes of symmetry characteristic to Bi_2Te_3 hexagonal crystal structure. Observed streaks are proof of monocrystalline terrace growth of the sample. b and c - RHEED diffraction image of sample C2 along two principal planes of symmetry characteristic to Bi_2Te_3 hexagonal crystal structure. Observed streaks are proof of monocrystalline terrace growth of the sample.	46
4.7	LEED diffraction image of sample A1 at different electron incident energies a) 56eV; b) 75eV; c) 98eV.	47
4.8	LEED diffraction image of sample C3 revealing characteristic Bi_2Te_3 hexagonal crystal structure. Broadening of the diffraction spots is a result of slight mismatch between nearest QL's.	48
4.9	a - LEED of 5nm thickness sample at energy 115eV. b - Art view of the cross section of the step sample B2 with an inset in the bottom of the figure showing thickness dependence of LEED image obtained at energy 80eV.	49
4.10	Schematic of <i>PhysicalElectronicsPHI5700</i> spectrometer.	51
4.11	Typical XPS spectra of pure Bi_2Te_3 sample.	53
4.12	Valence band spectra for the as grown film with various thickness.	55
4.13	XPS $Te3d_{5/2}$ a and $Bi4f_{7/2}$ b doublets for the as-grown films.	56
4.14	Fit of the $Bi4f_{7/2}$ doublet for the 6 nm thick film showing the contributions from the Bi_2Te_3 (high intensity doublet) and Bi (low intensity doublet).	56
4.15	XPS doublets of $Te3d_{5/2}$ (a) and $Bi4f_{7/2}$ (b) after oxidation of the film.	59

4.16	a - XPS spectra are fitting of $Bi4f_{7/2}$ core level and b - view over $Bi4f_{7/2}$ doublet lines. We can see two chemical states of Bi, one belonging to the oxide and second one to Bi_2Te_3 compound. c - XPS spectra fitting of $Te3d_{5/2}$ core level and d - view over $Te3d_{5/2}$ doublet lines. We can see that the tellurium has three chemical states: two main ones belong to oxide and Bi_2Te_3 , the third one probably belongs to pure Te in metallic state or FeTe compound.	60
4.17	XPS spectra of $Fe2p_{3/2}$ core level.	61
4.18	XPS spectra of valence band after the oxidation.	61
4.19	a - Artistic visualization of the surface of sample C2. Due to Stranski-Krastanov's type of growth, the sample at the start of deposition develops well-formed layers up to 10-12nm; after that, the material started to form an island-like structure that retained proper order and symmetry to the layers underneath. Highlighted with a green plane indicates the direction of the X-ray analysis beam, where the beam of ions used to remove layers was marked with red. b - Profile of sample C2 on line $Te3d_{5/2}$, the blue bottom line corresponds to the surface of the sample; the following lines were made during the removal of the next 2nm (2 QL) from the sample.	63
4.20	a - Profile of sample C2 of line Fe2p, the red bottom line corresponds to the surface of the sample following lines which were made during the removal of the next 2nm (2 QL) from the sample. b - profile of valence band, the red bottom line corresponds to the surface of the sample following lines which were made during the removal of the next 2nm (2 QL) from the sample.	64
4.21	Artistic sketch of sample C2 cross-section based on data received from the depth profile.	65
5.1	a - Schematic of two-color pump-probe experiment. b - Schematic of delay line. c - Schematic of photo detector.	69
5.2	Time scale of our ability to register physical processes.	71

5.3	Time dependence of the Fermi distribution after an ultrafast laser exciton: a - photon energy is first absorbed by the electrons, b - thermalization of the electronic subsystem, c - thermalization of the electronic subsystem with the phonon (cations) subsystem. d - TTM two temperature model shows the time scale of the processes mentioned earlier.	72
5.4	Schematic diagrams of electronic dispersions in $Bi_{1.5}Sb_{0.5}Te_{1.7}Se_{1.3}$. b - diagrams of relaxation processes of photo-excited carriers in the lowest conduction band (C1), the highest valence band (V1), and the surface states (SS) existing in 3D topological insulators: (1) photo-excitation of electron-hole pairs, (2) carrier thermalization, (3) carrier cooling due to phonon emission, (4) Auger recombination, and (5) intraband scattering from C1 and V1 to SS. From Y. Onishi et. al. Phys Rev B (2015).	74
5.5	The measured signal was fitted with function 5.6 and remaining after subtraction residua are consisting mainly of the phonon signal from the investigated region.	77
5.6	Deformation potential in band structure picture: excitation of an electron-hole pair disturbs the electronic distribution and modifies the interatomic interaction leading to a change of atomic positions and consequently to the generation of a strain field.	78
5.7	Deformation potential in molecular picture: excitation of electron from one orbital to another modifies the electronic distribution causing appearance of bonding (compression) or antibonding (expansion) interactions between atoms.	80
5.8	Scheme of two color pump (830nm) and probe (580nm) setup, used for the experiments.	81
5.9	Time-resolved optical reflectivity obtained for samples A_1, A_2, A_3 , data was normalized to largest magnitude for clarity.	85

5.10	a - optical phonon signal obtained through time derivation of obtained signal, we can see a strong signal from A_{1g}^1 mode. b - Fast Fourier transformation of the derived signal.	86
5.11	Optical phonon vibrations are confined to the unit cell and do not create a force that would act on the whole layer.	87
5.12	A_{1g}^1 optical phonon mode in Bi_2Te_3	89
5.13	a–c Coherent acoustic phonon signals extracted from the transient optical reflectivity signals. For clarity, curves have been scaled in amplitude. Dotted lines are numerical adjustments (see text for more details). d–f Corresponding coherent acoustic phonon spectra obtained by a fast Fourier transform (FFT). (g) The first two confined acoustic eigenmodes in film A1. U_z is the normal displacement of atoms.	91
5.14	Ultrafast optical response of ultrathin layers of Bi_2Te_3 . Time-resolved optical reflectivity obtained for various layers of Bi_2Te_3 for the a - step B1 and b - wedge B2 sample. The signals are normalized to the maximum of the electronic peak. (insets) The pump and probe are represented in the artist's view as red and orange beams.	93
5.15	Thickness dependence of the ultrafast carrier and phonon dynamics. a - Thickness dependence of the electron-phonon relaxation time for the wedge B2 (black squares) and step B1 (centered blue squares) samples. Thickness dependence of the A_{1g}^1 optical phonon frequency (red dots). b - Thickness dependence of the A_{1g} optical phonon amplitude (gold squares) and full width at height maximum (green dots).	94
5.16	a - Typical oscillatory component at a short time scale revealing the A_{1g} optical phonon. b - Fast Fourier Transform (FFT) of the signal shown in a reveal that the A_{1g}^1 mode is softening for the ultrathin layer.	96

5.17 Results of fitting the power of law function to the time of relaxation of hot carriers versus the film thickness. The performed calculation resulted in the relaxation of the fitting procedure close to $\alpha = 2.65$ 98

5.18 a - Art view of the cross-section of the C2 wedge sample together with continuous wavelength optical transmission, with a dashed curve, we presented calculated Beer-Lambert law, and with red reflectivity along thickness gradient. b - Contribution of the phonons signal to the transient reflectivity signal for three different thicknesses. d - Thickness dependence of the longitudinal acoustic resonance eigenmode period $1/f_0$. The red dashed slope provide an estimation of the longitudinal sound velocity of $2260m/s$ in Bi_2Te_3 . Inset shows an example of an acoustic signal with the period $1/f_0$ for the 6nm layer. 100

5.19 Scaling down a layer of Bi_2Te_3 revealed generation of strong coherent acoustic phonon. a - Map of the optical and acoustic phonon mode amplitudes with fixed pump power, the x-axis represents time and y-axis change of layer thickness. The experiment revealed the appearance of large acoustic phonon signals in the ultrathin layer. b - Thickness dependence of the photo-detected coherent acoustic signal amplitude. Green curve present model that takes into account the detection (red) contribution estimated size-dependent electron-hole acoustic deformation potential (blue) from the literature [9]. 102

5.20 All performed configurations of reflectivity measurements made with iron sample. 104

5.21	a - Time-resolved optical transmission (ΔT) and reflectivity (ΔR) obtained for the sample C1 with a pump wavelength 830nm. Signals, marked with Fe, were made on a part of sample with iron oxide, the letter B denotes the position of excitation by pump from the back side (mica side) similar for the front (F). The letters T and R are denoting transmission and reflection. b - Time-resolved optical reflectivity (ΔR) obtained for the sample C1 with a pump wavelength 415nm. c - Schematic of the relaxation process of photo-excited carriers in presence of mid-bandgap states induced by the close proximity of $\gamma-Fe_2O_3$ atoms within the structure of Bi_2Te_3	106
5.22	Time-resolved transmission (ΔT) obtained for the sample C1. Graph a presents the extracted phonon signals. b - presents overlapped derivatives of the signal showing, in the real time, the difference in frequency. Graph c presents the FFT showing appearance of blue shift of A_{g1}^1 frequency in Bi_2Te_3 doped with iron oxide.	109
5.23	a - FFT amplitude from measurements performed on the sample C2 with iron wedge, Signal revealed that the blue shift has discreet nature dependant on quantity of doping. The frequency shift appears when the relaxation time of photo-excited electron is faster than $\tau_e < 0.9p$. b - Schematic of A_{g1}^1 optical phonon mode in presence of iron in between VdW layer.	110
7.1	SHG process	122
7.2	DFG process	122
7.3	a) Photography of used setup; b) Schematic of ring OPO, optical unit with external spectrometer; c) Schematic of OPO.	123
7.4	Optical constants n and k of Bi_2Te_3 and energy loss function $-Im(1/\epsilon)$ from Kramers-Kronig analysis, $E \perp c$. From Greenaway J. Phys. Chem. Sol. (1965)[38].	124

List of Tables

2.1	Periodic table of topological insulators and superconductors. Ten symmetry classes are labelled using Altland and Zirnbauer (1997) notation.	12
2.2	Phonon modes frequencies (in THz) of Bi_2Te_3 . Letters “E” in-plane and “A” out-of-plane lattice vibrations, letter g denotes Raman active and u IR active modes.	21
3.1	Characteristics of growth of the samples.	33
4.1	Summary of the atomic concentration calculations derived from the XPS data.	53
5.1	Extracted with the fitting function E.q.4.1 relaxation times of hot carrier for the sample C1.	108

Bibliography

- [1] J.E. Moore, L. Balents, *Phys. Rev. B* 75, 121306(R) (2007)
- [2] J. E. Moore, *Nature* 464, 194-198 (2010)
- [3] M.Z. Hasan, C.L. Kane, *Rev. Mod. Phys.* 82, 3045-3064 (2010)
- [4] X.-L. Wang, S.X. Dou, C. Zhang, *NPG Asia Mater*, 2, 31-38 (2010)
- [5] R. Dey, N. Prasad, L.F. Register, S.K. Banerjee, *Phys. Rev. B* 97, 174406 (2018)
- [6] I. Žutić, J. Fabian, S.D. Sarma, *Rev. Mod. Phys.* 76, 323 (2004)
- [7] J. Sinova, S.O. Valenzuela, J.Wunderlich, C.H. Back, T. Jungwirth, *Rev. Mod. Phys.* 87, 1213 (2015)
- [8] F. Vidal, M. Eddrief, B. Rache Salles, I. Vobornik, E. Velez-Fort, G. Panaccione, M. Marangolo, *Phys. Rev. B* 83, 241410(R) (2013)
- [9] Y. Zhang, et al., *Nature Phys.* 6, 584-8 (2010)
- [10] J. Linder, T. Yokoyama, A Sudbo, *Phys. Rev. B* 80, 205401 (2009)
- [11] Y.Y. Li, et. al. *Adv. Mater.* 22, 4002-4007 (2010)
- [12] M. Weis, B. Wilk, G. Vaudel, K. Balin, R. Rapacz, A. Bulou, B. Arnaud, J. Szade, P. Ruello, *Sci. Rep.* 7: 13782 (2017)

- [13] F. Bloch, *Zeitschrift für Physik* 52, 7, (1929) 555
- [14] T. Ando, Y. Matsumoto, Y. Uemura, *J. Phys. Soc. Japan* 39, pp 279-288 (1975)
- [15] K.v. Klitzing, G. Dorda, M. Pepper, *Phys. Rev. Lett.* 45, 6, (1980) 494
- [16] H. Zhang, C.X. Liu, X.L. Qi, X. Dai, Z. Fang, S.C. Zhang, *Nature Phys.* 5, 10.103 (2009)
- [17] D. Xiao, M-Ch. Chang, Q. Niu, *Rev. Mod. Phys* 82.1959 (2010)
- [18] J. Alicea, *Rep. Prog. Phys* 75, 7 (2012)
- [19] D. Hsieh, D. Qian, L. Wray, Y. Xia, Y.S. Hor, R.J. Cava, M.Z. Hasan, *Nature*, 452, 970-974 (2008)
- [20] B.A. Bernevig, T.L. Hughes, S.C. Zhang, *Science*, 314, 1757-1761 (2006)
- [21] K. Shen, G. Vignale, R. Raimondi, *Phys. Rev. Lett.* 112, 096601 (2014)
- [22] K.T. Yamamoto, Y. Shiomi, K. Segawa, Y. Ando, E. Saitoh, *Phys. Rev.* B94, 024404 (2016)
- [23] J.C. Rojas-Sanchez, S. Oyarzun, Y. Fu, A. Marty, C. Vergnaud, S. Gambarelli, L. Vila, M. Jamet, Y. Ohtsubo, A. Taleb-Ibrahimi, P. Le Fèvre, F. Bertran, N. Reyren, J.M. George, A. Fert, *Phys. Rev. Lett.* 116, 096602 (2016)
- [24] Z. Alpichshev, J.G. Analytis, J.H. Chu, I.R. Fisher, Y.L. Chen, Z.X. Shen, A. Fang, A. Kapitulnik, *Phys. Rev. Lett.* 104, 016401 (2010)
- [25] P. Roushan, J. Seo, C.V. Parker, Y.S. Hor, D. Hsieh, D. Qian, A. Richardella, M.Z. Hasan, R.J. Cava, A. Yazdani, *Nature* 460, 1106–1109 (2009)
- [26] J. Chen, H.J. Qin, F. Yang, J. Liu, T. Guan, F.M. Qu, G.H. Zhang, J.R. Shi, X.C. Xie, C.L. Yang, K.H. Wu, Y.Q. Li, L. Lu, *Phys. Rev. Lett.* 105, 176602 (2010)

- [27] M.V. Costache, I. Neumann, J.F. Sierra, V. Marinova, M.M. Gospodinov, S. Roche, S.O. Valenzuela, *Phys. Rev. Lett.* 112, 086601 (2014)
- [28] D. Kim, Q. Li, P. Syers, N.P. Butch, J. Paglione, S.D. Sarma, M.S. Fuhrer, *Phys. Rev. Lett.* 109, 166801 (2012)
- [29] M. Weis, K. Balin, R. Rapacz, A. Nowak, M. Lejman, J. Szade, P. Ruello, *Phys. Rev. B* 92, 014301 (2015)
- [30] R. Rapacz, K. Balin, A. Nowak, J. Szade, *Journal of Crystal Growth* 401 567-572 (2014)
- [31] C.X. Liu, H.J. Zhang, B. Yan, X.L. Qi, T. Frauenheim, X. Dai, Z. Fang, S.C. Zhang, *Phys. Rev. B* 81, 041307(R) (2010)
- [32] H.Z. Lu, W.Y. Shan, W. Yao, Q. Niu, S.Q. Shen, *Phys. Rev. B* 81, 115407 (2010)
- [33] M. König, H. Buhmann, L.W. Molenkamp, T. Hughes, C.X. Liu, X.L. Qi, S.C. Zhang, *J. Phys. Soc. Jpn.* 77, 031007 (2008)
- [34] K. Balin, R. Rapacz, M. Weis, J. Szade, *AIP Advances* 7, 056323 (2017)
- [35] Y. Feutelais, *Materials Research Bulletin* 28 (1993)
- [36] J. Kaczkowski, A. Jezierski, *Materials Science-Poland* 4, 26 (2008)
- [37] P. Larson, S.D. Mahanti, M.G. Kanatzidis, *Phys. Rev. B* 61, 8162 (2000)
- [38] D.L. Greenaway, G. Harbeke, *J. Phys. Chem. Solids* 26, 1585 (1965)
- [39] W. Richter, H. Köhler, C.R. Becker, *Phys. Status Solidi B* 84, 619 (1977)
- [40] W. Kullmann, J. Geurts, W. Richter, N. Lehner, H. Rauh, U. Steigenberger, G. Eichhorn, G. Geick, *Phys. Status Solidi B* 125, 131 (1984)

- [41] Y. Wang, L. Guo, X. Xu, J. Pierce, and R. Venkatasubramanian, *Phys. Rev. B* 88, 064307 (2013)
- [42] M. A. Herman, H. Sitter, *Molecular Beam Epitaxy: Fundamentals and Current Status*, Springer-Verlag, 1989
- [43] E. Zaremba and W. Kohn, *Phys. Rev. B* 15 (4): 1769, (1977)
- [44] K. Hoefera, C. Beckera, D. Rataa, J. Swansona, P. Thalmeiera, and L. H. Tjenga, *PNAS* 101, 14979-14984 (2014)
- [45] S. Golia, M. Arora, R.K. Sharma, A.C. Rastogi, *Current App. Phys.* 3 195-197 (2003)
- [46] K. Watanabe, N. Sato, S. Miyoba, *J. Appl. Phys.* 54 1256 (1983)
- [47] F.A.A. Amin, A.S.S. Al Ghaffari, M.A. Issar, A.M. Habib, *J. Mater. Sci.* 27 1250 (1992)
- [48] S.A. Omer, U.G. Isifield, *Solar Energy Mater. Solar Cell* 53 67 (1998)
- [49] J.C. Tedenac, S. Charar, *Phys. Low Dimens. Struct.* 5-6 61 (2000)
- [50] J. W.G. Bos, F. Faucheux, R.A. Downie, A.J. Marcinkova, *Sol. Stat. Chem.* 193, 13-18 (2012)
- [51] R.J. Cava, J. Huiwen, M.K. Fuccillo, Q.D. Gibson, Y.S. Hor, *J. Mater. Chem. C* 1 (2013) 3176
- [52] M.P. Seah, S.J. Specker, *Surf. Interf. Anal.* 33, (2002) 631
- [53] S. Tanuma, C. J. Powell, D. R. Penn, *Surf. Interf. Anal.* 21, (1994)165
- [54] QUASES program by S. Tougaard
- [55] A.P. Grosvenor, B.A. Kobe, M.C. Biesinger, N.S. McIntyre, *Surf. Interface Anal.* 36: 1564 – 1574 (2004)

- [56] C. Kittel, Introduction to Solid State Physics, J. Wiley and Sons, 8th Edition (2005)
- [57] V.E. Gusev, O.B. Wright, Phys. Rev. B 57, 5 (1998)
- [58] M. I. Kaganov, I. M. Lifshitz, L. V. Tana-tarov, Sov. Phys. JETP4, 173 (1957)
- [59] V.E. Gusev, A. A. Karabutov, AIP Press, New York (1993)
- [60] P. Ruello, V. E. Gusev, Ultrasonics 56, 21-36 (2015)
- [61] E. Golias, J. Sanchez-Barriga, Phys. Rev. B 94, 161113(R) (2016)
- [62] M. Perner, S. Gresillon, J. Mrz, G. von Plessen, J. Feldmann J. Porstendorfer, K.-J. Berg, G. Berg, Phys. Rev. Lett. 85, 792 (2000)
- [63] C. Thomsen, H. T. Grahn, H. J. Maris, J. Tauc, Phys. Rev. B 34, 6 (1986)
- [64] Y.X. Yan, E.B. Gamble, K.A. Nelson, J. Chem. Phys. 83, 5391 (1985)
- [65] R. Merlin, Sol. Stat. Comm. 2-3, 207-220 (1997)
- [66] H. J. Zeiger, J. Vidal, T.K. Cheng, E.P. Ippen, G. Dresselhaus, M.S. Dresselhaus, Phys. Rev. B 45, 2 (1992)
- [67] P. Yu, M. Cardona, Fundamentals of Semiconductors, Springer
- [68] M. Eddrief, P. Atkinson, V. Etgens, and B. Jusserand, Nanotechnology 25, 245701 (2014)
- [69] N. Kamaraju, S. Kumar, and A. K. Sood, Eur. Phys. Lett. 92, 47007 (2010)
- [70] K. Norimatsu, J. Hu, A. Goto, K. Igarashi, T. Sasagawa, and K. G. Nakamura, Sol. State Commun. 157, 58 (2013)
- [71] S. Y. F. Zhao, C. Beekman, L. J. Sandilands, J. E. J. Bashucky, D. Kwok, N. Lee, A. D. LaForge, S. W. Cheong, and K. S. Burch, Appl. Phys. Lett. 98, 141911 (2011)

- [72] C. B. Satterthwaite and R. W. Ure Jr., *Phys. Rev.* 108, 1164 (1957)
- [73] B.-L. Huang and M. Kaviani, *Phys. Rev. B* 77, 125209 (2008)
- [74] T. Garl, E. G. Gamaly, D. Boschetto, A. V. Rode, B. Luther-Davies, and A. Rousse, *Phys. Rev. B* 78, 134302 (2008)
- [75] M. Hajlaoui, E. Papalazarou, J. Mauchain, G. Lantz, N. Moisan, D. Boschetto, Z. Jiang, I. Miotkowski, Y. P. Chen, A. Taleb-Ibrahimi, L. Perfetti, M. Marsi, *Nano Lett.* 12, 3532-3536 (2012)
- [76] A. Ayouch, X. Dieudonne, G. Vaudel, H. Piombini, K. Valle, V. Gusev, P. Belleville, and P. Ruello, *ACS Nano* 6, 10614 (2012)
- [77] C. Mechri, P. Ruello, and V. Gusev, *New. J. Phys.* 14, 023048 (2012)
- [78] V. Juve, A. Crut, P. Maioli, M. Pellarin, M. Broyer, N. Del Fatti, and F. Vallée, *Nano Lett.* 5, 1853 (2010)
- [79] Y. Wang, C. Liebig, X. Xu, and R. Venkatasubramanian, *Appl. Phys. Lett.* 97, 083103 (2010)
- [80] D. J. Cebula et al., *Clays Min.* 17, 195 (1987)
- [81] S. L. Johnson, et al. *Phys. Rev. Lett.* 100, 155501 (2008)
- [82] J. M. Ziman, *Principle of Theory of Solids*, Cambridge University Press (1964)
- [83] Y. Wang, B. Qiu, A. J. H. McGaughey, X. Ruan, and X. Xu, *J. Heat Trans.* 135, 091102 (2013)
- [84] J. R. Wiese and L. Muldower, *J. Phys. Chem. Solids* 15, 13 (1960)
- [85] C. Thomsen, H. T. Grahn, H. J. Maris, and J. Tauc, *Phys. Rev. B* 34, 4129 (1986)

- [86] M. H. Francombe, Br. J. Appl. Phys. 9, 415 (1958)
- [87] L. Xue-Dong and Y.-H. Park, Mat. Trans. 43, 681 (2002)
- [88] P. Ruello, S. Zhang, P. Laffez, B. Perrin, and V. Gusev, Phys. Rev. B. 79, 094303 (2009)
- [89] B. Zhou, et al. Phys. Rev. Lett. 101, 246807 (2008)
- [90] C-X. Liu, et al. Phys. Rev. B 81, 041307 (2010).
- [91] . Kim, et al. Nanotech. 27 045705 (2016)
- [92] J. A. Sobota, et al. Phys. Rev. Lett. 108, 117403 (2012)
- [93] D. Hsieh, et al. Phys. Rev. Lett. 107, 077401 (2011)
- [94] E. Golias and J. Sanchez-Barriga, Phys. Rev. B 94, 161113(R) (2016)
- [95] S. Giraud, A. Kundu, R. Egger, Phys. Rev. B 85, 035441 (2012)
- [96] S. Giraud, A. Kundu, R. Egger, Phys. Rev. B 85, 035441 (2012)
- [97] M. Eddrief, P. Atkinson, V. Etgens, B. Jusserand, Nanotech. 25, 245701 (2014)
- [98] K. M. Shahil, M. Z. Hossain, D. Teweldebrhan, A. A. Balandin, Appl. Phys. Lett. 96, 153103 (2010)
- [99] Y. Giret, A. Gellé, B. Arnaud, Phys. Rev. Lett. 106, 155503 (2011)
- [100] F. Vidal et al., Phys. Rev. B 88, 241410 (2013)
- [101] Y. Li, et al., Adv. Mater. 22, 4002–4007 (2010)
- [102] G. Allan, C. Delerue, Phys. Rev. B 70, 245321 (2004)
- [103] B-L. Huang, M. Kaviani, Phys. Rev. B 77, 125209 (2008)

- [104] D.M. Mittleman, *Phys. Rev. B* 49, 14435 (1994)
- [105] A. Stella, et. al., *Phys. Rev. B* 53, 15497–15500 (1996)
- [106] A. Arbouet, et. al., *Phys. Rev. Lett.* 90, 177401–4 (2003)
- [107] Y.D. Glinka, et. al., *Appl. Phys. Lett.* 103, 151903 (2013)
- [108] M. Hajlaoui, et. al., *Nature Comm.* 5, 3003 (2014)
- [109] O. B. Wright *J. Appl. Phys.* 71, 1617 (1992)
- [110] V. Gusev, *Acta Acustica* 82, S37 (1996)
- [111] O. Matsuda, O.B. Wright, *Rev. Sci. Instrum.* 74, 895 (2003)
- [112] S. Mohanty and J. Ghose, *J. Phys. Chem. Solids* 53, 81 (1992)
- [113] W.H Strehlow, E.L. Cook, *J. Phys. Chem. Ref. Data* 2, 163 (1973)
- [114] A.G. Joly, J.R. Williams, S.A. Chambers, G. Xiong, W.P. Hess, D.M. Laman, *J. App. Phys.* 99, 053521 (2006)
- [115] R. Grau-Crespo, A. Y Al-Baitai, I. Saadoune, N. H De leeuw, *J. Phys. Condens. Matter* 22, 255401 (2010)
- [116] S. Chakrabarti, D. Ganguli, S. Chaudhuri, *Physica E* 24, 333-342 (2004)
- [117] J.K. Vassiliou, V. Mehrotra, M.W. Russell, E.P. Giannelis, R.D. McMichael, R.D. Shull, R.F. Ziolo, *J. Appl. Phys.* 73, 5109 (1993)
- [118] N. J. Cherepy, D. B. Liston, J. A. Lovejoy, H. Deng, and J. Z. Zhang, *J. Phys. Chem. B* 102, 770 (1998)
- [119] E.S. Harmon, M.R. Melloch, J.M. Woodall, D.D. Nolte, N. Otsuka, C.L. Chang, *Appl. Phys. Lett.* 63, 2248 (1993)

- [120] L. A. Wray, Y. Xia, S.-Y. Xu, R. Shankar, Y.S. Hor, R.J. Cava, A. Bansil, H. Lin, M.Z. Hasan, *Nature Phys.* 7, 32–37 (2011)
- [121] J. Honolka, et. al., *Phys. Rev. Lett.* 108, 256811 (2012)
- [122] H. Yan, D. Song, K. F. Mak, I. Chatzakis, J. Maultzsch, T.F. Heinz, *Phys. Rev. B* 80(12), 121403 (2009)
- [123] G. Lantz, B. Mansart, D. Grieger, D. Boschetto, N. Nilforoushan, E. Papalazarou, N. Moisan, L. Perfetti, V. L. R. Jacques, D. Le Bolloc'h, C. Laulhé, S. Ravy, J-P Rueff, T. E. Glover, M. P. Hertlein, Z. Hussain, S. Song, M. Chollet, M. Fabrizio, M. Marsi, *Nat Commun.* 8: 13917 (2017)
- [124] R. Ernstorfer, M. Harb, C. T. Hebeisen, G. Sciaini, T. Dartigalongue, R. J. D. Miller, *Science* 323(5917):1033–7 (2009)
- [125] V. Recoules, J. Clerouin, G. Zerah, P. M. Anglade, S. Mazevet, *Phys. Rev. Lett.* 96, 055503 (2006)
- [126] F. Bottin, G. Zerah, *Phys. Rev. B* 75, 174114 (2007)
- [127] S. Mazevet, J. Clérouin, V. Recoules, P. M. Anglade, G. Zerah, *Phys. Rev. Lett.* 95, 085002 (2005)
- [128] D. Boschetto, L. Malard, CH. Lui, K.F. Mak, Z. Li, H. Yan, T.F. Heinz, *Nano letters* 13 (10), 4620-4623 (2013)